MICRO-CHANNEL MILLING USING

ABRASIVE WATERJETS AND

HIGH PRESSURE ABRASIVE SLURRY JETS

by

Naser Haghbin

BSc, Mechanical Engineering, Iran University of Science and Technology, 1995

MASc, Mechanical Engineering, Ryerson University, 2011

A dissertation

presented to Ryerson University

in partial fulfillment of the

requirement for the degree of

Doctor of Philosophy

in the program of

Mechanical Engineering

Toronto, Ontario, Canada, 2016

AUTHOR'S DECLARATION FOR ELECTRONIC SUBMISSION OF DISSERTATION

I hereby declare that I am the sole author of this dissertation. This is a true copy of the dissertation, including any required final revisions, as accepted by my examiners.

I authorize Ryerson University to lend this dissertation to other institutions or individuals for the purpose of scholarly research.

I further authorize Ryerson University to reproduce this dissertation by photocopying or by other means, in total or in part, at the request of other institutions or individuals for the purpose of scholarly research.

I understand that my dissertation may be made electronically available to the public.

MICRO-CHANNEL MILLING USING

ABRASIVE WATERJETS AND

HIGH PRESSURE ABRASIVE SLURRY JETS

Naser Haghbin

Doctor of Philosophy, 2016

Mechanical Engineering

Ryerson University

Abstract

Abrasive water jet technology can be used for micro-milling using recently developed miniaturized nozzles. This thesis develops methodologies to predict the shape of micro-channels milled using high pressure abrasive water jets, and presents a new high pressure abrasive slurry jet micro-machining process. Since abrasive water jet (AWJ) machining is often used with both the nozzle tip and workpiece submerged in water to reduce noise and contain debris, the performance of submerged and unsubmerged abrasive water jet micro-milling of channels in 316L stainless steel and 6061-T6 aluminum at various nozzle angles and standoff distances were compared. It was found that the centerline erosion rate decreased with channel depth due to the spreading of the jet as the effective standoff distance increased, and because of the growing effect of the stagnation zone as the channel became deeper. The erosive jet spread over a larger effective footprint in air than in water, since particles on the jet periphery were slowed much more quickly in water due to increased drag. As a result, the width of a channel machined in air was wider than that in water. It was also found that the erosive efficacy distribution changed suddenly after the initial formation of the channel. Then, a new surface evolution model was developed that predicts the size and shape of relatively deep micro-channels up to aspect ratios of 3 resulting from unsubmerged and

submerged abrasive water jet micro-machining (AWJM) using a novel approach in which two different erosive efficacy expressions were sequentially applied.

Since the channels produced by AWJM were found to be relatively wavy due to fluctuations in abrasive mass flow rate, a novel high pressure (water pump pressure up to 345 MPa) abrasive jet slurry micro-machining (HASJM) system was introduced by feeding a premixed slurry into the mixing chamber of a water jet machine with a micro-nozzle. Moreover, an existing model developed for AWJM abrasive particle velocities was modified and used to predict the particle velocity in HASJM, and then verified using a double disc apparatus (DDA). The HASJM system was then used to study the effect of entrained air in abrasive water jet micro-machining (AWJM) by performing experiments at the same particle velocity and dose for the two systems. The centerline waviness, W_a, of micro-channels made in SS316L and Al60661-T6 using HASJM were typically 3.4 times lower than those made with AWJM using the same dose of particles due to the more constant abrasive flow rate provided by the HASJM provided. The centerline roughness, R_a was approximately the same in both processes at a traverse velocity of V_t=4572 mm/min and a nozzle angle of 90°. For micro-channels of a given depth, the widths of those made with HASJM were 25.6 % narrower than those produced with AWJM, mainly due to the wider jet that resulted from the entrained air in AWJM.

Acknowledgements

I would like to thank:

Dedication

This dissertation is dedicated to my dear wife, Negin, my daughter, Elia, and my son, Daniel.

Table of Contents

viii

List of Tables

List of Figures

Nomenclature

Roman symbols

A_m	The average channel cross-sectional area
A_{pw}	The effective interaction areas between the particles and high pressure water
$A_{pw'}$	The effective interaction areas between the particles and low pressure water
A_O	The cross section area in vena contracta zone (assumed equal to orifice diameter)
$A_{ww'}$	The effective interaction areas between the particles and low pressure water
ASV	Opening percentage of abrasive slurry valve stem
C_D	The drag coefficients
d	Channel centerline depth (µm)
d_{cal}	The centerline depths of the calibration channels (µm)
d_{exp}	Expected centerline depth after n passes (µm)
d_j	Jet diameter
d_M	The mixing tube diameter
d_n	Actual channel centerline depth after n passes (µm)
d_o	The jet diameter in vena contracta (assumed equal to orifice diameter)
d_d	Diameter of spherical elements of uniform dispersion phase
E	Specific erosion rate (mg/g)
$E(\beta)$	Specific erosion rate at the global nozzle angle of β (°)
$E(90°)$	Specific erosion rate at the global nozzle angle of 90 (°)
E_{cal}	Centerline erosion rate for a given calibration channel
E_h	Centerline erosion rate at standoff distance of h
E_h^*	Centerline depths of shallow channels at standoff distance h normalized by the depth of the channel machined at h=2 mm
E_1	Centerline erosion rate at standoff distance of h=1 mm
E_{inst}	Instantaneous normalized centerline erosion rate
E_N	Total volumetric centerline erosion rate on the multi-pass channel
E_0	Initial erosion rate after n=2 passes
$E_{out,s}$	The power of the slurry phase of the jet exiting the nozzle

f	The friction factor
F_D^{wp}	The drag forces between high pressure water and particle phases
$F_D^{ww'}$	The drag forces between high pressure water and low pressure water phases
$F_D^{pw'}$	The drag forces between particle and low pressure water phases
$g(\beta)$	The normalized erosion rate at angle of β
h	Nominal standoff distance (mm)
h_{eff}	Effective standoff distance (i.e. the sum of the nominal standoff distance and the channel centerline depth)
h_{total}	Total effective standoff distance
HV	Initial Vickers hardness of the target (GPa)
K	The velocity exponent
L_M	The mixing tube length
$\dot{m}$	Particle mass flow rate incident to the area dA (g/min)
$\dot{m}(n)$	Instantaneous abrasive mass flow rate incident to dA during the nth pass (g/min)
$\dot{m}_p$	The mass flow rate of the abrasive particle entered the mixing tube (g/min)
$\dot{m}_s$	The mass flow rate slurry entered the mixing tube (g/min)
$\dot{m}_w$	The mass flow rate of the high pressure water entered the mixing tube (g/min)
$\dot{m}_{w'}$	The mass flow rate of the low pressure water entered the mixing tube (g/min)
M_a	Total mass of abrasive incident to the target surface (g)
M_m	Total mass of target material removed (mg)
n	Number of passes
P_w	The pressure of the high pressure water upstream of the orifice (MPa)
P_p	Water pump pressure (MPa)
$Q^*(x^*)$	Non-dimensional erosive efficacy
$Q_{inst}^*(x^*)$	Non-dimensional instantaneous erosive efficacy
R_a	Centerline roughness (µm)
Re_d	Reynolds number of the dispersed phase
S	The distance between the upper disc and the recording disc
t	Machining time after n passes to reach a depth z
t^*	Dimensionless machining time after n passes to reach a depth z

T	The time required to propagate the surface at the channel centerline (i.e. $x=0$), to a centerline depth z equal to h
t_C	The corrected time
T_c	The corrected time constant
t_N	The time to reach the expected depth, d_{exp}, after N passes
u_w	Velocity of the high pressure water phase in the mixing tube (m/s)
$u_{w'}$	Velocity of the low pressure water phase in the mixing tube (m/s)
u_p	Velocity of the abrasive particle phase in the mixing tube (m/s)
$V^*(x^*)$	$V^*(x^*)=V(x^*)/V(0)$ is the dimensionless particle velocity distribution at the surface
V_j	Velocity of the slurry jet at the exit of nozzle tip (m/s)
V_m	Total volume of material removed from the target surface
V_p	The average particle velocity in DDA test (m/s)
V_s	Velocity of slurry entered mixing tube (m/s)
V_t	The nozzle traverse velocity (mm/min)
V_w	Velocity of high pressure water entered mixing tube
W	Channel width (µm)
W_a	Centerline waviness (µm)
$W_{t,in}$	Inlet particle concentration (wt%)
$W_{t,out}$	Output particle concentration (wt%)
x	Width coordinate
x^*	Dimensionless width coordinate
y	Axis along the channel length
z	Depth coordinate
z^*	Dimensionless depth coordinate
$z^*(0,t^*)$	Dimensionless depth at $x^*=0$ and dimensionless time of t^*, or dimensionless centerline depth at dimensionless time of t^*
$z^*_{,t^*}$	The derivative of z^* with respect to t^*
$z^*_{,x^*}$	The derivative of z^* with respect to x^*
$z^*_{,x^*x^*}(x^*,t^*)$	The second derivative z^* with respect to x^*

Greek symbols

α	The particle local impact angle (°)
α_p	The volume fraction of the abrasive particles in the mixing tube
α_w	The volume fraction of the high pressure water in the mixing tube
$\alpha_{w'}$	The volume fraction of the low pressure water in the mixing tube
β	The global angle of the nozzle (°)
ε	Curvature-dependent smoothing term
η	Orifice efficiency
θ	Nozzle angle with the channel centerline (°)
μ_c	The viscosity of the continuous phase
ρ_p	The density of abrasive particles
ρ_w	The density of the high pressure water upstream of the orifice
$\rho_{w'}$	The density of the low pressure water entered to nozzle from slurry tube
ρ_p	The density of abrasive particles
σ	The spread of the erosive efficacy (standard deviation of a normal distribution)
$\phi^*(x^*)$	$\phi^*(x^*) = \phi(x^*)/\phi(0)$ is the dimensionless particle flux
φ	The angle of scar centerline with the reference line
ω	The disc angular velocity (rpm)

Chapter 1 Introduction

1.1. Water jet technology

Abrasive water jet (AWJ) machining and abrasive slurry jet (ASJ) machining are water jet based technologies for micro machining in a variety of materials such as metals, glass, ceramics, polymers, and composite materials.

In AWJ machining, an abrasive water jet (AWJ) machine uses an ultra-high water pressure (134 MPa to 345 MPa) jet of (1) water only, (2) water and air or (3) water, air, and abrasive additives to cut, mill or polish different materials [1]. In an AWJ machine (Figure 1-1), hydraulically driven high-pressure pumps bring the water to the applied cutting pressures. A pressure surge chamber produces a uniform flow of high-pressure water without a pressure
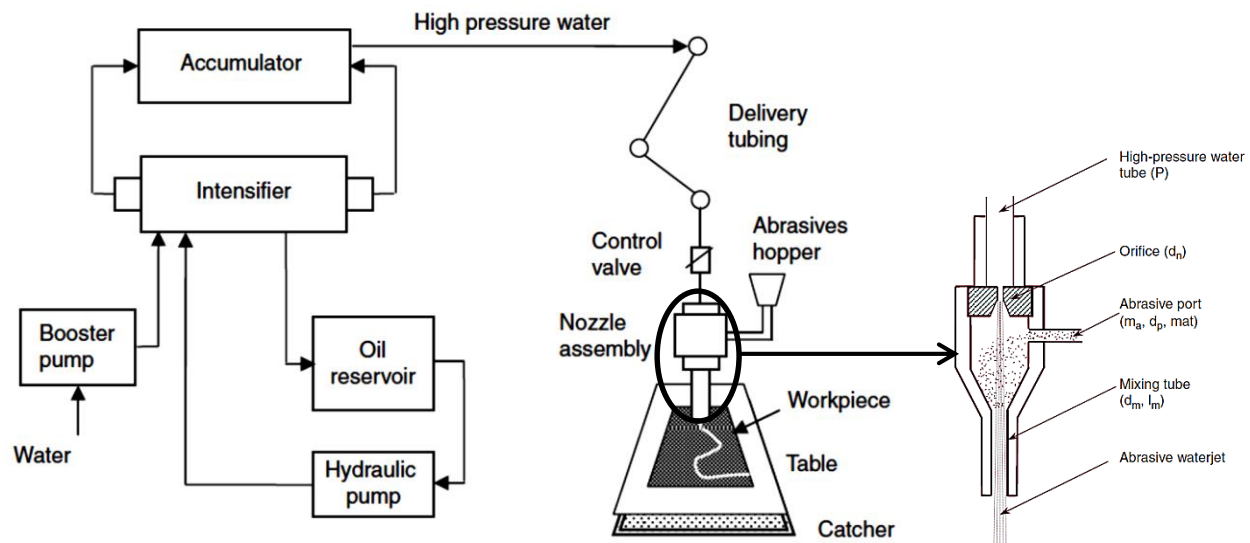
Figure 1-1 Two-dimensional abrasive water jet cutting system [2].

variation. In the next step, the high-pressure water is directed through a small 0.1 mm-0.4 mm sapphire focusing orifice and a high-speed (i.e. 900 m/s) waterjet is formed [2]. As the water jet passes through the mixing tube, abrasive media (usually garnet) is fed in and mixed with the water stream. Then, the momentum of this high-speed water is gradually transferred to the abrasive particles, which enter into the mixing chamber and move down the mixing tube and ultimately

exit. The resulting abrasive particle speeds are generally 250-720 m/s. Because of this operation, a focused jet with a diameter on the order of the nozzle diameter is produced that will erode the workpiece material at impact [3]. In contrast with the AWJ system, no air is entrained into the ASJ system, because the abrasive and water are premixed in a separate container and then this slurry of abrasive and water is pumped through the orifice (i.e. traditional ASJ setup suggested by Miller [4]).

AWJs have been used in the past mostly for large scale material separation, i.e. cutting, with kerf widths on the order of 1.3 mm. Recently, however, there has been considerable attention paid to the possibility of using AWJ machines to perform controlled depth milling (CDM) of these larger scale features. For example, Hashish [5,6] performed preliminary milling experiments on aluminum, titanium, glass and graphite composites with an AWJ machine, concluding that it is one of the most energy efficient methods of material removal, and has a great potential to be used in milling applications. Problems associated with the use of AWJs as a CDM technique include insufficient tolerance on depth, and unsatisfactory surface waviness and surface roughness of the milled area [7]. Ali and Wang [8] explained that AWJ equipment show potential to be used for the milling of materials in different patterns and shapes, using spiraling, zigzagging, stitching, and lapping patterns; however, they did not present any experimental results. Alberdi et al. [9] modelled the kerf shape of a straight channel as a Gaussian bell function using the maximum channel depth (d), maximum width (w), and the width at the half of the maximum depth ($w_{0.5}$) as design variables. Freist et al. [10] used a cosine function to find the kerf geometry of channels made in ceramics. Laurinat et al. [11] also suggested an analytical model to predict the depth of cut in ductile materials using a modified cosine. However, these preliminary studies were mostly empirical and proof-of-concept for the milling of features larger than about 1 mm. More extensive research is required to understand and control operating parameters in the micro-AWJ milling domain.

1.2. Literature review

In this section, a literature review of the developments in experimental and modeling aspects of AWJ machining will be presented to identify the knowledge gaps and potential areas for further research.

1.2.1. Solid particle erosion

The abrasive particles machine a material surface using solid particle erosion mechanism. Material response to particle impact has been classified as ductile erosion and brittle erosion [8] as shown in Figure 1-2. Ductile erosion is applicable to materials (e.g. metals) that can have
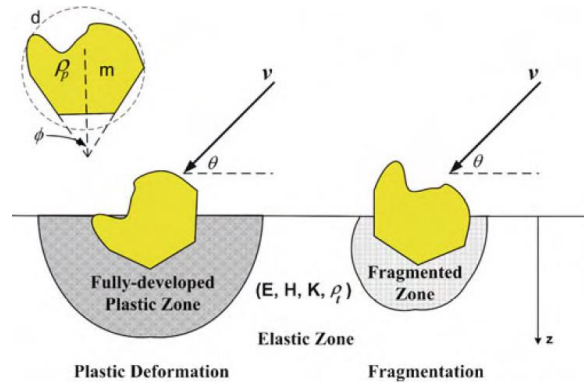
Figure 1-2 Ductile and brittle erosion modes [8].

plastic deformation and be scratched or ploughed under the impact of solid particles [12-14]. Brittle erosion applies to ceramics, glasses, and hard materials that do not have a significant plastic deformation and respond to impact loads by fracture forming cracks and fragmentation of affected zone [8]. Most ductile materials eroded by angular particles exhibit a peak erosion rate at incident angles of 20°-45° [8]. For brittle materials, the peak erosion occurs at angle 90°.

1.2.2. Particle embedding

AWJ machining can result in the embedment of abrasive particles in the target surface, which may cause problems such as coating delamination, imprint transfer problems in a micro-mold, and fatigue life reduction [16,19-21]. There are some papers about embedment of particles with relatively low velocities, e.g. in air-driven abrasive jet micro machining (AJM) [19-26]. Getu et al. [19] defined two criteria for embedment (i.e., particles do not lose contact with the target in the impact process and friction force between the particle and target is larger than the elastic rebound force the target applies on the particle). However, there are relatively few studies on the effect of processing parameters on the embedment of micro-particles into a target surface during milling with AWJ [16]. Ramulu and Raju [27] found that harder abrasive particles have a slight tendency

3

to be embedded. The shape of particles is another important factor that may affect particle embedment [22]. Ives and Ruff [22] explained that embedded particles, which are continually bombarded with incoming particles, are fractured and more deeply embedded. Particle embedment also depends on its impact angle. Higher impact angles (90°) generally lead to a lower level of particle embedment [22]. Shipway et al. [28] found that the level of embedded particle is rapidly reached a steady-state condition and then it does not increase with the number of passes of the jet.

1.2.3. Effect of the plain water jet (PWJ)

The effect of the high-speed water machining with AWJ is not completely understood [29]. Hashish [5] concluded that the water only accelerates the abrasive particles and cannot remove material from many metals. However, Summers et al. [30] observed pitting at steel surface under high water pressure (210 MPa). Ramulu [31] found that both the abrasive particles and high-pressure water act during piercing of brittle materials. Indeed, some authors [32, 33] have used PWJ machining instead of AWJ machining for surface treatment, peening, milling, and cleaning technology due to its specific advantages, such as cost-effectiveness, environmental friendliness, and lack of grit embedment. Kong et al. [33] firstly attempted to use an ultra-high pressure water jet for milling hard materials such as gamma titanium aluminide. They concluded that PWJ has a high potential to generate features such as slots, grooves, and closed loop pockets on difficult to cut materials.

1.2.4. Effect of the entrained air

Along with abrasive, a significant amount of air is entrained into the abrasive jet in AWJ processes. The air-volume flow rate depends on several process parameters, including the pump pressure, abrasive flow rate, mixing-chamber design, focus diameter, and abrasive feed diameter. Himmelreich [34] measured the air-volume flow rate and found it increased almost linearly with the square root of the pump pressure ($\dot{Q}_{air} = a_3.\sqrt{p}$). Tazibt at al. [35,36] confirmed this relationship and found that the air occupies more than 90 percent of the volume of an abrasive water jet. The entrained air-volume flow rate significantly decreased as the abrasive-mass flow rate increases [37].

Madadnia et al. [38] have postulated that the entrained air may play a major role in the jet cutting process. Chillman et al. [39] compared a plain water jet (PWJ) with a water air jet (WAJ)

4

and concluded that the air flow in a WAJ could increase the erosive nature of the jet by accelerating the breakdown of the solid fluid flow into droplet fluid flow (Figure 1-3).
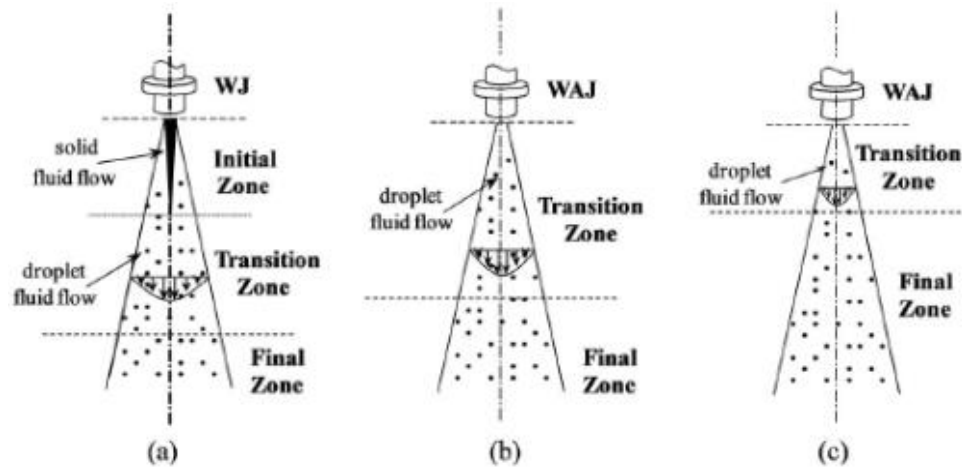
Figure 1-3 Water jet regions with distance from nozzle for three different conditions: (a) waterjet, (b) water-air jet with low air flow rate, and (c) water-air jet with high air flow rate [40].

The impingement of water droplets can cause erosion on the target material [39-41]. Huang et al. [32] explained that an initial stage of surface damage (i.e. material deformation) is formed by the water jet impingement and the subsequent surface damage is made by hydraulic penetration and lateral outflow of the water jet. Some papers [1,35,36] assumed a homogeneous mixture of water, air and particles in an AWJ. However, there is disagreement on this point, as others claimed that AWJ has non-uniform characteristics made up of different zones that vary from the interior to the exterior of the jet [42-44].

1.2.5. Channel repeatability and waviness in AWJ machining

It is important to minimize surface waviness to prevent further finishing operations [28]. Chen and Siores [45] classified the causes of waviness formation into two categories, i.e. internal and external effects. The internal effect occurs because the kinetic energy in the jet is not uniformly distributed. For example, the jet energy has a wavy distribution, which this leads to a wavy striation formation on the target surface. The external effects refer to the fluctuation or unsteadiness of the

AWJ process parameters, including nozzle traverse velocity, water pressure, abrasive mass flow rate, air flow rate, as well as vibration of the workpiece and cutting head during machining [46,47].

Water pressure has a significant influence on waviness of a cutting surface. Waviness is minimized at high water pressure since it provides sufficient energy to the abrasive enabling cutting [47]. Shipway et al. [28] noticed surface waviness increases with a decrease of traverse speed or an increase of multiple depth passes of the nozzle across the workpiece.

An increase in the abrasive flow rate substantially reduces a cutting surface waviness. At lower abrasive-mass flow rate, the primary wavelength is about $6.d_{jet}$. With an increase in the abrasive mass flow rate, the wavelength reduces initially due to decrease of air bubbles and increase of particle flux, and then it increases due to decrease of particles energy [29].

1.2.6. Abrasive slurry jet machining

Abrasive slurry jet (ASJ) machining is another water jet based technology for micro machining on metals, glass, ceramics, polymers and composite materials [4]. In ASJ machining, abrasive and water are premixed in a separate container and the slurry is pumped through a small orifice. In contrast with AWJ, no air is entrained in an ASJ, so that it behaves as a homogeneous jet without a water droplet zone at small standoff distances. The initial studies [91, 81, 48] of ASJ machining have shown that low pressure (<14 MPa) ASJ erosion is a practical process not only for cutting, but also for milling/etching of glasses and other ceramics. Because of the relatively low kinetic energies involved, the etch rate on metals is relatively low. Miller [4] also looked at high pressure slurry (70 MPa). However, the problem of his setup is the wear of the orifice, since the slurry forced through the orifice. In this research (Chapter 4), the AWJ machine will be used in the manner that the slurry will be added in the mixing tube. This is a potential large advantage to avoid any damage to the orifice.

1.2.7. Surface evolution model of milling in AWJ machining

A major step for controlled-depth milling in AWJ machining is to develop a model to predict the channel profile [49]. Some researchers [49,51] used statistical and empirical approaches (e.g. interpolation and regression analysis), which require many experiments varying a large number of parameters and must be repeated for each target material/abrasive powder combination. Artificial

intelligence approaches, such as genetic algorithms and programming [50,52] also require a great deal of raw data for model construction. Simulation approaches, such as the finite element method [17], require long computational times and simplifying hypotheses.

A mathematical model to predict the AWJ milled single-pass surface profile or 'footprint' using a relatively large nozzle (mixing tube diameter of 1 mm, with an average garnet particle size of 180-300 µm), has been developed by Kong et al [49], Axinte et al. [53] and Billingham et al. [54]. These models are broadly similar to the surface evolution models for the abrasive air jet machining (AJM) of glass first introduced by Boonkamp and Jansen [55] and Slikkerveer et al. [56], and later refined by Papini, Spelt and coworkers [57-58], who also extended them for use in the AJM of ductile materials such as polymethylmethacrylate (PMMA) [19,57] and metals [20,21]. The main differences between the surface evolution approach of Papini, Spelt and coworkers for AJM, and those used by Axinte et al. for AWJ are: (i) in contrast to the AJM models, the AWJ models did not consider the dependency of erosion rate on impact angle that occurs for ductile materials [59,60], (ii) the AWJ models have been tested for only relatively shallow features on titanium Ti6Al4V up to aspect ratio of 0.4, while the AJM models have been tested with high accuracy to aspect ratios up to 1.2 where the surface evolution can generate sharp corners or when the converging sidewalls at bottom of the feature bottom create a pointed profile.

1.2.8. Submerged and unsubmerged AWJ machining

Most previous studies of AWJ machining were limited to machining in the air; however, AWJ machining is often performed with a submerged nozzle tip and workpiece in order to reduce jet noise and abrasive dust. Since the drag of the surrounding fluid is significantly different when machining in air or water, it would be of interest to determine what effect this would have on the topography of the machined features, and the applicability of the surface evolution model.

1.2.9. AWJ velocity

1.2.9.1. Water velocity

In an AWJ process, a pressurized water is passed through an orifice and a high-speed water jet is generated. Using Bernoulli's Law and the nozzle coefficient (η), the velocity of the exit water-jet can be estimated as [29]

$$V_w = \eta. \sqrt{\frac{2.P}{\rho_w}} \qquad (1.1)$$

where P and ρ_w are water pressure and density, respectively. The coefficient (η) expresses the nozzle efficiency, by characterizing momentum losses due to wall friction, fluid-flow disturbances, and the compressibility of the water [29]. It can be measured by measuring impact force of the water jet and the nozzle diameter as follows [29]:

$$\eta = \sqrt{\frac{2.F_w}{\pi.\rho_w.d_N^2}} \qquad (1.2)$$

where F_w is the water-jet impact force and d_N is the nozzle diameter. Momber and Kovacevic [29] found that the nozzle efficiency coefficient is usually between $0.83 < \eta < 0.93$.

1.2.9.2. Particle velocity

Erosion of metals is highly influenced by the particle impact velocity. It has generally been accepted that the erosion rate, E, is a function of the particle velocity, V. This relation is often empirically modelled as [59-61]

$$E = C(V)^K \qquad (1.3)$$

where C is a constant and K is the velocity exponent. The predicted channel profile shape is thus a strong function of K. In AJM, Oka et al. [59] and Yerramareddy and Bahadur [62] observed that the value of K is between 2 and 3 for ductile metals, and between 3 and 5 for brittle metals in air abrasion processes. However, very few studies have investigated the value of K for AWJ, probably because of the difficulty in determining the particle velocity.

1.2.9.3. Experimental measurement of particle velocity

Several methods have been introduced to measure the abrasive velocity [63-72], such as laser dopper velocimetry [63], inductive method [64], the jet impact force method [66], rotary disk method [72], PIV (particle image velocimetry) method [68,71]. Liu et al. [72] used a dual-rotary disk apparatus to measure the average maximum water-droplet and abrasive speeds. This apparatus consists of two discs, fixed to a shaft one above the other at a given separation, and made to rotate rapidly. The particles pass from a narrow slot on the upper disk and generate an erosion scar on

the lower disk. The average speed of the particles (V_a) is found by measuring the angle, between a reference line directly below the slot, and a line through the center of the erosion scar.

Sawamura et al. [68] used the PIV (particle image velocimetry) method for measuring particle velocity. However, in doing so, they faced problems due to the presence of air bubbles in the abrasive water jet. The air bubbles were difficult to distinguish from the abrasive particles. Their results were thus limited by high uncertainties.

Coray et al [69] compared all possible particle velocimetry methods and concluded that the method of laser-induced fluorescence and particle tracking velocimetry (LIF/ PTV) may be a promising method for the future. In the LIF/ PTV method, the abrasive particles are coated with a thin layer of fluorescent dye which is excited by a pulsed laser, and the emitted radiation is detected by a CCD camera [70]. Roth et al. [71] tried conditions, but LIF/ PTV method under real AWJ conditions but they had problems with the dye detaching from the abrasive particles, thus creating extensive background noise. The detachment problems are probably due to the use of Rhodamine B dye, a water-soluble material which is thus likely unsuitable for abrasive water jet applications. A sophisticated nonlinear image processing algorithm was developed to eliminate this noise and identify the fluorescent particles in the abrasive water jet. This algorithm helped to visually detect about 90% of the particles while only few ghost particles created.

Generally, previous research suffered from one or more of the following problems: 1) only the average particle velocity was determined; 2) the results were not reliable due to difficulties in image processing to distinguish abrasive particles in a mixture of abrasive+water+air; 3) unrealistic conditions have been used, e.g., using magnetic particles instead of abrasive garnet so that a conductive-correlative method can be used; 4) previous investigations were not performed for micro-abrasive water jets.

1.2.9.4. Theoretical prediction of particle velocity

Theoretical models of particle velocity in AWJ applications have also been developed. For example, Tazbit et al. [35,36] used the momentum equation to find particle velocity in a two phase (abrasive-water) system. They assumed that the particles move under the action of drag determined the velocity as a function of the distance along the mixing tube. They claimed that their model can

predict the particle velocity at impact where there is also entrained air by replacing the water density in their equations with the following fluid jet density [1]: $\rho_{fl} = \beta\rho_{air} + (1 - \beta\rho_{water})$. In this relationship, β is the air volume fraction in the total volume of air-particles, which was experimentally measured in their article. Zhang [73] also experimentally explored the air flow rate in the abrasive feed tube.

Liu et al [79] suggested an idealized "reverse-bell" shape particle velocity and abrasive distribution when modeling AWJ, without considering air effects. Li et al. [80] derived perhaps the most complete model of particle velocity distribution in a micro abrasive air jet (i.e., AJM) in the nozzle and after leaving the nozzle in free jet flow. Narayanan et al. [81] used the Bernoulli's, momentum and continuity principles to find particle velocity in an abrasive water jet, which was a three-phase flow consists of water (i.e. a non-compressible fluid), air (i.e. a compressible fluid), and abrasive.

1.2.10. Abrasive water jet micro-machining (AWJM)

All mentioned investigations have concentrated on the macro milling/cutting range. Further downsizing of the AWJ raises some challenges and difficulties in achieving consistent and uniform feeding of abrasives to the micro AWJ nozzle [82,83] due to: 1) a more complex flow phenomena in a three-phase micro abrasive water jet; 2) lower flowability of smaller particles due to the tendency of fine abrasives to coagulate or clump together as explained by Liu [83].

Lately, some researchers have attempted to use abrasive water jets (AWJ) for micro-cutting applications [82-85], because conventional micro-machining methods such as chemical etching [86 5], micro-milling machining [87,88], electrical discharge machining (EDM) [89], and laser machining [90] require relatively expensive equipment, employ hazardous chemicals, are time-consuming, cause thermal damage to the material, and can result in poor surface texture [91]. AWJs produce features with no heat-effected zone, minimal residual stresses, and edges without crushing, and having fewer defects [82,83]. For example, over the past five years, miniature AWJ nozzles, miniature AWJ nozzles and ancillary devices have been developed for micro-machining very small through-cut features [85], such as stainless steel micro-channels for fuel cells [92], stainless steel plates for orthopedic implants to repair bone and skull fractures [93], various medical devices [93], and miniature mechanical components, such as planetary gears [84].

1.2.11. Summary

The initial studies of AWJ machining [87-91] have shown that it is promising not only for cutting, but also milling/etching of materials. However, little is known about the relationship between AWJ operating parameters and the resulting erosion rates, especially in the range of micro-machining. Moreover, micro-milling of channels using water jet technology is also a potential research area. In addition, there is no reliable surface evolution model for prediction of channel profile. The machined channel cross-sectional profiles are highly dependent on the velocity distributions in the AWJ, which should be measured using suitable techniques. The influence of water and air on the resulting machined channel shape and quality also requires more investigation. Finally, the problem of repeatability and waviness resulting AWJ milling is an important issue that needs to be investigated and solved in future research. The research objectives of this thesis, outlined in Section 1.3, aim to address these challenges.

1.3. Objectives

This research investigates milling of micro-channels using abrasive water jet micro-machining (AWJM) and high-pressure abrasive slurry jet micro-machining (HASJM). In order to overcome the shortcomings of previous models and to improve channel quality (i.e. reduce waviness and roughness), this dissertation develops methodologies to predict the shape of micro-channels milled using high pressure abrasive water jets, and presents a new high pressure abrasive slurry jet micro-machining process. The following secondary objectives were identified to build towards the main objectives:

(i) Determine the effect of unsubmerged and submerged machining on the size and shape of micro-channels (Chapter 2).

(ii) Develop a surface evolution model to predict the size and shape of relatively deep micro-channels, resulting from unsubmerged and submerged abrasive water jet micro-machining (AWJM) (Chapter 3).

(iii) Introduce a new high-pressure abrasive slurry-jet micro-machining (HASJM) apparatus from a relatively simple modification to a commercial high-pressure water jet (Chapter 4).

(iv) Isolate the effect of the entrained air in abrasive water jet micro-machining (AWJM) by comparing the centerline roughness and waviness of micro-channels made using AWJM and HASJM under identical velocity and dose conditions (Chapter 5).

Chapter 2 Abrasive Waterjet Micro-Machining of Channels in Metals: Comparison Between Machining in Air and Submerged in Water

This chapter is based on the following published paper:

N. Haghbin, J. K. Spelt, and M. Papini, "Abrasive waterjet micro-machining of channels in metals: comparison between machining in air and submerged in water," *International Journal of Machine Tools and Manufacture*, vol. 88, pp. 108-117, 2015.

2.1. Introduction

There has been increased recent interest in the use of abrasive waterjets (AWJ) for micro-machining. For example, miniature AWJ nozzles have been used to micro-machine through-cut features as small as 200 µm [85], stainless steel micro-channels for fuel cells [92] stainless steel plates for orthopedic implants to repair bone and skull fractures [92], and miniature mechanical components, such as planetary gears [85]. Liu et al. [83] used AWJ to machine micro-features in composites and thin metals, and Liu and Shubert [84] outlined some of the difficulties involved in preventing clogging by fine abrasives as they flow from the mixing tube to the micro-nozzle. A key motivation for this interest in AWJ micro-machining is the ability to machine a wide range of materials with no heat-affected zone, minimal residual stress and relatively little edge damage. There has also been considerable attention paid to the use of AWJ machines to perform controlled depth milling of larger scale features having widths greater than 1.3 mm. For example, Hashish [5,6] performed preliminary milling experiments on aluminum, titanium, glass and graphite composites with an AWJ machine, concluding that it is one of the most energy efficient methods for material removal, and has a great potential in milling applications. Axinte et al. [53] machined multi-pass channels in glass and developed models to predict their developing cross-sectional shapes. Kong et al. [49] machined straight, single-pass channels in titanium, while Billingham et al. [54] milled overlapped, single-pass channels in titanium. Shipway et al. [28] investigated the role of waterjet pressure, jet impingement angle, traverse speed, and abrasive size on waviness and roughness of milled channels in titanium.

A vast published literature shows the effect of standoff distances on width, depth and AWJ velocity for cutting applications; however, very few of them discuss these effects in milling applications. Regarding milling, Laurinat et al. [11] showed that the top kerf width of channels is proportional to the standoff distance. Alberdi et al. [9] found that the standoff distance is the most important factor for the kerf width. Srinvasu et al. [77] reported an increased width at a shallower jet impingement angle, i.e. nozzle angle less than 90°, which is due to the increase in width of jet footprint. Moreover, they found that the kerf width deceased with the increase in jet feed rate, although the difference was insignificant. For cutting, Kovacevic [94] showed that an increase in the standoff distance decreased the depth of cut almost linearly. Chen et al. [95] explained that this is because the jet power reaching the workpiece decreases when standoff increases, and therefore the lower part of the kerf cannot be machined as efficiently. Momber and Kovacevic [29] noted that, compared to other cutting parameters, changes in the standoff distance do not significantly influence the velocity of the abrasive particles. Clark and Burmeister [96] also discussed the stagnation effect as the formation of a film on the impacted zone that decreases the particle velocity and the ability to erode. Matsumura et al. [97] explained that this stagnation effect is controlled by the channel sidewall angles, which changes the slurry flow direction and reduces the AWJ velocity. Lv et al. [98] used a CFD model to simulate slurry velocity in the impact zone.

All of previous studies of AWJ cutting and milling have been conducted with the nozzle and target in air rather than submerged. However, AWJ machining is frequently performed with a submerged nozzle and workpiece in order to reduce noise, splash and airborne debris. For example, Radvanska et al. [99] suggested using submerged AWJ machining as a safer machining method, with some of the kinetic energy of the jet being consumed in order to reduce noise. Shimizu [100] found that a submerged stationary slurry jet with a pressure of 20 MPa at standoff distances between 20 and 40 mm caused cavitation erosion on the workpiece after 2 h of machining. Madadnia et al. [38] found a similar cavitation effect on an aluminum sample at standoff distance 50 mm after 180 s of machining with a stationary submerged water jet having a diameter of 254 μm at a pressure of 240 MPa submerged in a slurry solution. However, submerged milling using an abrasive water jet and the effect of the surrounding water on the erosion rate, depth, and width of channels at relatively lower standoff distances (less than 5 mm) appears not to have been considered in the literature. Since the drag on the particles due to the surrounding fluid is

significantly different when machining in air and water, the effect on the topography of the resulting micro-machined features needs to be considered.

Previous research studies did not consider abrasive water jets for micro-milling purposes. This chapter presents a comparison of submerged and unsubmerged abrasive water jet micro-milling (AWJM) of micro-channels in 6061 aluminum alloy and 316L stainless steel using a novel prototype miniature nozzle with a 254 µm mixing tube. Experiments were conducted to examine the relative effects of nozzle standoff, channel depth and jet impingement angle on the erosion rate and shapes of channel cross-sections.

2.2. Experiments

2.2.1. Experimental setup

An OMAX 2626 Jet Machining Center (OMAX Corp., Kent, WA, USA) was used with a prototype nozzle having orifice and mixing tube diameters of 127 µm and 254 µm, respectively. Channels were micro-milled at pressures between 131 MPa and 268 MPa with the nozzle and target submerged in water (Figure 2-1) and in air. A treated 320-mesh garnet, with an average size of 38 µm (Figure 2-2) was used in all experiments. Table 2.1 gives the range of AWJ parameters used in the experiments. The aluminum alloy 6061-T6 and stainless steel 316L target samples were 3 mm thick and were cut into 16×5 cm pieces. These were clamped to a stationary base that was placed underneath the nozzle at standoff distances between 2 and 4 mm (Figure 2-1).

The nozzle movement was computer controlled with a positioning accuracy of ±76 µm over 30 cm and a maximum scan speed of 4572 mm/min. The resulting micro-channel profile shapes were measured using a non-contact optical profilometer (model ST 400, Nanovea, Irvine, CA, USA) having a lateral and vertical resolution of 0.1 µm. A scanning electron microscope was used for further characterizing the channels.
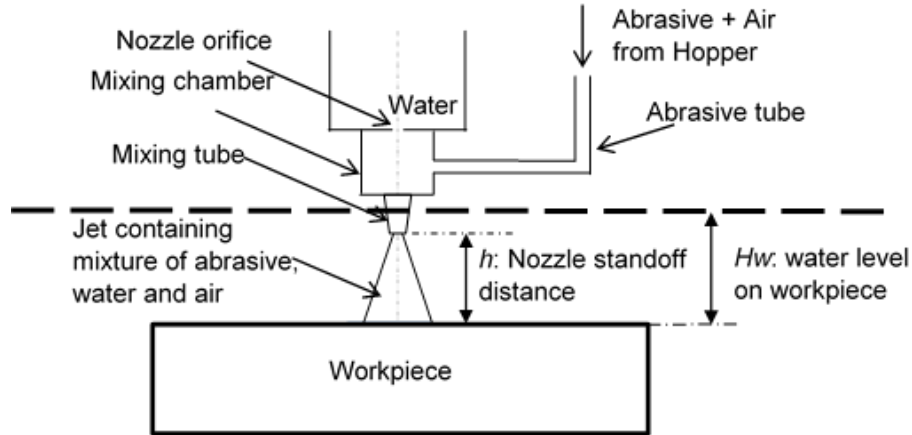
Figure 2-1 Schematic of submerged abrasive water jet. Not to scale.
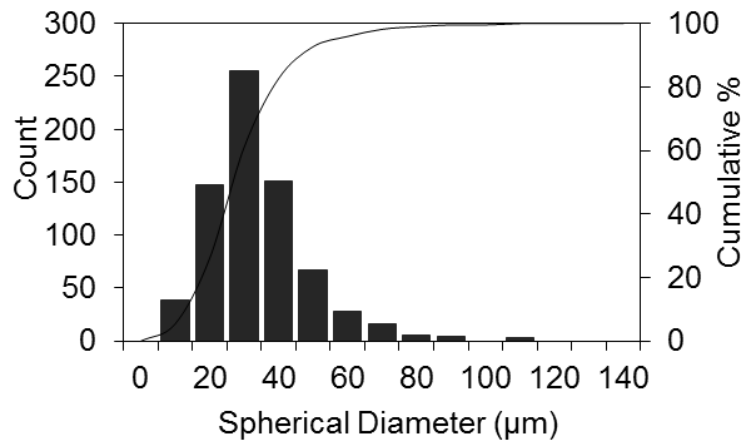
Figure 2-2 Particle size distribution of garnet abrasive. Curve gives cumulative percent.

Table 2.1. Machining parameters.

Standoff distance (mm), h	2, 2.5, 3, 3.5, 4
Submerged depth (mm), H_W	20
Abrasive mass flow rate (g/s), $\dot{m}_a$	0.6-1.1
Garnet nominal diameter (μm)	38, 75
Water pump pressure (MPa), P_p	138
Traverse speed (mm/min), V_t	1000, 4572
Nozzle angle (deg.), $\varTheta$	90°, 60°, 45°, 30°, 15°
Number of passes, n	1, 2, 4, 10, 20, 30, 40, 50
Orifice diameter/mixing tube diameters (μm), d_O/d_M	127/254
Workpiece materials	SS 316L, Al 6061-T6, Glass

2.2.2. Jet size

The jet diameter was used to characterize its spreading behaviour at different standoff distances. It is difficult to define a jet diameter for a water jet since the entrained air bubbles [29] create a diffuse, unsteady transition zone between the jet core and the surrounding media, water or air, as shown in Figure 2-3. In the past, the jet edge has been defined as the location where the impact of individual water droplets was measured [43,44], or the location where the impact force of the jet drops to 5% of its maximum impact force [101].

Core zone of
micro AWJ

Droplet zone
of micro AWJ
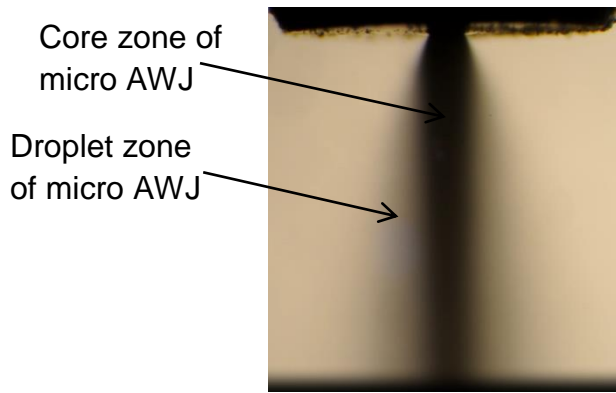
Figure 2-3 Magnified shape of the abrasive water jet emerging from the micro-nozzle blasted in air at P_p=138 MPa with 320 mesh garnet. The narrowest jet diameter is 254 µm where it emerges from the mixing tube.

In the present work, the effective jet diameter at a given standoff distance was defined as the entrance width of the slot cut by the jet in a rigid, 3 mm thick polyurethane modeling foam (Renshape, Huntsman Advanced Materials). Because of its very rapid erosion rate, the jet cut through the foam almost instantaneously, and the resulting cut was created without significant backflow or secondary milling effects. In this sense, the jet diameter was defined as the diameter of the blast zone having sufficient kinetic energy to erode the foam. Tests were conducted at a nozzle scan speed V_t=4572 mm/min, P_p=138 MPa and at standoff distances between 2 and 4 mm with the nozzle either submerged or in air under three conditions: 1. water+abrasive+entrained air (i.e. the normal AWJ operation condition, 2. water+entrained air (i.e. with no abrasive flowing into

16

the mixing tube), and 3. water only (i.e. with the abrasive feed tube blocked so that neither air nor abrasive could enter the mixing tube). The jet diameter was taken to be the average of the slot widths found in 24 width measurements; i.e 8 measurements of width within a 2 cm long machined channel, repeated on three separate channels.

2.2.3. Micro-machining experiments

Straight, stepped channels of various depths were machined into the two target materials using 1, 2, 4, 10, 20, 30, 40 and 50 passes at P_p=138 MPa and V_t=1000 mm/min without turning off the water jet. The measured water flow rate at this pressure was 0.213 L/min. The scanning direction and the nozzle axis were in the same plane, and channels were machined at Θ=30° and 90° at both h=2 and 3 mm (Figure 2-4). Each of the eight sections of the stepped channel corresponding to a particular number of passes was 20 mm long, so the entire channel was 160 mm long; i.e. the first pass of the jet was 160 mm long beginning at y=0 with the second pass returning to y=20 mm, the third pass went to y=140 mm leaving a 2-pass segment at the end, the forth pass returned to y=20 mm, etc.
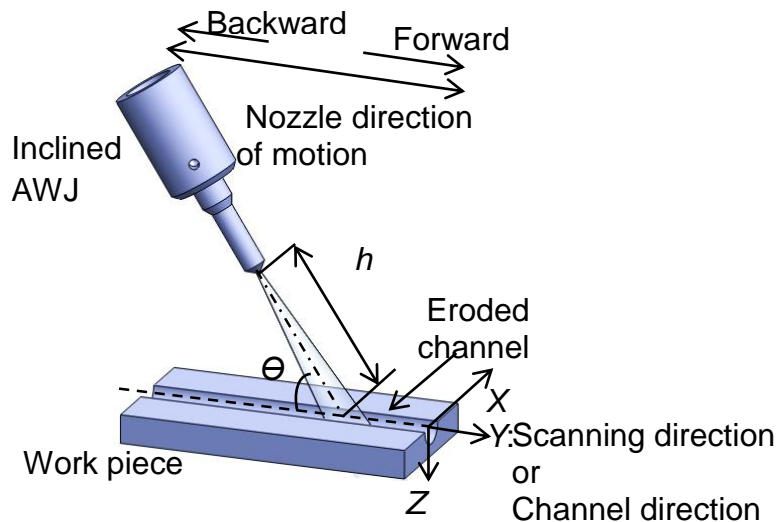
Figure 2-4 Micro-milling with nozzle global angles of Θ=30°, 90°, and standoff distance, h. Not to scale.

Channel depths were reported as the average and standard deviation of 24 total measurements; i.e. 8 measurements within a 2 cm long machined channel, repeated on three separately machined channels. The average width of each of these three 2 cm channels was then calculated using the average cross-section, taken as the one of these 8 profiles which had a centerline depth equal to the average value. The width of a channel was defined by the points on either side where the depth of erosion was 1/8 of the particle diameter (i.e. 4.7 µm for a particle size 38 µm). The erosion depth was defined as the average depth of 10 profilometer points 2 mm apart. Channel to channel scatter in both depth and width was similar to scatter within a channel. The overall standard deviation among the centerline depths and widths were 28 µm and 14 µm, respectively.

Significant variations in the abrasive mass flow rate are typical in AWJ operations [76,77,102]. Therefore, in order to more accurately associate a given multi-pass channel profile with a particular abrasive flow rate, two-pass shallow, 20 mm long, calibration channels were machined beside the main channel at P_p=138 MPa and V_t=1000 mm/min immediately after the machining of the steps having 4, 10, 20, 30, 40 and 50 passes. The depths of these shallow calibration channels were then used to characterize the abrasive flow rate at any number of passes. The positioning accuracy of the water jet was excellent, and the process of repeatedly moving away from the main channel to machine the adjacent calibration channels introduced only a negligible change in the width of the main channel (i.e. 1-3%). The machining of an entire set of channels (i.e. with depths achieved using from 1 to 50 passes) with the associated calibration channels, plus 20 s for jet stabilization, took 20 min, during which time the machine was running continuously.

2.2.4. Measurement of erosion rate

2.2.4.1. Spreading effect on erosion rate

It was found that the erosion rate was affected both by the spreading of the divergent jet as a function of the standoff distance, and the channel depth which affected the constraint of the flow and the size of the stagnation zone. The spreading effect was investigated by measuring the width of channels made in the two target materials. The stagnation effect was quantified by measuring the centerline depth of the channels to define an instantaneous centerline erosion rate (Section 2.2.4.2).

A number of authors have found that the centerline erosion rate due to AWJ machining decreases with increasing standoff. Momber and Kovacevic [29] found a linear decrease in channel depth with an increase in standoff in air due to the radial expansion of the jet spreads and the resulting decrease in the number of impacts per unit area. They found that particle velocity was not influenced significantly by the increase of standoff distance. On the other hand, an excessively small standoff distance may impede flow from the abrasive tube, and so Gao [103] suggested an optimum standoff distance of about 2.0 mm.

To investigate the effect of standoff with the present micro-nozzle, shallow channels were machined at standoffs between 2 and 5 mm on SS316L and Al6061-T6 using P_p=138 MPa, V_t=4572 mm/min, and Θ=90°. To avoid effects associated with the variation of the abrasive mass flow rate, the channels were machined one after the other rapidly without interrupting the AWJ flow.

2.2.4.2. Normalized instantaneous centerline erosion rate, E_{inst}, for micromachining experiments

It was found that the centerline erosion rate decreased with increasing channel depth. In order to study the instantaneous change in the centerline erosion rate with respect to channel depth for the experiments of Section 2.3.3, it was necessary to take into account variations in mass flow rate that occurred during a given multi-pass experiment. These fluctuations were reflected in the change in calibration channel depths. Thus, an expected centerline depth, d_{exp}, after N passes, was defined as

$$d_{exp} = \int_0^N d_{cal}(n)dn \qquad (2.1)$$

where the function $d_{cal}(n)$ is a curve fit of the centerline depths of the calibration channels measured during the course of a machining experiment to create a stepped channel. It is noted that if the abrasive flow rate did not fluctuate during an experiment, Eq. (2.1) was simplified to $d_{exp} = Nd_{cal}$. Figure 2-5 illustrates how the depths of these calibration channels varied over the course of one particular experiment; i.e. the calibration channel depth, d_{cal}, after the machining of each of

the stepped channel segments having 2, 4, 10, 20, 30 40 and 50 passes. Although these variations in d_{cal} were due to changing abrasive mass flow rates that could not be predicted from one experiment to the next, there was a consistent trend of a monotonic decrease with increasing machining time, tending toward a steady value after some period.

The expected centerline depth, d_{exp}, in Eq. (2.1) is an estimate of the channel depth that would have been achieved if there were no decrease of erosion rate due to increasing channel depth; i.e. if the machining had continued on an effectively flat target taking into account the measured fluctuations in the mass flux of the abrasive. As will be discussed in Section 2.3.1, d_{exp} also accounts for the effect of jet spreading due to changes in standoff distance, since d_{exp} was measured for each experimental condition. The only remaining factor affecting channel depth that is not accounted for in d_{exp} is the change in the erosive flow field that is a function of the channel depth. This is the focus of Section 2.3.3.
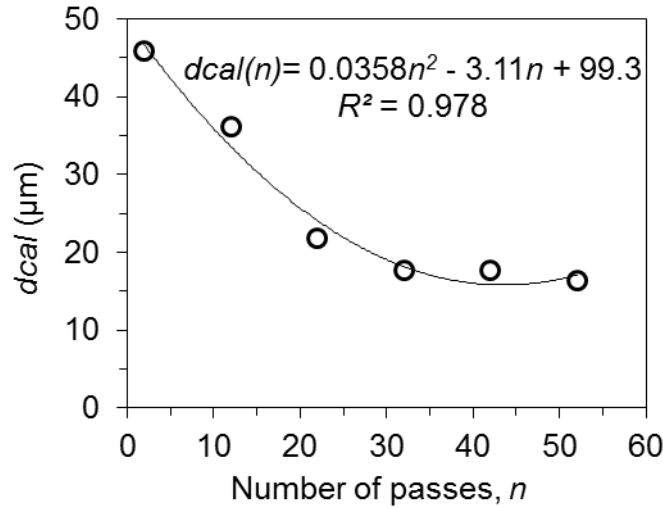
Figure 2-5 Example of centerline depths of two-pass calibration channels, d_{cal}, machined after making each of the stepped channel segments having 4, 10, 20, 30, 40 and 50 passes. SS316L at nozzle angle $\Theta=90°$, $P_p=138$ MPa, $V_t=1000$ mm/min, $h=2$ mm, submerged. Second-order curve fit giving the function of $d_{cal}(n)$ of Eq. (2.1). Each of the data points represents the average depth of a total of 24 measurements on three separate channels. Scatter bars representing ±1 standard deviation were small enough to fit within the symbols.

The depth of a given channel can be related to the centerline erosion rate, E, as follows. Referring to the coordinate system in Figure 2-4, the volume removed due to the impact of particles on a differential area $dA=dydx$ at the centerline is $dV=zdydx$, where z is the centerline depth. If the specimen moves at a traverse speed of V_t, then the removed volume in a time dt becomes

$$dV = zV_t dt\, dx \qquad (2.2)$$

The volumetric erosion rate (volume removed per mass of particle incident) is thus

$$E = \frac{zV_t dt\, dx}{\dot{m}dt} \qquad (2.3)$$

where $\dot{m}$ is the particle mass flow rate incident to the area dA. Thus, the particle mass flow rate delivered to dA on the centerline of a given single pass calibration channel of depth of d_{cal} is

$$\dot{m} = \frac{d_{cal}V_t\, dx}{E_{cal}} \qquad (2.4)$$

where E_{cal} is the volumetric erosion rate for a given calibration channel; i.e. a constant since all calibration channels were shallow, and machined on an initially flat surface at the same standoff distance.

Since each calibration channel was machined immediately after each stepped channel segment having $n=2$, 4, 10, 20, 30, 40, and 50 passes, Eq. (2.4) with the appropriate value of d_{cal} (n) represents the instantaneous mass flow rate delivered to the stepped channels during the nth pass. Thus, for the multi-pass channel segments, the total mass of abrasive delivered to dA on the centerline after N passes is

$$m_{tot} = \left[\int_0^N \dot{m}(n)dn \right] dt \qquad (2.5)$$

21

where $\dot{m}(n)$ is the instantaneous abrasive mass flow rate incident to dA during the nth pass of a machining experiment to create a stepped channel (Eq. (2.4)). The total volumetric centerline erosion rate on the multi-pass channel segments having depth d_n after N passes is thus

$$E_N = \frac{d_n V_t \ dx}{\int_0^N \dot{m}(n)dn} \tag{2.6}$$

Substituting Eq. (2.4) for calibration channels after n passes into Eq. (2.6) leads to

$$E_{inst} = \frac{E_N}{E_{cal}} = \frac{d_n}{\int_0^N d_{cal}(n)dn} = \frac{d_n}{d_{exp}} \tag{2.7}$$

Equation (2.7) shows that the instantaneous normalized centerline erosion rate (ratio of erosion rate at n passes to the erosion rate for a flat surface) is the instantaneous slope of a plot of the actual centerline depth after n passes versus the expected depth at that time; i.e. the depth were the surface to remain flat and at a constant standoff distance up to n passes. This expression will be used in the analyses of Section 2.3.3.

2.3. Results and discussion
2.3.1. Jet size

As mentioned previously, several investigators have noted a decreased erosion rate with channel depth that was attributed to jet spreading as the effective nozzle to surface standoff increases (i.e. distance from the end of the mixing tube to the bottom of the channel). Figure 2-6 shows the jet diameters, d_j, that were taken to be equal to the opening widths of the cuts on the foam material (Section 2.2.2) as measured using an optical microscope. It is evident that the jet diameter increased linearly with standoff distance, although differences existed depending on the composition of the jet, and whether the machining was done in air or submerged under water. For the water-only jet (Figure 2-6a), the jet diameter remained at the orifice diameter (127 µm) up to a standoff distance of 2 mm, and then gradually increased to just less than the mixing tube

diameter, 254 µm, at h=4 mm. For the water with entrained air (Figure 2-6b), the jet was wider, occupying the entire mixing tube (254 µm diameter) at h=2 mm, and gradually spreading to 300 µm at h=4 mm. The diameters of both the water-only jet and the water+air jet (Figure 2-6a, b) were found to be significantly smaller (t-test, $p<0.001$) when exiting in water than in air, presumably because the increased drag of the surrounding water decreased the water droplet velocity at the jet periphery to the point where erosion of the foam target did not occur, thereby creating a narrower channel.

Upstream of the mixing tube, the water jet entrains air with the abrasive particles. The effect of this entrained air on the water jet as it spreads in air was explored by Yanaida and Ohashi [43,44] and Huang et al. [32] who found that after a certain standoff distance the central water jet breaks up into droplets. Chillman et al. [39] concluded that entrained air in a water jet accelerates the breakup of the jet, regardless of whether the jet is in air or is submerged under water. Neusen et al. [104] found that the length of the water jet before it breaks up was sensitive to the jet velocity, and was between $50.d_M$ and $125.d_M$, where d_M is the mixing tube diameter. For the present experiments with the micro-nozzle (d_M =254 µm) at P_p=138 MPa, this implies that the water jet did not break up in the axial direction for the entire range of the selected standoffs between 2 and 5 mm.

For the case of a jet comprised of water+abrasive+air, the channels were much wider than those machined with water+air, reflecting a greater effective jet diameter; i.e. approximately 460 µm or about twice the mixing tube diameter at h=2 mm for both exit conditions. This was probably due to collisions of the abrasive particles with the mixing tube wall, which caused the particles to exit at a greater angle to the nozzle axis. This is similar to the spreading mechanism seen in abrasive air jet machining [14]. Moreover, the addition of abrasive caused the rate of spreading with distance from the nozzle to be greater when the jet exited in air than when it was under water (Figure 2-6c). Therefore, comparing the spreading rates (slopes) of the jets without (Figure 2-6a and b) and with abrasive (Figure 2-6c) revealed that not only was the effective AWJ diameter significantly larger in air than under water, but also that the jet spread more rapidly with abrasive present (t-test, $p<0.001$).
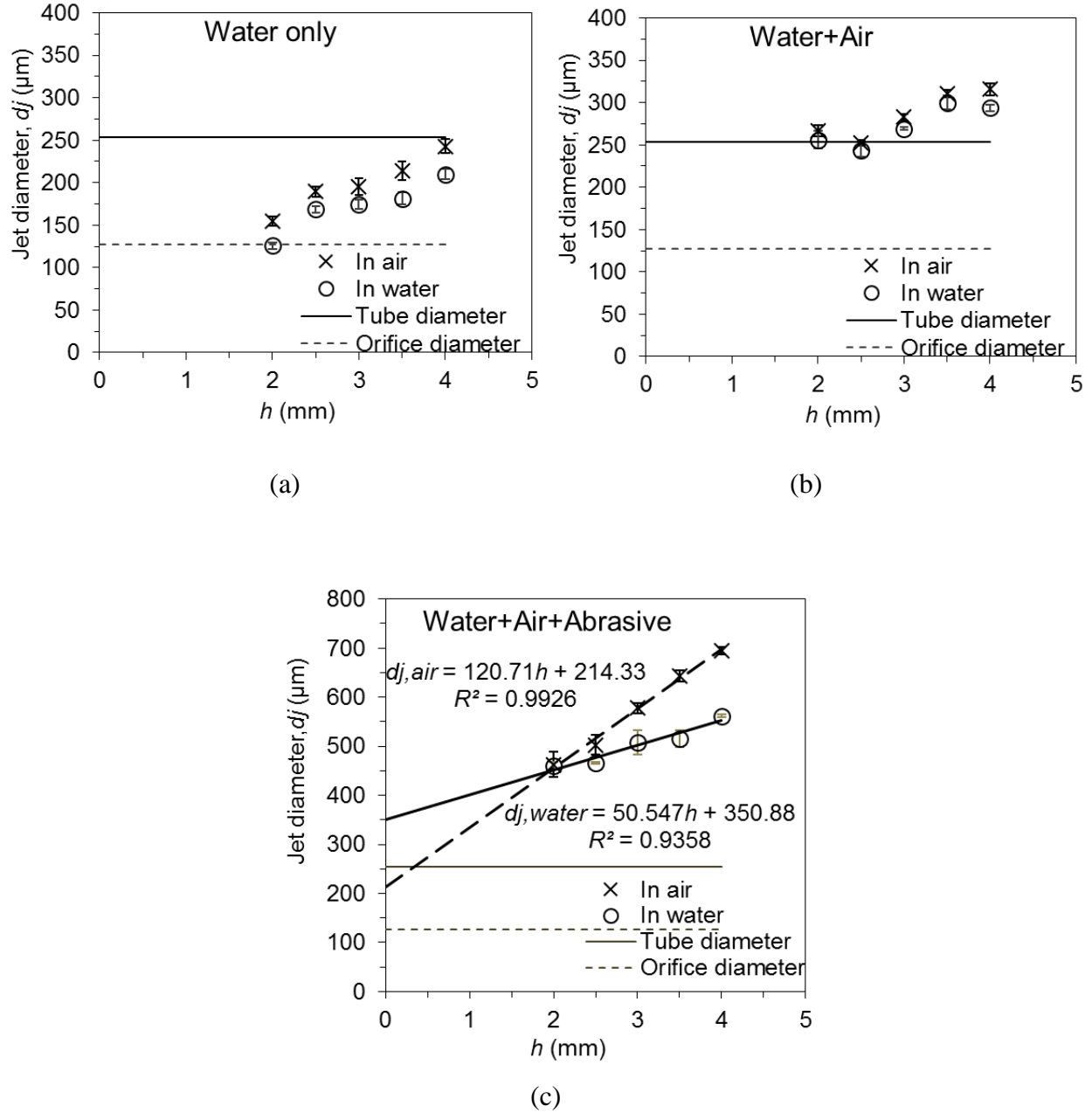
Figure 2-6 Effective jet diameters, d_j, from foam-board cuts when jet exited in air and in water for (a) Water-only jet; (b) Water+air jet; (c) Water+air+abrasive jet; P_p=138 MPa, V_t=4572 mm/min. Scatter bars represent ± 1 standard deviation. Mixing tube and orifice diameters shown for reference. Each of the data points and scatter bars represent the average width and standard deviation of a total of 24 measurements on 3 separate channels.

As mentioned previously, it is hypothesized that this was due to the increased drag on particles at the periphery of the submerged jet. Peripheral particles in air retained their velocity over a greater standoff distance, thereby machining wider channels in the foam; i.e. there was a greater effective jet diameter when the jet was in air (Figure 2-6c). This is consistent with Srinivasu et al. [77] who found that the jet axial velocity decreased as the jet diverged with increasing standoff distance. Statistical comparison of each pair of data points (t-test, $p<0.01$) in Figure 2-7 showed that single-pass channels ($d \leq 30$ μm) machined in the stainless steel and aluminum were significantly wider in air than in water, consistent with the effective jet diameter data of Figure 2-6c. Figure 2-7 also illustrates that the channels in SS316L were significantly narrower (t-test, $p<0.001$) than those in Al6061-T6, simply because a narrower cone of particles had sufficient velocity to erode stainless steel than in the case of aluminum, where more peripheral particles still had sufficient velocity to erode a channel.
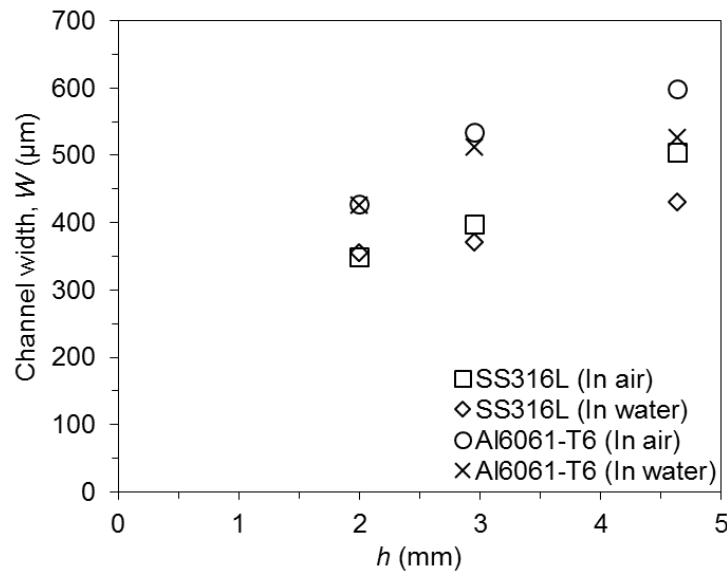
Figure 2-7 Channel width versus standoff distance in air and in water for SS316L and Al6061-T6 at P_p=138 MPa, V_t=4572 mm/min, Θ=90° (water+air+abrasive). Each of the data points represents the average width of 3 cross-sections, each being the average of 8 cross-sections taken from each of the three channels. Scatter bars representing ±1 standard deviation were small enough to fit within the symbols.

2.3.2. Channel shape and width

Figure 2-8 shows typical micro-channels with aspect ratios (depth/width) of about 1.2 machined under water using 30 passes for stainless steel and 10 passes for aluminum at P_P=138 MPa, V_t=1 m/min and h=2 mm. It is seen that the sidewalls were relatively steep so that the channel width increased only slowly with increasing depth. This is consistent with the creation of a filled portion of the channel having a constant aspect ratio, as mentioned previously.

(a)   (b)
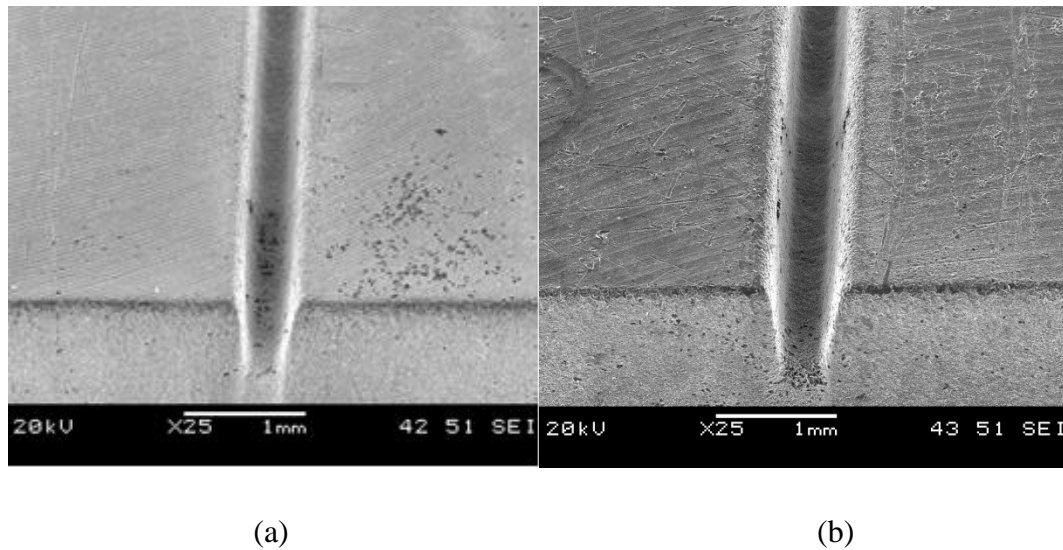
Figure 2-8 Scanning electron micrographs of channels with aspect ratio 1.2 in (a) SS316L (30 passes) and (b) Al6061-T6 (10 passes), machined under water at P_p=138 MPa, V_t=1000 mm/min, and h=2 mm.

Figure 2-9 shows that channels machined in air were slightly wider than those machined under water for the same depth, but the differences were relatively small. This agrees with the narrowing of the effective diameter of the submerged jet shown in Figure 2-6 and Figure 2-9 also reveals that the centerline depths of submerged and unsubmerged channels were approximately the same, because although the energy in the peripheral area of the AWJ in water was less than that in air, the energy in the jet core was equal in water and in air. This is discussed further in Section 2.3.3 (Figure 2-12).
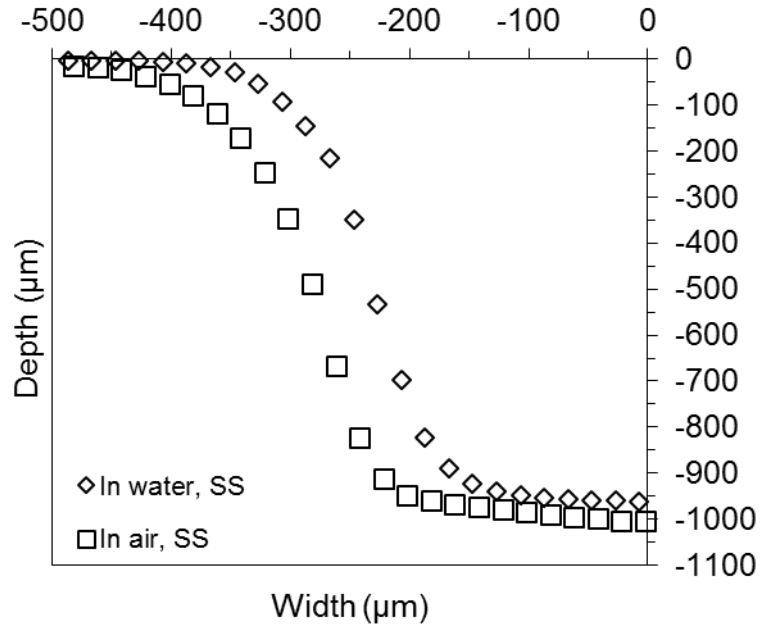
(a)
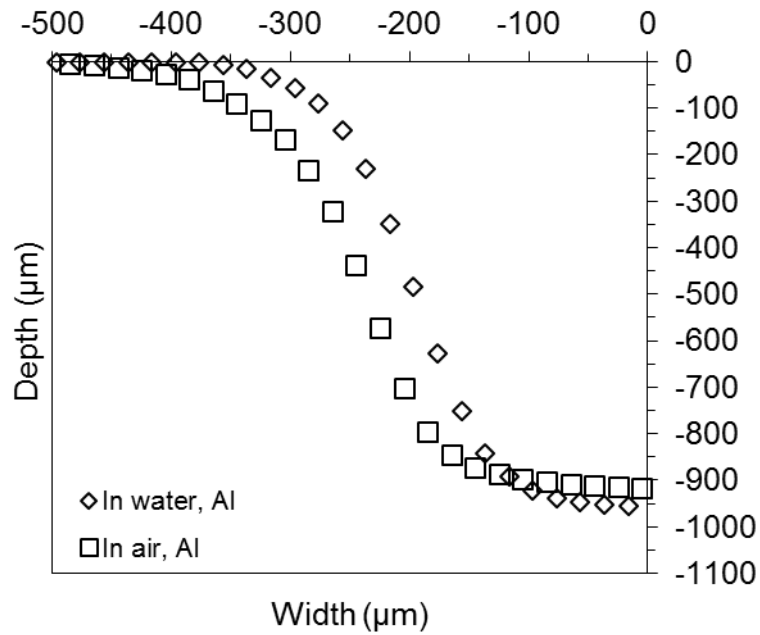
(b)

Figure 2-9 Comparison of half-channel shapes in water and in air for (a) 316L SS (30 passes), and (b) 6061-T6 Al (10 passes) at P_p= 138 MPa, V_t=1000 mm/min, Θ=90°, and h=3 mm.

2.3.3. Decrease of normalized instantaneous centerline erosion rate, E_{inst}, with channel depth

Figure 2-10 presents the centerline depth of channels, d, versus the expected depth, d_{exp}, for the two target materials, machined in water and in air at P_p=138 MPa, V_t=1000 mm/min, h=2, 3 mm with nozzle angles Θ=90° and Θ=30° for both backward (BW) and forward (FW) machining (Figure 2-4). As mentioned above, the expected depth (Eq. (2.1)) was calculated assuming that the erosion rate, measured using the shallow calibration channels, was maintained as the channels became deeper. The machining tests were performed using the standard conditions (Table 2.1; 38 μm garnet) (Figure 2-10a, b) as well as a larger size garnet with an average size of 75 μm (Figure 2-10c). It was found that a single power law curve (d=2.0441$d_{exp}^{0.850}$) could be fit to all of these data at both nozzle angles with R^2=0.991 with both abrasives. It is important to remember that d_{exp} (from Eq. (2.1)) incorporated the effects of spreading inherent in the use of the two standoff distances (h) and the two nozzle angles; i.e. the only effect not inherent in d_{exp} is the effect of stagnation within a channel. Therefore, Figure 2-10 shows that there was a progressive reduction in the measured centerline depth compared with the depth expected from the total incident energy of the abrasive jet (the latter being proportional to d_{exp}). This progressive decrease in the expected depth was attributed to the reduction in the particle velocity caused by stagnation effects within the confines of the deepening channel, and to continued spreading as the effective standoff to the bottom of the channel increased. A point by point statistical analysis of the experimental data points in Figure 2-10 (t-test, p>0.95) showed that the function relating the actual depth to the expected depth was independent of the two target materials tested, the nominal standoff distance, nozzle angle, particle size, and surrounding fluid.

As explained in Section 2.2.4.2, the slope of the power-law curve fit (d=2.04$d_{exp}^{0.850}$) in Figure 2-10, is equal to the instantaneous centerline erosion rate normalized by the corresponding value on a flat surface; i.e E_{inst}=1.74$d_{exp}^{-0.150}$, or in terms of the actual channel centerline depth, d, (d_{exp}=0.431$d^{1.17}$) as

$$E_{inst} = \frac{1.97}{d^{0.177}} \tag{2.8}$$

(a)

(b)

(c)
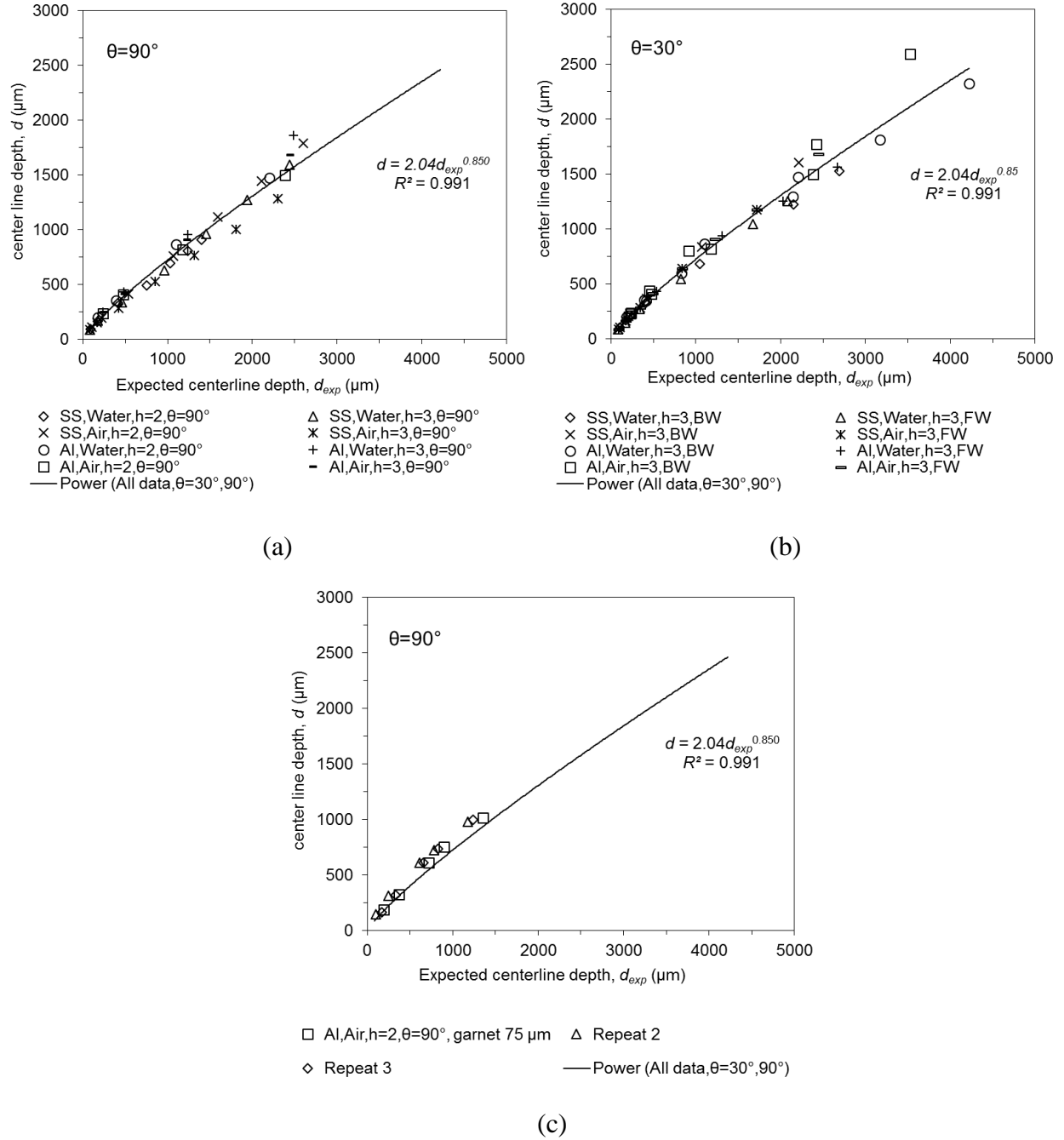
Figure 2-10 Channel centerline depth, d, versus the expected depth, d_{exp} (Eq. (2.1)) for micromilling with (a) normal nozzle angle, $\Theta=90°$, $h=2$, 3 mm, and (b) inclined nozzle angle, $\Theta=30°$, $h=3$ mm (backward and forward) in water and in air for SS316L and Al6061-T6, (c) using larger garnet particles (75 µm) at $\Theta=90°$, $h=2$ for Al6061-T6, $P_p=138$ MPa, $V_t=1000$ mm/min. Each of the data points represents the average depth of a total of 24 measurements on three channels. Scatter bars representing ±1 standard deviation were small enough to fit within the symbols.

Figure 2-11 shows the dependence of the normalized instantaneous centerline erosion rate (E_{inst}) on channel depth, Eq. (2.8), for both target materials at nominal standoff distances of h=2 and 3 mm for both submerged and unsubmerged machining at normal (θ=90°) and inclined (θ=30°) nozzle angles. As with Figure 2-10, E_{inst} was independent of the target material, the initial (nominal) standoff distance, h, and whether the jet was submerged or not. Therefore, the decrease in the normalized instantaneous centerline erosion rate (E_{inst}) was only a function of the channel depth for the given jet diameter. Figure 2-11 shows that stagnation effects within the confines of the channels and the increased jet spreading caused the normalized instantaneous centerline erosion rate to decrease by up to 40% of its initial value at a channel depth of 800 µm.

Similar trends were apparent in the behavior of the volumetric erosion rate as a function of the channel centerline depth. The principal difference was that the volumetric erosion rate decreased less with increasing depth than did the centerline erosion rate. This was a consequence of how the channel width also changed with depth.
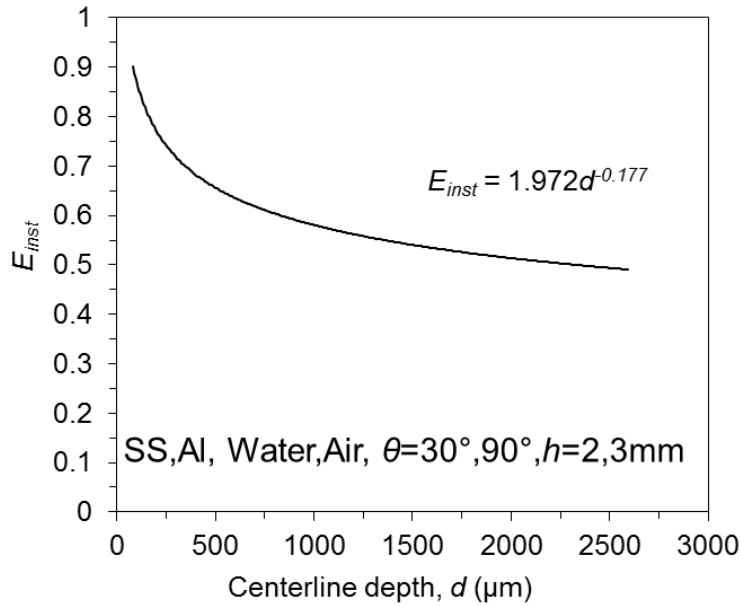
Figure 2-11 Normalized instantaneous centerline erosion rate, E_{inst}, versus channel centerline depth, d, for channels machined in air and submerged in water for SS316L and Al6061-T6 at nozzle angles, Θ=30°, 90°, P_p=138 MPa, V_t=1000 mm/min, h=2, 3 mm.

As mentioned above, it is hypothesized that the decrease in the normalized instantaneous centerline erosion rate with increasing channel depth, d, seen in Figure 2-11, was due to continued jet spreading and a further decrease in particle velocity resulting from drag within the stagnation zone near the bottom of the channel. The increase in the spreading effect (relative to the spread of the jet on the initial flat surface) was a function of the total effective standoff, h_{total}, between the nozzle and channel bottom $(h+d)$, and was quantified by measuring the depths of shallow channels ($d \leq 50$ µm) at 5 standoff distances between $h=2$ and 5 mm. It was assumed that the stagnation effect in such shallow channels was relatively small compared with the deeper channels of Figure 2-10.

Figure 2-12 shows these shallow channel depths normalized by the depth of the channel machined at $h=2$ mm, E_h^*, for the two target materials at a highest scan speed, $V_t=4572$ mm/min, $P_p=138$ MPa, and nozzle angles $\theta=45°$, 90°.
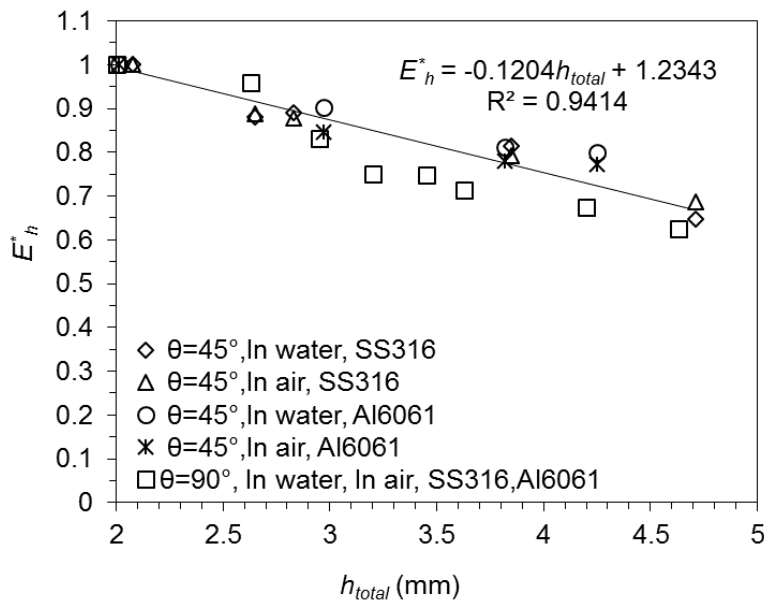
Figure 2-12 Shallow channel depth normalized by that at $h=2$ mm, E_h^* as a function of total effective standoff distance to the bottom of each shallow channel, h_{total}, for $\theta=90°$ (solid line) and $\theta=45°$ in water and in air. SS316L and Al6061 at $P_p=138$ MPa, and $V_t=4587$ mm/min. Each of the data points represents the average depth of a total of 24 measurements on three channels. Scatter bars representing ±1 standard deviation were small enough to fit within the symbols.

31

A statistical analysis was performed to compare the slopes of lines fitted for the different machining conditions (note: for all conditions at h=2 mm, E_h^*=1). With a high probability (t-test, p>0.9), the effect of standoff distance in water and in air machining was the same. As expected for this spreading effect, the decrease in E_h^* with increasing h was independent of the target material, the jet inclination, and whether the jet was submerged or in air.

The decrease in the normalized centerline depth due to increased spreading seen in Figure 2-12, can be superimposed on the data of Figure 2-11 to show how much of the normalized centerline erosion rate decrease with depth was due to flow stagnation in deeper channels. Figure 2-13 shows these two effects, with the difference between the solid line, representing E_h^*, and the instantaneous erosion rate, E_{inst}, being due to the effect of the growing stagnation zone in channels as they become deeper. This is consistent with the CFD modelling of waterjet particle velocities in channels of various depths and widths of Matsumura et al. [97] and Lv et al. [98].
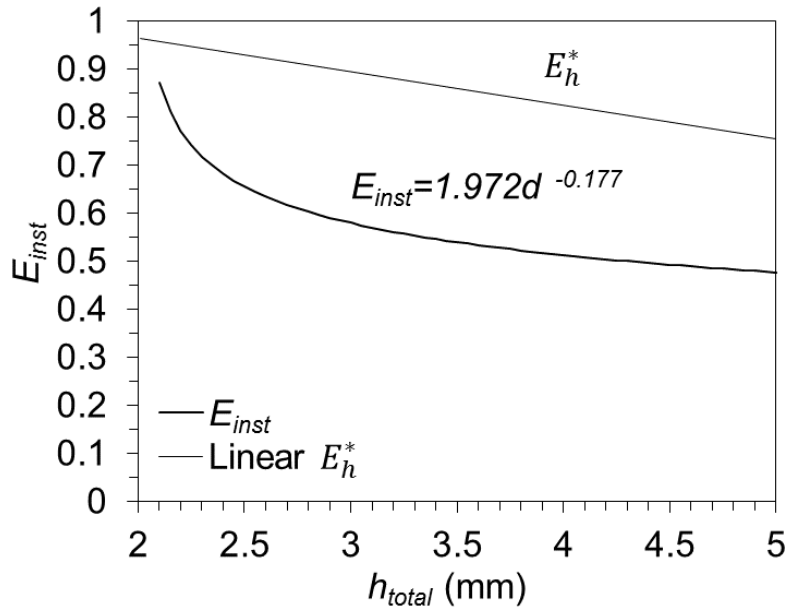
Figure 2-13 Normalized instantaneous centerline erosion rate, E_{inst} (Figure 2-11) and the amount of it due to jet spreading, E^*_h (Figure 2-12) as a function of total effective standoff distance, h_{total}. Data for Al6061-T6 and SS316L machined in water and in air, at θ=30°, 90°, h=2 mm, P_p=138 MPa, V_t=4587 mm/min.

It is intriguing that the reduction in E_{inst} due to the stagnation zone seen in Figure 2-13, increases quickly to approximately h_{total}=3.4 mm ($d\approx$1 mm), but then becomes constant so that further decreases are attributable to spreading alone; i.e. the slopes of the two curves become roughly equal. It is hypothesized that this was probably a consequence of attaining an approximately constant value for the aspect ratio of the filled portion of the channel cross-section; i.e. the depth to width ratio of the part of the cross-section that is effectively filled with water within the footprint of the jet. This is consistent with the observation of Section 2.3.2, that the channels in steel and aluminum had essentially the same cross-sectional shapes, which did not change appreciably with depth since the side walls were quite steep.

This hypothesis was explored further by comparing the curves of Figure 2-10 for the two metals with the behavior of glass, as shown in Figure 2-14a. In this case, channels were made in borosilicate glass plates (Borofloat®, Schott Inc., NY, USA) when submerged and in air with a high scan speed (V_t=4572 mm/min) and n=1, 2, 4, 6, 8 passes (Θ=90°, h=2 mm, P_p=138 MPa). A statistical analysis comparing the slopes of the two curves (Figure 2-14a) showed that the progressive reduction in the expected depth was significantly greater in glass than in the two target metals (t-test, $p<0.001$). This is consistent with the greater V-shape of channels made in glass than in metal, as shown in Figure 2-14b. It is hypothesized that the narrower glass channels would be filled to a higher level by the jet flow within the footprint, and that this would produce a greater stagnation zone reduction of the erosion rate. Thus, the channel shape can affect the depth of water within the channel, which in turn affects the relationship between the expected depth and the actual depth. Target materials that erode to produce similarly shaped channels result in similar decreases in instantaneous erosion rate.
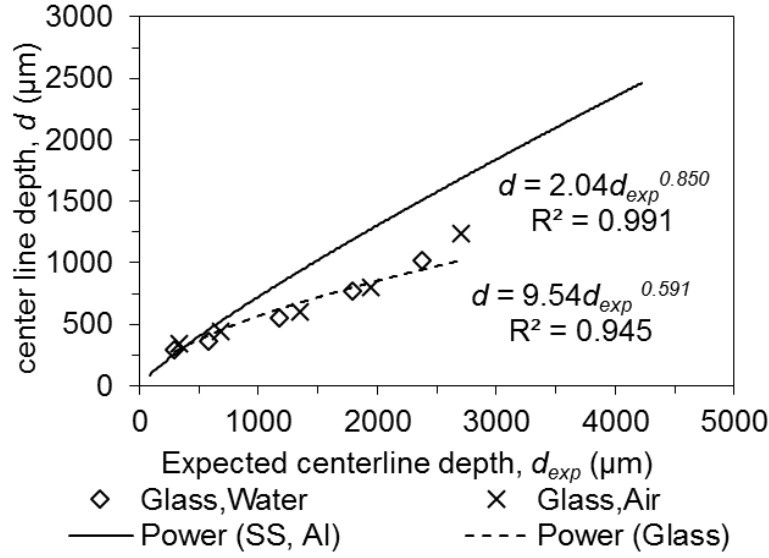
(a)
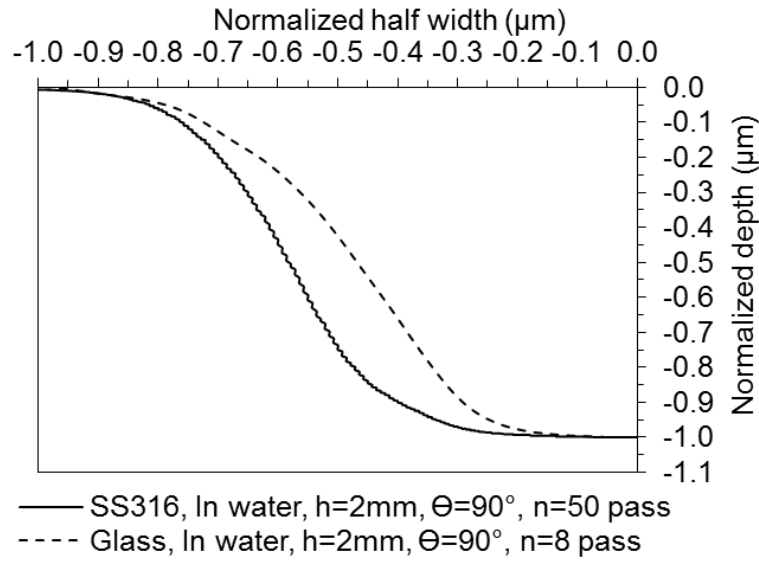
(b)

Figure 2-14 (a) Comparison of channel centerline depth, d, versus the expected depth, d_{exp} (Eq. (2.1)) for channels machined in glass (data points and dashed curve) and metals (solid curve, data of Figure 2-10). (b) Normalized cross-sectional shapes of channels with the same depth ($d \approx 1\text{mm}$) machined in water in SS316 ($n=50$ passes) with $V_t=1000$ mm/min and glass ($n=8$ passes) with $V_t=4572$ mm/min at $\Theta=90°$, $h=2$ mm, $P_p=138$ MPa. Each of the data points represents the average depth of a total of 24 measurements on three separate channels. Scatter bars representing ±1 standard deviation were small enough to fit within the symbols.

2.4. Summary

The abrasive water jet micro-machining of channels in aluminum and stainless steel was compared in the submerged and unsubmerged conditions for a range of angles and standoff distances. It was found that the channels machined using the unsubmerged jet were significantly wider than those machined with the submerged jet because of increased drag on the jet periphery. This was true for water-only jets, jets with entrained air, and jets with entrained air and particles. Moreover, the instantaneous centerline erosion rate and volumetric erosion rates decreased with channel depth. It was established that this was due to the combined effects of jet spreading with increase effective standoff distance and the jet stagnation zone at the bottom of the channel within the footprint of the jet. The decrease in erosion rate due to the stagnation zone was shown to be only a function of channel geometry, and was independent of the standoff distance, jet angle, jet direction (forward or backward machining) and whether the jet was submerged or in air. A major advantage of submerged abrasive waterjet micro-machining compared to its use in air, is that it is possible to machine narrower channels, thereby increasing the resolution of the process without reducing the centerline etch rate. Submerged AWJ micro-machining also has the additional benefits of reducing noise and releasing less abrasive debris to the air. In Chapter 3, the data from this chapter will be used to develop a model to predict the cross sectional channel shapes resulting from submerged and unsubmerged AWJM.

Chapter 3 Abrasive Waterjet Micro-Machining of Channels in Metals: Model to Predict High Aspect-Ratio Channel Profiles for Submerged and Unsubmerged Machining

This chapter is based on the following published paper:

N. Haghbin, J. K. Spelt, and M. Papini, "Abrasive waterjet micro-machining of channels in metals: Model to predict high aspect-ratio channel profiles for submerged and unsubmerged machining," *Journal of Materials Processing Technology*, vol. 222, pp. 399-409, 2015.

3.1.Introduction

Micro-channels with a wide range of low to high aspect ratios (i.e. depth/width) have many applications in micro-electromechanical systems (MEMS) and micro fluidics systems, such as those in lab-on-chip devices [105], microchip electronic cooling systems [106], biomedical micro-devices [107], biochemistry [107], and electrophoretic applications [109]. Abrasive water jet micro-machining (AWJM) is an attractive technology for producing micro-channels because of its ability to machine a wide range of ductile and brittle materials with no heat affected zone, minimal residual stress, and relatively little edge damage.

To obtain a micro-channel of a given required aspect ratio with a low waviness and roughness, the AWJM process must be precisely controlled. This is most easily accomplished using multiple passes at a relatively high scan speed. Researchers such as Agus et al. [110] have also found that using this multi-pass strategy is an efficient solution because it decreases surface waviness, and reduces total costs associated with the purchase of spare parts, energy, and abrasive. Furthermore, Wang and Guo [111] found that, for the same machining time, multi-pass AWJ milling in ceramics at a high traverse speed can result in a higher material removal and lower surface roughness than single-pass machining with a slow traverse speed. Shipway et al. [28] also showed that using a high traverse velocity and multi-pass machining in titanium results in a lower roughness and waviness of channels than a single pass at a low traverse velocity. The present work thus focuses on the development of a model to predict the depth and shape of micro-channels made using multiple nozzle passes.

The first relatively simple mathematical models of AWJ machining could predict only the depth of cut made by relatively large nozzles, rather than the actual channel shape as it is milled and becomes deeper. For example, for water-only jets, Crow [112] derived an equation for depth as a function of water velocity and the properties of the target (rock), and Rehbinder [113] developed a model to predict the water pressure required to reach a required depth in the cutting of rock. Hlavac and Vasak [114] proposed an energy approach to express the depth of a deep cut made by a water-only jet in rock in terms of the initial jet velocity, traverse velocity, cutting time, and the strength of the rock. In AWJ machining, Hashish [115] presented a model to predict the depth of cut in ductile materials as a function of the different abrasive waterjet parameters (i.e. water pressure, abrasive flow rate, traverse velocity, and jet diameter).

A key step for controlled-depth abrasive water jet (AWJ) milling is to develop a model to predict the size and shape of the channel cross-sectional profile [49]. Alberdi et al. [9] modelled the kerf shape of a straight channel in aluminum 7075-T651 as a Gaussian bell function using the maximum channel depth, maximum width, and the width at half of the maximum depth as parameters. Freist et al. [10] defined the kerf shape for AWJ milling in ceramics using a cosine function. Laurinat et al. [11] described channel kerf profiles in different materials using modified cosine functions, and related their model to the standoff distance and the traverse feed rate. They divided the kerf profile in two zones, and developed analytical models for the total depth of cut in the case of ductile materials. Wang [116] presented an empirical model using a dimensional analysis technique to determine the depth of cut in alumina ceramic, but the model did not predict the shape and width of channels. Ojmertz and Amini [117] used statistical methods such as interpolation and regression analysis to model the shapes of channels in a milling process, but these types of empirical approaches require many experiments, varying a large number of parameters, and must be repeated for each target material/abrasive powder combination. Artificial intelligence approaches, such as the genetic algorithms applied by Carrascal and Alberdi [118], also require a great deal of data spanning the range of the many machining parameters in order to predict the kerf profile in AWJ machining. Simulation approaches to predict the shape of AWJ milled footprints, such as the finite element methods presented by Anwar et al. [119] or the unit event approach used by Lebar and Junkar [120] require long computational times and many simplifying hypotheses.

A mathematical model to predict relatively shallow AWJ milled surface profiles or 'footprints' using a relatively large nozzle (mixing tube diameter of 1 mm, with an average garnet particle size of 180-300 µm), was developed by Axinte et al. [53] for brittle materials with the jet incident perpendicular to the surface, i.e., at a 90° jet impact angle. This model for brittle materials was subsequently applied to single straight paths in a titanium alloy, normally considered to be a ductile material, for moving jets with arbitrary angle [49], and for overlapped single and multiple straight paths in titanium [54]. This footprint approach is similar to that pioneered by Ghobeity et al. [58] that utilized a shallow first pass profile in order to determine the erosive efficacy of the blasting system in the prediction of the surface evolution of features machined in glass using abrasive air jet micro-machining (AJM). This AJM methodology has also been extended so that it could be used for ductile materials such as polymethylmethacrylate (PMMA) at both normal and oblique angles of attack [19,121], and to metals [21]. Nouraei et al. [122] also successfully applied the AJM model for brittle materials to the abrasive slurry jet micro-machining of borosilicate glass.

While useful for planning the milling of relatively wide and shallow features, the footprint models developed thus far for AWJ using relatively large nozzles (1 mm) are not appropriate for the presently considered multi-pass micro-machining of high aspect-ratio channels. As machined features become deeper, the local impact angle on the steep sidewalls changes. Oka et al. [59] and many others have shown that for ductile materials, the erosion rate depends strongly on the impact angle. Since the current AWJ footprint models do not consider this dependency, they are appropriate only for shallow and wide features, and have therefore been tested only up to an aspect ratio (ratio of feature depth to width) of 0.4. The earlier AJM surface evolution models, on the other hand, do consider this dependence on the local impact angle, as well as other complications associated with the prediction of very high aspect-ratio features (up to 2.5), such as the use of curvature-dependent smoothing [78] near rapid changes in sidewall slope.

Haghbin et al. [123] presented erosion rates and cross-sectional profiles of micro-channels in SS316L and Al6061-T6 made using a novel prototype miniaturized nozzle with a 254 µm mixing tube operating in air and when submerged under water. They showed that submerged AWJM, which is used to reduce dust and noise, produces narrower channels than those made in air without a reduction in the centerline etch rate. In contrast to micro-channels machined using air driven AJM, the instantaneous centerline erosion rate and volumetric erosion rates decreased with channel

depth due to jet spreading with increased effective standoff distance and the jet stagnation zone at the bottom of the channel within the footprint of the jet. The decrease in erosion rate due to the stagnation zone was only a function of channel geometry, and was independent of the standoff distance, jet angle, jet direction (forward or backward machining) and whether the jet was submerged or in air. These effects were captured conveniently by defining a centerline instantaneous erosion rate that was normalized by the erosion rate of a shallow channel at the same effective standoff distance, E_{inst}. This normalized instantaneous centerline erosion rate decreased with increasing centerline depth, d, according to a single master power-law curve that reflected the increase in the stagnation zone size. In addition to being independent of the nozzle-to-surface standoff distance via the normalization, E_{inst} was independent of target material (glass or metal) and the surrounding fluid (air or water).

This chapter demonstrates that the erosive efficacy distribution also changes with channel depth, reflecting changes in the local particle impact angles within a deepening machined channel. Previous AWJM models have not considered these changes and are, therefore, limited to relatively shallow channels. The new model can predict the shapes of channels machined in water and in air on 6061-T6 aluminum alloy and 316L stainless steel targets up to aspect ratios of 3.2. Since these targets span a wide range of material properties such as hardness and density that are known to strongly affect the erosion rate, the model is expected to be generally applicable to a wide variety of metals and other ductile materials.

3.2. Experiments

3.2.1. Micro-machining of high aspect ratio channels

The experimental setup and the AWJ parameters and procedure are described in detail in section 2.2.1. Briefly, an OMAX 2626 Jet Machining Centre (OMAX Corp., Kent, Washington, USA) fitted with a prototype nozzle having an orifice diameter, d_O, of 127 µm and a 254 µm mixing tube (i.e. focusing or collimating tube) diameter, d_M, with a 28 mm mixing tube length, L_M, was used to machine straight micro-channels up to an aspect ratio of 3.2 in aluminum 6061-T6 and stainless steel 316L target samples. The prototype nozzle was a 5/10 MAXJET 5, which had the same nozzle body as the 7/15 Mini MAXJET 5 (OMAX part no. 305764-07) as discussed by Liu and Sagawa [124] (i.e. only the mixing tube and orifice were changed). The water flow rate at a

machining pressure of P_p=138 MPa was 0.213 L/min. Figure 3-1 presents the size distribution and an image of the treated 320-mesh garnet (Barton International, Glens Falls, NY, USA) with an average equivalent spherical diameter of 38 µm used in all experiments. The abrasive mass flow rate, $\dot{m}_a$, was varied between 0.6 and 1.1 g/s.
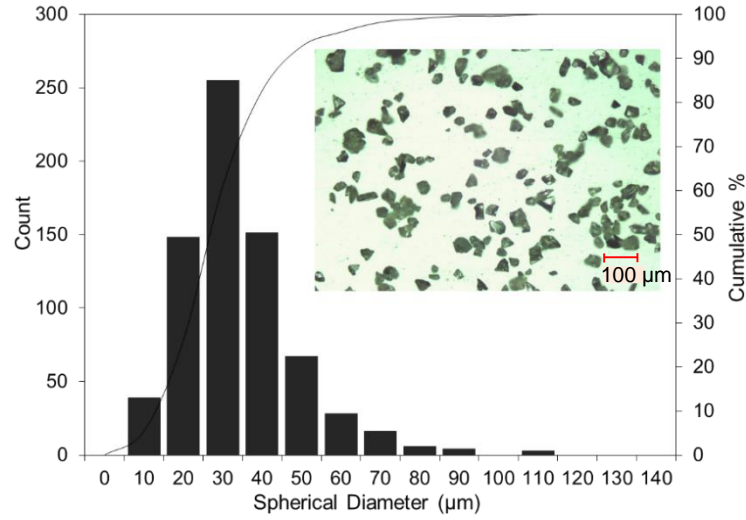
Figure 3-1 The size distribution and shapes of the surface-treated320-mesh garnet. Scale bar represents 100 µm.

The straight micro-channels were machined using multiple nozzle passes (up to n=50) at a traverse velocity of V_t=1000 mm/min with global nozzle inclinations of θ= 90° and 30°. Nozzle to surface standoff distances of h=2, 3 mm (Figure 3-2a) were used, and both the nozzle tip and the workpiece were either in air or were submerged in water. The θ=30° experiments were performed both in the 'forward' and 'backward' configuration (Figure 3-2a). The resulting micro-channel cross-sectional profile shapes were measured using a non-contact optical profilometer (model ST 400, Nanovea, Irvine, CA, USA) having a lateral and vertical resolution of 0.1 µm.

Channel centerline depths were recorded as the average and standard deviation of 24 total measurements; i.e. 8 measurements within a 2 cm long machined channel, repeated on three separately machined channels. Channel to channel scatter was similar to scatter within a channel.

40

The average cross-sectional profile of these three 2 cm channels was then, taken as the one of these 24 profiles which had a centerline depth equal to the average value. The overall standard deviation among the channel centerline depth was 28 µm.
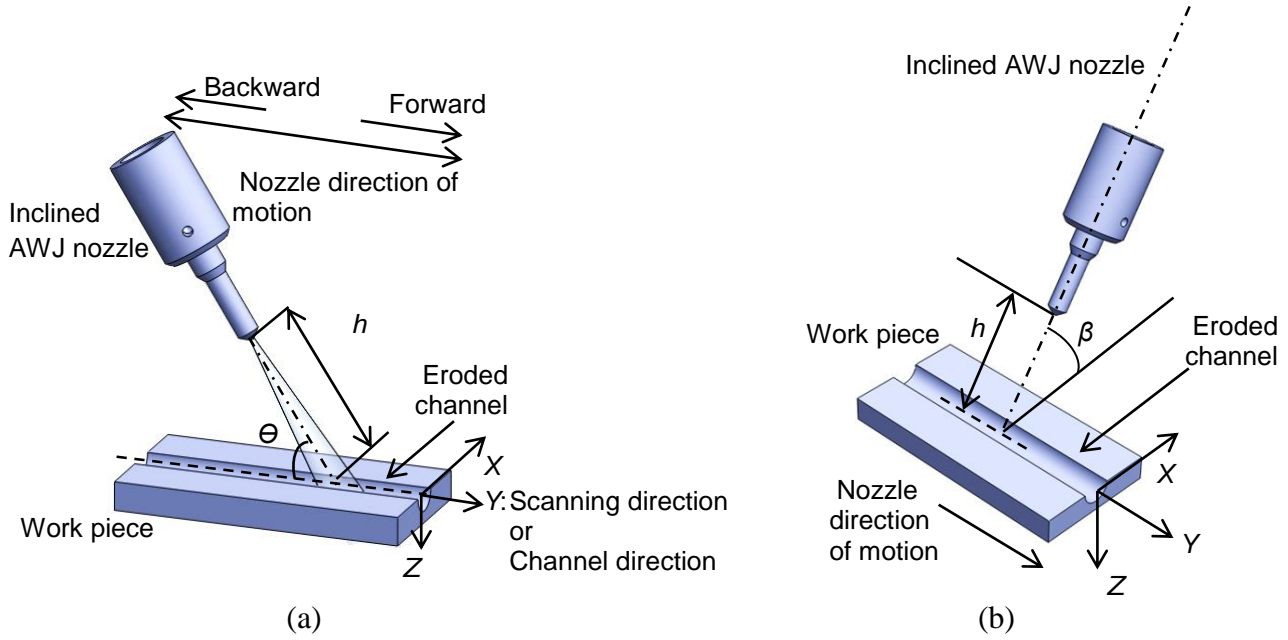
Figure 3-2 (a) Setup used for (a) micro-milling with nozzle at global angles of $\Theta=30°$, 90°, and standoff distance, h, and (b) measurement of erosion rates on nominally flat surfaces using very shallow channels as function of global angle β. Not to scale.

3.2.2. Measurement of erosion rate versus angle of attack

The erosion rate, E, generally depends on the angle, β, between the incident particles and the target according to

$$E(\beta) = \frac{M_m}{M_a} \tag{3.1}$$

where M_m and M_a are the total mass of target material removed and the total mass of abrasive incident to the target surface, respectively. The use of very shallow channels ensured that the local impact angles, α, within the jet footprint (Figure 3-3) were unaffected by the slope of the channel walls and were approximately equal to the global angle of the nozzle, β (Figure 3-2b). It was

41

further assumed that incident particle trajectories were largely unaffected by streamline deflection within the footprint area [120], and that the effect of the shallow sidewall slope on the size of the stagnation zone was negligible. Therefore, under these conditions, the jet angle β was equal to the local impact angle α.
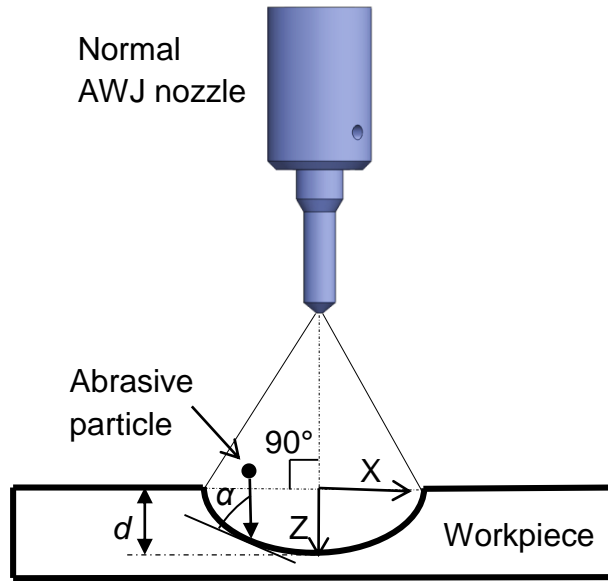
Figure 3-3 AWJ nozzle at angle θ=90° when machining a deep channel (Figure 3-2a) and local impact angle (α) of abrasive particles.

The function $E(\beta)$ was determined for the 6061-T6 aluminum alloy and 316L stainless steel by machining very shallow (<50 µm) channels using a scan speed of 4572 mm/min at β=15°, 30°, 45°, 60°, 90° at h=3 mm as shown in Figure 3-2b. This configuration, i.e. with the nozzle axis perpendicular to the scanning direction at all angles, was used in order to minimize erosion that may be caused by flow parallel to the target, beyond the initial blast zone of the jet. The removed target mass was calculated by measuring the average channel cross-sectional area, A_m, and multiplying by the channel length and target density (stainless steel: 8027 kg/m^3, aluminum: 2700 kg/m^3). The mass of abrasive incident to the channel was found by collecting and weighing the abrasive exiting from the abrasive hopper during the machining time. The average volume of

eroded material was calculated using the average channel cross-sectional profile as defined in Section 3.2.1.

The normalized dependence of the erosion rate on β was expressed as,

$$g(\beta) = \frac{E(\beta)}{E(90°)} \tag{3.2}$$

where $E(\beta)$ and $E(90°)$ are the erosion rates (g/g) at a given global angle of attack, β, and at normal incidence (β=90°), respectively. The function $g(\beta)$, or equivalently, $g(\alpha)$, where α is the local angle of impact, was fit to the following expression [59]:

$$g(\beta) = (sin\beta)^{n1}(1 + HV(1 - sin\beta))^{n2} \tag{3.3}$$

where the first term is associated with erosion due to repeated plastic deformation, and the second term is related to erosion due to cutting. The constants n_1 and n_2, which are fitted using the erosion versus angle of attack data, depend on particle type, hardness and size, and the impact conditions, while HV (GPa) is the initial Vickers hardness of the target.

3.3. Surface evolution modelling

3.3.1. Original AJM model

Getu et al. [57] developed a surface evolution model for air-driven abrasive jet micro-machining (AJM) of ductile polymers. The model was adapted for use in the AJM of metals by Ally et al. [21]. The partial differential equation describing the general surface evolution in this case is

$$z^*_{,t^*} = Q^*(x^*) \cdot \left(\sqrt{(1 + z^*_{,x^*}(x^*, t^*)^2)} \right) \cdot g(\alpha) \cdot \left[1 - \varepsilon \cdot \frac{z^*_{,x^*x^*}(x^*, t^*)}{(1 + z^*_{,x^*}(x^*, t^*)^2)^{\frac{3}{2}}} \right] \tag{3.4}$$

43

where the starred letters represent the dimensionless depth and width coordinates $z^*=z/h$, $x^*=x/h$, respectively, that have been normalized by the standoff distance h (Figure 3-2). The terms $z^*_{,t^*}$, and $z^*_{,x^*}$ are the derivatives of z^* with respect to t^* and x^*, respectively. The dimensionless machining time is $t^*=t/T$, where t is the machining time after n passes to reach a depth z. The time constant, T, is the number of passes, assuming a constant erosion rate, required to propagate the surface at the channel centerline (i.e. $x=0$), to a centerline depth z equal to h; i.e. $z^*=1$. The term $Q^*(x^*)$ represents the potential of the abrasive jet to erode the target, the so-called non-dimensional "erosive efficacy", defined as

$$Q^*(x^*) = V^*(x^*)^K \phi^*(x^*) \qquad (3.5)$$

where $V^*(x^*)=V(x^*)/V(0)$ is the dimensionless particle velocity distribution at the surface, K is the velocity exponent, and $\phi^*(x^*)= \phi(x^*)/\phi(0)$ is the dimensionless particle flux. Therefore, the erosive efficacy represents the amount of erosion at a given transverse coordinate, x^*, normalized by the value at the center of the channel. The model in Eq. (3.4) assumes a constant centerline erosion rate, an assumption that was found to be valid for AJM of channels and holes up to aspect ratios of 2.5 and 1.2, respectively [57,121].

Haghbin et al. [123] found that the erosion rate in the AWJ machining decreased with increasing channel depth due to the continued spreading of the jet and the increase in the size of the stagnation zone. These two effects were modelled using a normalized instantaneous centerline erosion rate, E_{inst}, equal to the slope of a plot of the actual centerline depth after n passes (d_n) versus the expected depth at that time (d_{exp}); i.e. $E_{inst}=d_n/d_{exp}$. It was showed that E_{inst} decreases with the centerline depth according to

$$E_{inst} = \frac{A}{[z^*(0,t^*).h]^B} \qquad (3.6)$$

where A and B are 1.972 and 0.177, respectively, for SS316L and Al6061-T6 regardless of whether the jet is in or out of water [123]. The term $z^*(0,t^*)$ is the normalized depth of the channel at the

centerline ($x^*=0$) at standoff distance, h, and a normalized time t^*. Therefore, E_{inst} is just the ratio of the centerline erosion rate in a channel at depth z^* and the corresponding value on a flat surface at a standoff distance equal to z^*. Consequently, the erosive efficacy could be corrected to account for the effect of the footprint stagnation zone at depth z^* by multiplying by E_{inst}; i.e.

$$Q_{inst}^*(x^*) = E_{inst} \cdot Q^*(x^*) \qquad (3.7)$$

This instantaneous erosion efficacy $Q_{inst}^*(x^*)$ was then used in Eq. (3.4) instead of the constant erosion efficacy, $Q^*(x^*)$, that was used in the original AJM model.

The last term in Eq. (3.4) is a curvature-dependent smoothing term, ε that is necessary to improve accuracy and maintain stability in the solution of the partial differential equation in cases where the profile has a relatively sharp corner. Guidelines for the choice of ε, based on the aspect ratio of the channel, can be found in Ghobeity et al. [78]. In the present work, values between 0.001 and 0.01 were appropriate.

3.3.2. Erosion rate as function of global angle of incidence, $g(\beta)$

The measured $g(\beta)$ functions in Eq. (3.2) are shown in Figure 3-4 for the SS316L and Al6061-T6. These relationships were effectively independent of the surrounding medium of air or water. The best fits to Eq. (3.3) were found using a non-linear least-squares curve fit in Mathcad 14 (Mathsoft Engineering & Education, INC., Cambridge, MA, USA). The fitted exponents n_1 and n_2 and the nominal Vickers hardness, HV, were 1.578, 37.184, 1.373 (GPa) for SS316L, and 1.808, 40.292, 0.981 (GPa) for Al6061-T6. While Oka et al. [59] correlated n_1 and n_2 to particle and target properties reflecting brittle and ductile contributions to erosion, following the work of Ally et al. [21], the present work utilized Eq. (3.3) to provide only the functional form for an empirical curve fit without these interpretations.

The curve fits of Eq. (3.3) indicated that the maximum erosion rates for Al6061-T6 and SS316L occurred between 20° and 30°, indicating a ductile erosion response similar to that reported by other authors for these materials. For example, Ally et al. [21] reported that the maximum erosion rates of stainless steel, aluminum, and titanium alloys blasted using air abrasion with 50 μm aluminum oxide particles occurred between 20° and 35°, similar to the finding of Oka

45

et al. [59] for ductile materials air blasted with 325 µm silica sand particles. This indicates that particle divergence within the footprint of the water jet did not have a significant effect on the average impact angle, which could still be represented by the jet angle, β.
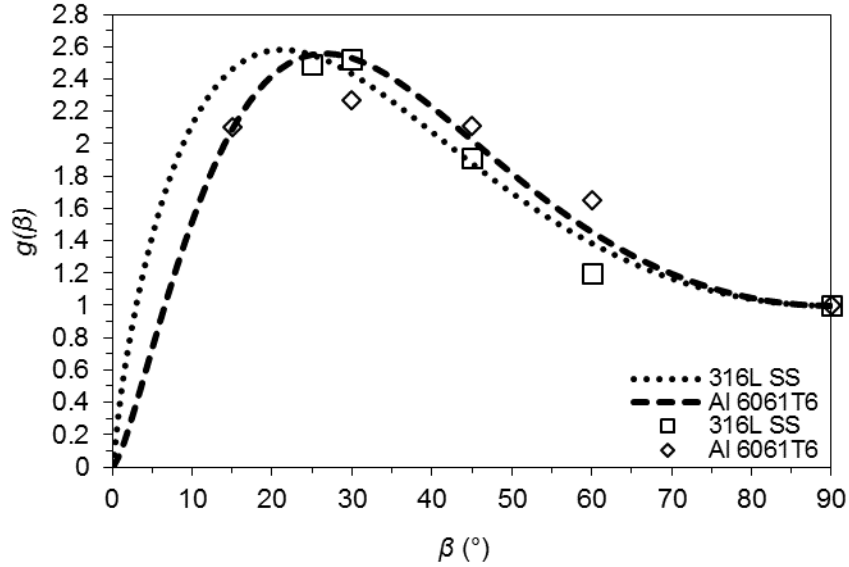
Figure 3-4 Normalized erosion rate, $g(\beta)$, as a function of global angle, β, for Al6061-T6 and SS316L at nozzle angles β=15°, 30°, 45°, 60°, 90°, P_p=138 MPa, V_t=4572 mm/min. Dashed lines indicate best fit to Eq. (3.3). Each of the data points represents the average depth of a total of 24 measurements on three separate channels. Scatter bars representing ±1 standard deviation are small enough to fit within the symbols.

Referring to Figure 3-3, the local impact angle on the channel sidewall, α, is given by

$$\alpha = \left(\frac{\pi}{2} - arccos\left(\frac{1}{\sqrt{1+z^*_{,x^*}{}^2}} \right) \right) \tag{3.8}$$

As mentioned above, for very shallow channels (depth≤ 50 µm), the local impact angle of the abrasive particles and the nozzle angle are approximately equal (β=α). Therefore, once the

function $g(\beta)$ has been determined from Eq. (3.2), it can be used in Eq. (3.4) by replacing β with α. It is noted that in ductile materials, the local erosion rate on the sidewalls increases as the channels become deeper, since the local angle, α, decreases.

3.3.3. Predicted micro-channel profiles using modification for abrasive flow-rate fluctuations

Haghbin et al. [123] that found that the fluctuation of abrasive mass flow rate over time that commonly occurs in AWJ operations can be quantified by periodically machining shallow, two-pass calibration channels during the machining experiments. This led to the following expression for the expected depth of a channel after N passes that includes the effects of the measured abrasive flow rate fluctuations

$$d_{exp} = \int_0^N d_{cal}(n)dn \qquad (3.9)$$

where the function $d_{cal}(n)$ is a curve fit of 5th order polynomial to the centerline depths of the calibration channels measured after $n=2$, 4, 10, 20, 30, 40, and 50 passes during the course of a machining experiment to create a stepped channel [123]. The time, t_N, to reach the expected depth, d_{exp}, after N passes is just the product of N and the time per pass as determined by the scanning speed and length of channel. Recalling that Eq. (3.4) assumes a constant erosion rate, it is necessary to correct the dimensionless machining time, $t^*=t/T$, so that t and T correspond to an effective, constant centerline erosion rate (μm/s), chosen here to be the value measured in the first two-pass calibration channel, E_0, at standoff distance, h. Therefore, the corrected time, t_c and the corrected time constant, T_c, used in Eq. (3.4) are defined as

$$t_C = \frac{d_{exp}}{E_0} \qquad (3.10)$$

$$T_C = \frac{h}{E_0} \qquad (3.11)$$

which is equivalent to $t_c=t_N/t_2$, and the corrected time constant $T_c=T/t_2$.

Figure 3-5a shows an example of predicted and measured profiles, expressed in dimensional form, using the original AJM model with the initial condition $z^*(x^*,0)=0$. The effect of abrasive

flow rate fluctuations was eliminated using Eq. (3.9). The method of lines implemented in Mathcad 14 (Mathsoft Engineering & Education, Inc., Cambridge, MA, USA) was used to solve Eq. (3.4) and obtain the predicted multi-pass normalized micro-channel profiles. The non-dimensional time step was $\Delta t^* = 120$ and the non-dimensional coordinate step was $\Delta x^* = 120$.

(a)   (b)
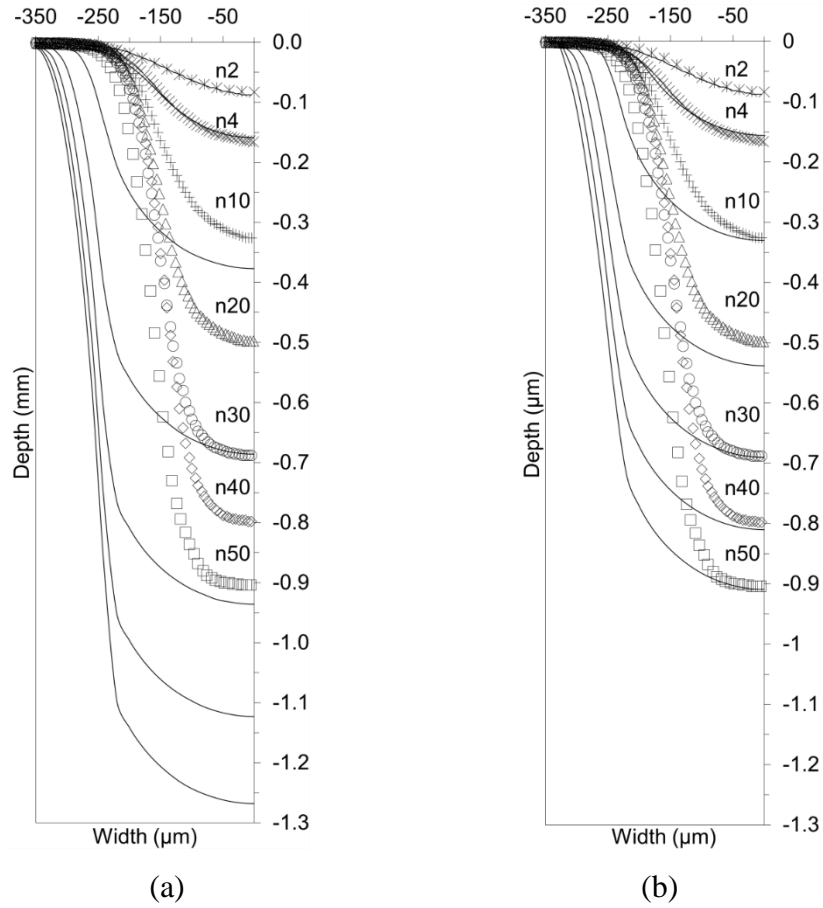
Figure 3-5 Experimental (symbols) and predicted (solid lines) micro-channel profiles using: (a) surface evolution model of Eq. (3.4) without depth correction ($E_{inst}=1$), and (b) using $E_{inst}=1.972/z^*(0,t)^{0.177}$. Data for submerged machining in SS 316L at $\Theta=90°$, $P_p=138$ MPa, $V_t=1000$ mm/min, $h=2$ mm, $n=2, 4, 10, 20, 30, 40, 50$ passes.

The particle flux $\phi(x)$, particle velocity $V(x)$, and velocity constant K in Eq. (3.5) under the AWJ conditions of the present tests were not easily determined. Therefore, following the approach of Getu et al. [57,121], the erosive efficacy function, $Q^*(x^*)$, of Eqs. (3.4) and (3.5) was inferred

by curve fitting a measured shallow cross-sectional profile to a normal distribution with a standard deviation of $\sigma=0.055$ (Eq. (3.12)).

As expected, the model greatly over-predicted the centerline depth (Figure 3-4a; average error for all conditions was 29%), because it assumed an erosion rate that did not decrease with depth. Figure 3-5b shows the predicted results with the depth-varying instantaneous erosion rate, E_{inst}. Although the depths were now predicted accurately (with an average centerline depth error less than 4%), the widths were still vastly over-predicted after about 2 passes. The average percentage error in the predicted width at half the channel depth was 58% for $n \geq 4$ passes. This suggested that there was a change in the erosive efficacy dependence on x^* that was originally determined from the shape of a shallow channel cross-section. Specifically, the erosion pattern of the water jet became markedly narrower after about 2 passes, corresponding to a channel depth of approximately 200 µm.

3.3.4. Profile predictions using a depth-varying erosive efficacy function

The model predictions of Figure 3-5b imply a two-stage channel formation, where a relatively wide erosive efficacy characterizes the erosion pattern when channels are initially forming, and the sidewalls adjacent to the footprint are subject to the radial flow of the abrasive slurry as illustrated in Figure 3-6a. After the initial formation of the channels, a second stage of channel formation is hypothesized to occur wherein most of the slurry flow from the footprint is directed along the length of the channel rather than radially and up the sidewalls (Figure 3-6b). This would decrease the erosion of the sidewalls relative to the channel depth in the region of the footprint and make the effective erosive efficacy seen on further passes much narrower, approaching the jet diameter.
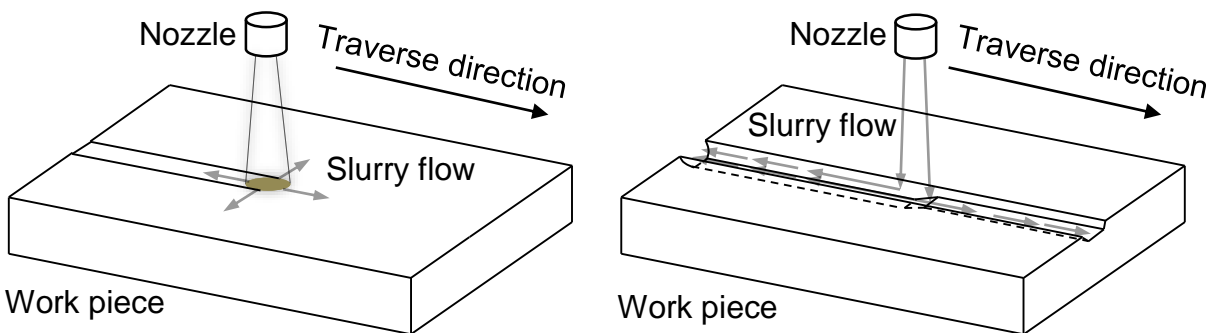
Figure 3-6 (a) The first stage ($n \leq 2$ passes), the channel is forming and a radial flow from the footprint erodes the channel wall as shown by the arrows. (b) The channel is sufficiently deep to direct most of the slurry goes along the length of the channel.

Figure 3-5 shows that, in the initial stages of machining, the shallow channel profiles could be fitted accurately by using a Gaussian function of the form

$$Q_{is}^*(x^*, 0, \sigma) = e^{-\frac{(x^*)^2}{2\sigma^2}}$$
(3.12)

where the subscript "is" refers to the initial stage of channel formation. This is consistent with Alberdi et al. [9] who reported that the water jet channels in aluminum had the bell shape or a normal distribution. As mentioned above, the parameter σ which represents the spread of the erosive efficacy, was found by fitting Eq. (3.12) to profiles of shallow channels in the two target materials made in water and in air at nozzle angle θ=90° and standoffs h=2 and 3 mm. This yielded σ= 0.055 and 0.04 at h=2 and 3 mm, respectively, independent of the target material and whether the machining was in air or submerged. Figure 3-7 shows that a normal distribution with a standard deviation, σ, of 0.055 at h=2 mm provided a good curve fit to the measured profile. However, the cross-sectional profile shape became much narrower after 2 passes (Figure 3-6), and the channel width approached that of the free jet, d_j.
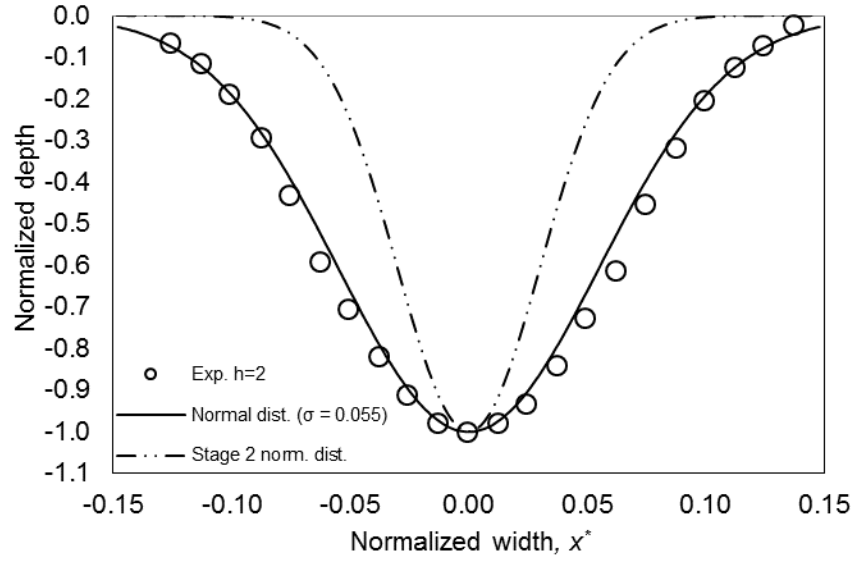
Figure 3-7 Normalized measured (Exp.) two-pass profile of AWJM channels machined at standoff h=2 mm, and curve fit of Eq. (3.12), using σ=0.055. Dashed curve is best-fit of Eq. (3.12) to deeper channel profiles ($n>2$).

As explained by Haghbin et al. [123], the AWJ diameter, d_j, increased linearly with standoff distance, h, due to spreading as

$$d_j = C.h_{eff} + D \tag{3.13}$$

where h_{eff} is effective standoff distance (i.e. the sum of the nominal standoff distance and the channel centerline depth), and the parameters C and D are specific to the water jet orifice and operating conditions, and were measured to be 50.55 and 350.9, respectively, for submerged machining, and 120.7 and 214.3, respectively, for machining in air. The narrower erosive efficacy in the second stage ($n>2$) was modelled by making the width of the erosion pattern a function of the channel depth. This was done by choosing σ in Eq. (3.12) to correspond to a distribution where the erosive efficacy was 1% of its centerline value at an x^* corresponding to the jet diameter (Eq.

(3.13)) at a given effective standoff length, h_{eff}. This yielded an erosive efficacy that changed with channel depth according to:

$$Q^*(x^*, 0, \sigma) = -\exp\left(\frac{-(x^*)^2}{2\left[\left(\frac{C}{6069.71}|z^*(x,t)|\right) + \left(\frac{\left(C + D/h\right)}{6069.71}\right)\right]^2}\right)$$
(3.14)

where h is standoff distance in mm. Equation (3.14) was then used in Eqs. (3.7) and (3.4) to predict the profiles of micro-channels machined using 4-50 passes for submerged and unsubmerged machining at h=2 and 3 mm.

3.3.5. Predicted surface evolution for AWJM at Θ=90° in water and in air using new model

Equation 3.4 was numerically solved using the modifications introduced in Section 3.3. with the initial condition $z^*(x^*,0)$=0, using the method of lines implemented in Mathcad 14 (Mathsoft Engineering & Education, Inc., Cambridge, MA, USA) to obtain the predicted multi-pass normalized micro-channel profiles. The non-dimensional time step was Δt^*= 500 and 1000 while the non-dimensional coordinate step was Δx^*=500 and 1000 for $n\leq2$ passes and $n>2$ passes, respectively.

Figure 3-8 and Figure 3-9 compare the predicted profiles using the new two-stage model with measured profiles for submerged and unsubmerged machining in stainless steel 316L and aluminum 6061-T6 at , at standoff distances h= 2 and 3 mm, respectively. Although the two-stage model is more accurate than the single-stage model of Figure 3-5, the differences in the predicted and measured channel width remained larger than the differences in the predicted depth. The average percentage difference in the channel width at half depth was 10% for all the data of Figure 3-8 and Figure 3-9. The difference between the predicted and measured width varied randomly with depth due to process fluctuations, such as variations of water pressure and abrasive mass flow rate, which lead to change of AWJ diameter. It is noted that a few of the model cross-sections contained some waviness near the bottom (e.g. the model profiles for 40 and 50 passes in Figure 3-8b). These were artifacts of the numerical solution procedure that can be eliminated by

increasing either the smoothing term, ε, or the non-dimensional time step, Δt^*, and coordinate step, Δx^*.
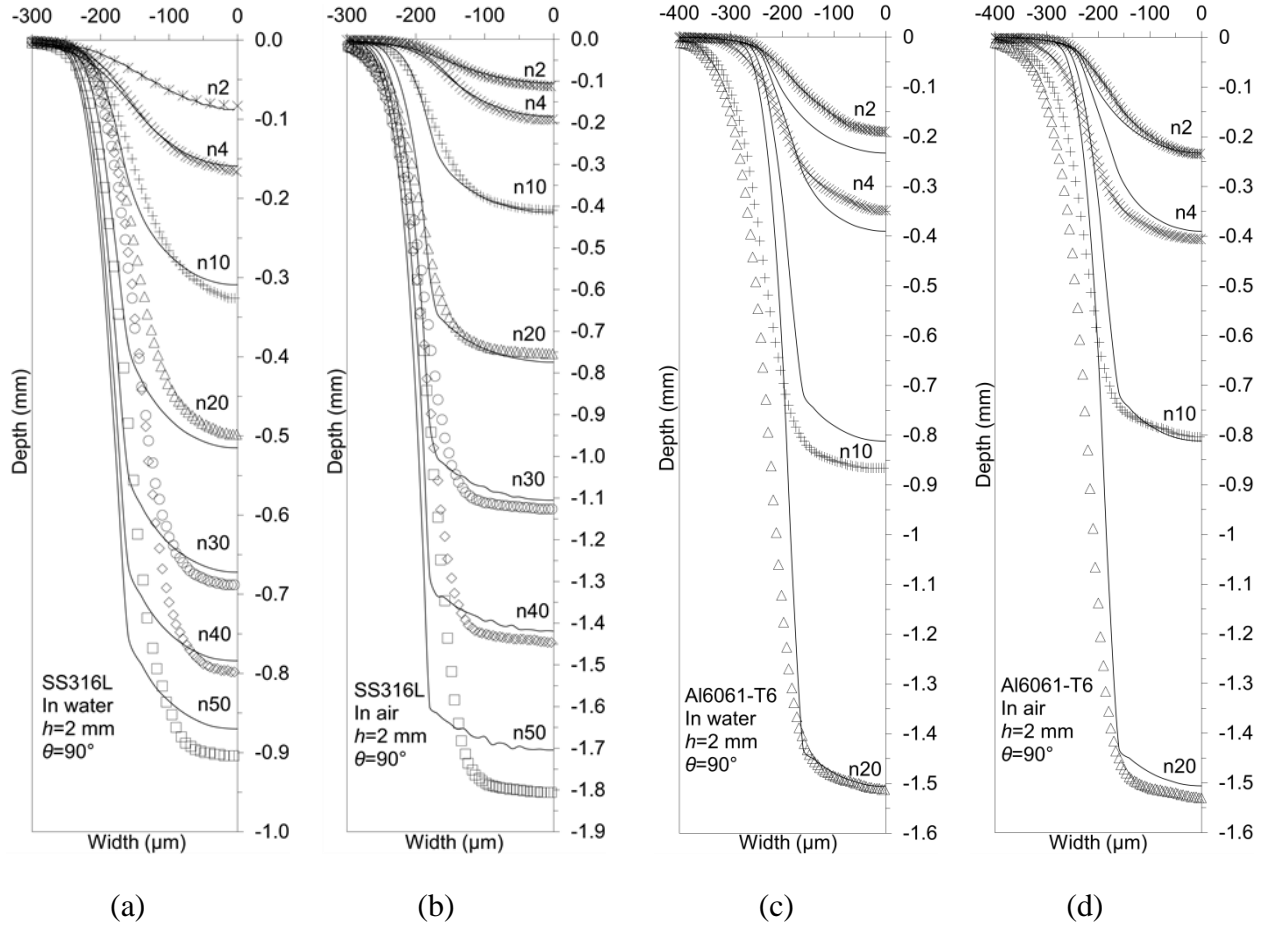
Figure 3-8 Measured (symbols) and predicted (solid lines) micro-channel profiles for standoff distance h=2 mm and nozzle angle θ=90° using model of Eq. (3.4) with E_{inst} (Eq. (3.6)) and a two-stage erosion efficacy. SS316L (n=2, 4, 10, 20, 30, 40, 50): (a) submerged, (b) in air. Al6061-T6 (n=2, 4, 10, 20): (c) submerged, (d) in air. P_p=138 MPa, V_t=1000 mm/min.
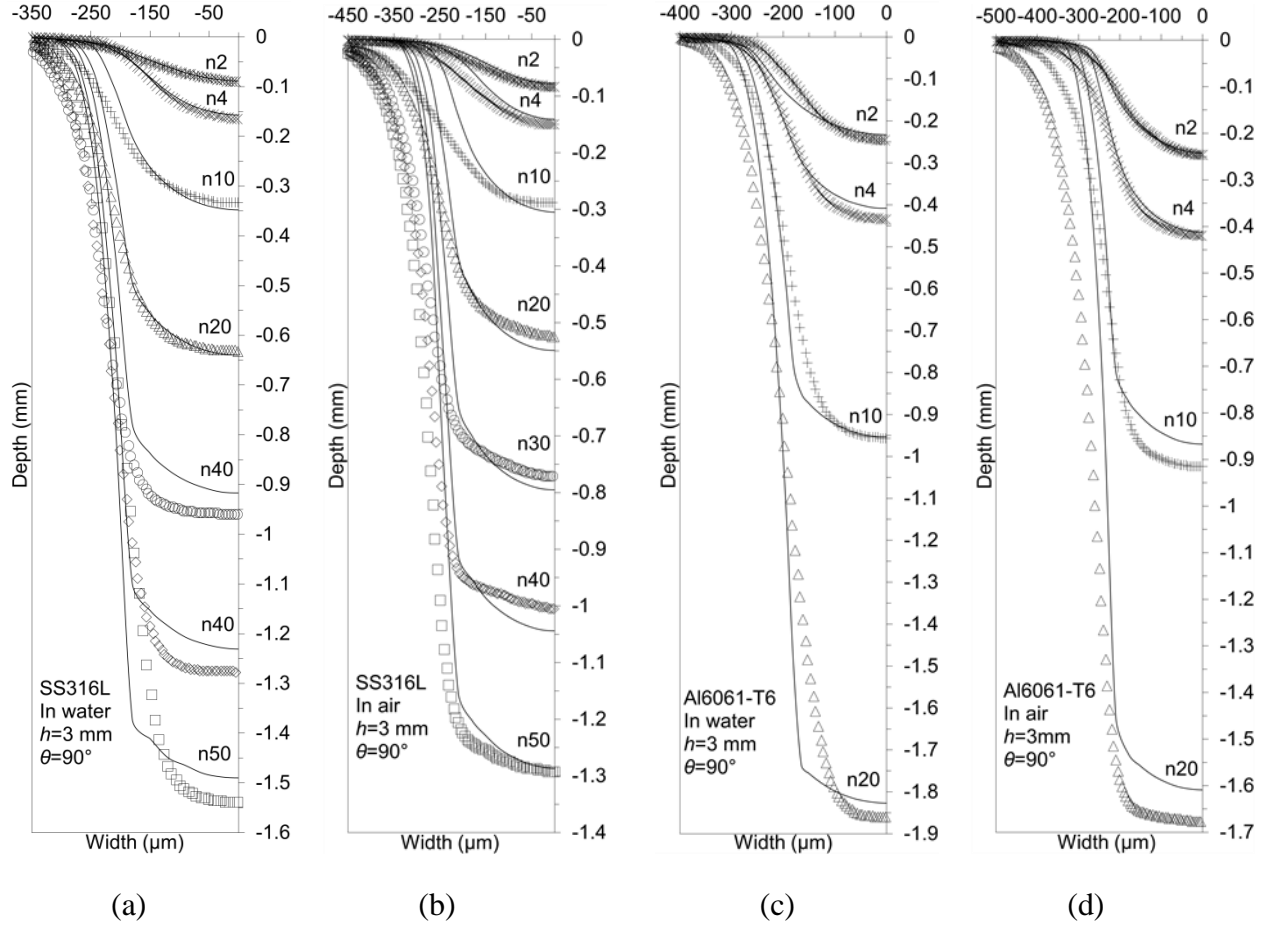
Figure 3-9 Measured (symbols) and predicted (solid lines) micro-channel profiles for standoff distance h=3 mm and nozzle angle θ=90° using model of Eq. (3.4) with E_{inst} (Eq. (3.6)) and a two-stage erosion efficacy. SS316L (n=2, 4, 10, 20, 30, 40, 50): (a) submerged, (b) in air. Al6061-T6 (n=2, 4, 10, 20): (c) submerged, (d) in air. P_p=138 MPa, V_t=1000 mm/min.

3.3.6. Predicted surface evolution for AWJM at Θ=30° in water and in air using new model

As shown in Figure 3-4, the erosion rate of both target materials was maximum between 20° and 35°. The predicted and measured profiles for micro-channels machined at θ=30° using both backward (BW) and forward (FW) machining in SS316L and Al6061-T6 are shown in Figure 3-10 and Figure 3-11, respectively. For in-air and submerged machining at h=3mm, the standard deviation of 0.035 (Eq. (3.12)) was used for the first stage, and Eq. (3.14) was used to make the width of the erosive distribution a function of depth in the second stage of forming channels.

Figure 3-10 and Figure 3-11 show that the overall accuracy of the model in predicting the shape of the channels at a jet angle of 30° was similar to that at θ=90° (Figure 3-8 and Figure 3-9); i.e. the error in the predicted width at half depth was 16%, while it was 10 % at θ=90°. The maximum error in the prediction of the sidewall slopes was 3% for both nozzle angles. There was no significant difference in the prediction error between forward and backward machining.

| | | | |
| (a) | (b) | (c) | (d) |
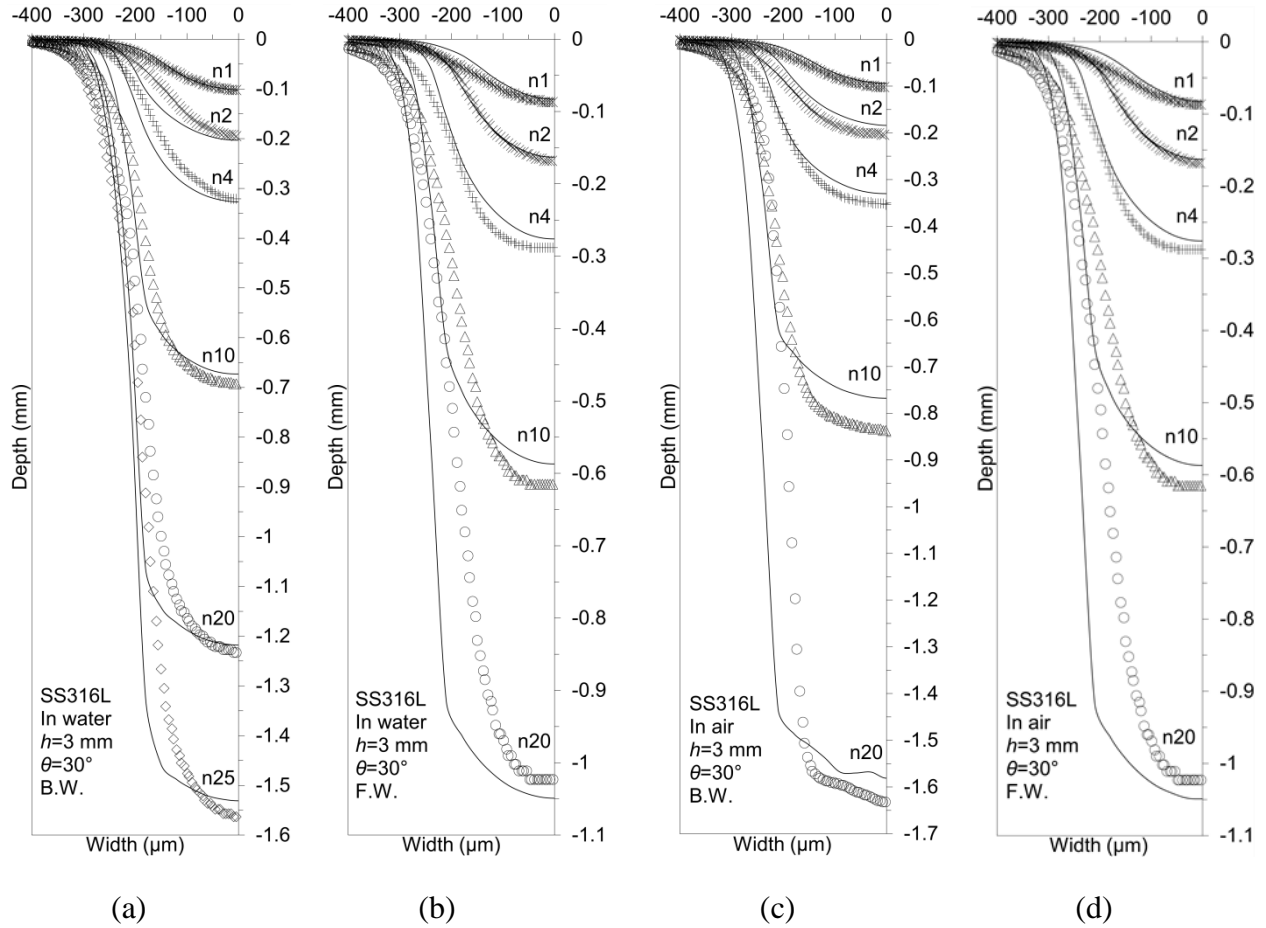
Figure 3-10 Experimental (symbols) and predicted (solid lines) micro-channel profiles machined in SS316L (n=2, 4, 10, 20) at standoff distance h=3 mm and nozzle angle θ=30°, using surface evolution model of Eq. (3.4) with E_{inst} (Eq. (3.6)) and the two-stage erosion efficacy with σ=0.035 (Eq. (3.12)) for the first stage and Eq. (3.14) for the second stage. (a) backward (B.W.) submerged, (b) forward (F.W.) submerged, (c) backward (B.W.) in air, (d) forward (F.W.) in air. P_p= 138 MPa, V_t=1000 mm/min.
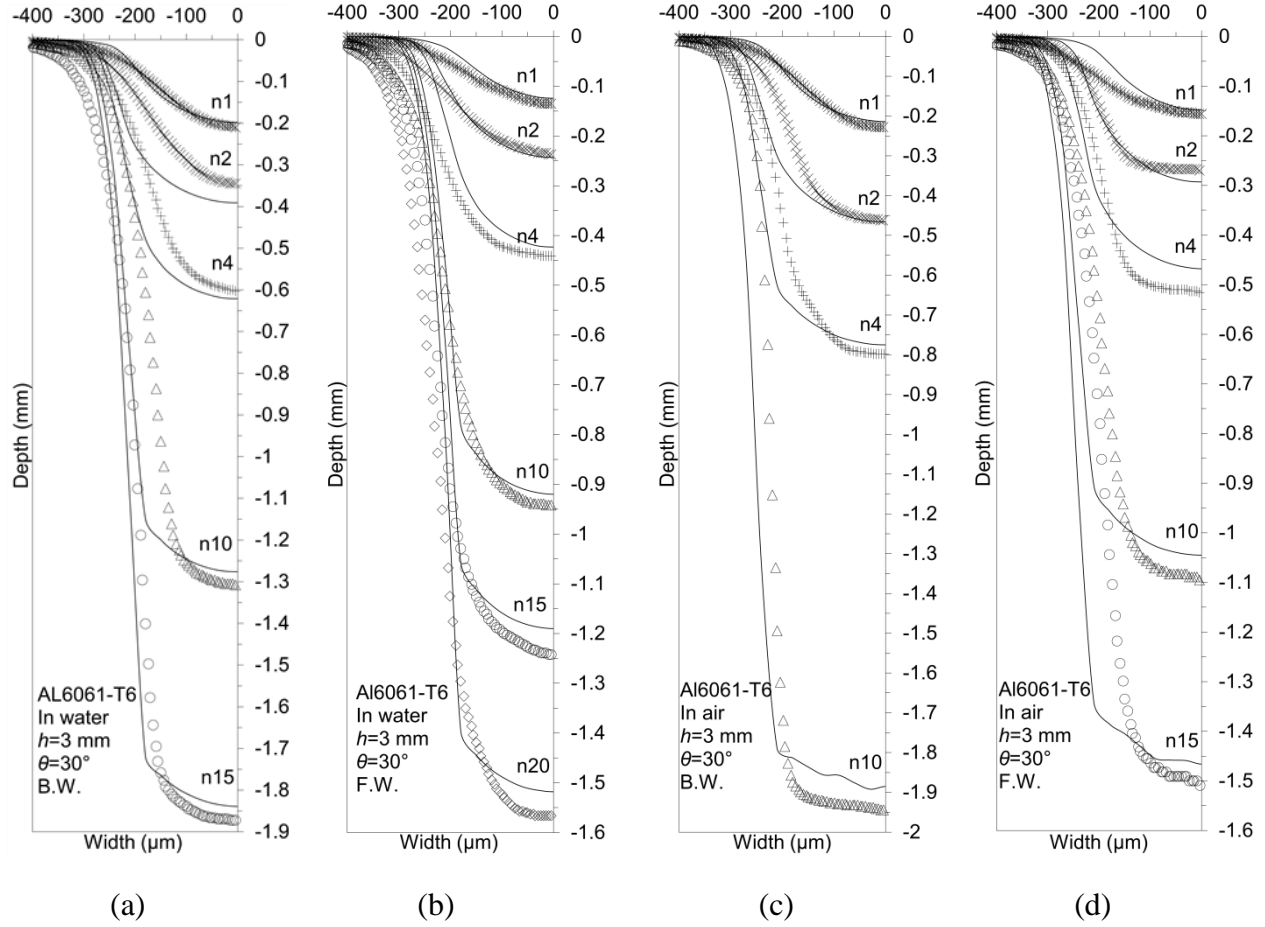
Figure 3-11 Experimental (symbols) and predicted (solid lines) micro-channel profiles machined in Al6061-T6 (n=2, 4, 10, 20) at standoff distance h=3 mm and nozzle angle θ=30°, using surface evolution model of Eq. (3.5) with E_{inst} (Eq. (3.6)) and the two-stage erosion efficacy with σ=0.035 (Eq. (3.12)) for the first stage and Eq. (3.14) or the second stage. (a) backward (B.W) submerged, (b) forward (F.W.) submerged, (c) backward (B.W.) in air, (d) forward (F.W.) in air. P_p= 138 MPa, V_t=1000 mm/min.

The main source of the remaining error in the prediction of the channel cross-sectional shapes was attributed to the inability of the present model to account for the secondary milling caused by the jet flow as it deflected from the bottom of relatively deep channels. Such secondary milling of the sidewalls was not captured by the profiles of shallow calibration channels, as explained in Haghbin et al. [123]. Computational fluid dynamic (CFD) modelling could be used to better understand and predict the erosion produced by these additional complex flows.

56

3.3.7. Summary of methodology to predict surface evolution in high aspect-ratio channels

The instantaneous erosion efficacy, $Q_{inst}^*(x^*)$, in Eq. (3.7) and the normalized erosion rate (Figure 3-4) at different incident angles, $g(\alpha)$, used in the model are typical of a system consisting of the target material, abrasive particles, pressure, micro-nozzle, and the fluid surrounding the jet (i.e. submerged or unsubmerged machining). In this section, a procedure is described which can be used to calibrate the model for different systems. The present water-jet micro-machining model incorporated two modifications that were necessary to capture the effects of the water flow on the erosion:

(i) The centerline erosion rate was modelled as a function of channel depth to account for its decrease with the growing stagnation zone [123].

(ii) The width of the erosion pattern was modelled in two-stage stages, because channel shape in the very early phase of machining from a flat surface was significantly broader than in a second phase where the abrasive flow was constrained by the channel walls, thereby making the erosive pattern narrower. Moreover, in the second stage, channels became progressively wider with increasing depth, and this was modelled by broadening the distribution of the erosive flux to match the growing width of the spreading water-jet at the effective nozzle standoff distance to the bottom of the channel.

The implementation of this surface evolution model (Eq. (3.4)) requires the following data:

1. The variation of the normalized instantaneous centerline erosion rate, E_{inst}, with channel depth can be obtained by measuring the depths of two channels spanning the range of the shallowest and deepest desired channels. The error incurred in using only these two data points (i.e. the deepest and shallowest channels) compared to using all the data from Haghbin et al. [123] was found to be only about 7% for metals (Al6061-T6 and SS316L). This is an acceptable error given the large decrease in experimental effort associated with using just these two measurement conditions. This dependence of E_{inst} on channel depth is only a function of channel geometry (independent of the type of metal, jet angle, standoff distance, jet submerged or in air, forward or backward machining), and is therefore expected to be the same for a wide range of ductile materials that result in U-shaped channels. Moreover, another master curve for V-shaped channels, such as those that develop in brittle materials such as glass, has also been provided [123].

2. The diameter of the water jet can be estimated as a function of standoff distance by cutting slots through an easily-eroded material such as high-density polyurethane modeling foam [123]. This is used to determine the variation of the erosion efficacy distribution with channel depth using the method of Section 3.3.4.

3. The dependence of the erosion rate on the angle of attack ($g(\alpha)$) can be measured by machining shallow channels (about 50 µm deep) at various nozzle inclinations as discussed in Section 3.2.2. The effect of random fluctuations in the abrasive mass flow rate during water jet machining can be accounted for by periodically machining shallow calibration channels.

3.4.Summary

The present model to predict the cross-sectional profiles of relatively deep channels produced in metals by abrasive water jets was based on an earlier model developed for abrasive air-jet micro-machining [21,78]. The erosion patterns produced by water jets are quite different, and so it was necessary to incorporate three modifications into the model: (i) the decrease in erosion rate with increasing channel depth, (ii) the abrupt narrowing of the erosive pattern produced by the jet footprint once a channel was formed on a flat surface and the flow became constrained by the channel walls, and (iii) the progressive widening of the channels as they became deeper. The model was tested for stainless steel 316L and aluminum 6061-T6 at nozzle angles of 90° and 30°, with standoff distances of 2 and 3 mm. It was found to work equally well when the water jet was submerged and when it was used in air, and when machining was in the forward or backward directions. Channel depths were predicted to within approximately 4%, while the average error in the predicted channel width at half the depth was less than 16%, and the maximum error of the predicted sidewall slopes was less than 3%. Further refinements of the model will likely require CFD modelling of the complex flows within deeper channels in order to account for the relatively small amount of secondary milling of the sidewalls. As will be shown in the next chapter, AWJM can result in wavy channels due to fluctuations in abrasive mass flow rate. The next chapter describes a new high pressure slurry jet apparatus that solves this problem.

Chapter 4 High Pressure Abrasive Slurry Jet Micro-Machining using Slurry Entrainment

This chapter is based on the following published paper:

N. Haghbin, F. Ahmadzadeh, J. K. Spelt, and M. Papini, "High pressure abrasive slurry jet micro-machining using slurry entrainment," *International Journal of Advanced Manufacturing Technology*, pp. 1-13, 2015.

4.1. Introduction

Abrasive slurry jets (ASJ) have been used for micro-machining in recent years, because they have advantages over traditional micro-fabrication technologies including the absence of a heat-affected zone and a low workpiece force transfer, which result in little change in target material properties. A promising application of ASJ technology is the milling of micro-channels for use in micro-fluidic devices [125] and micro-electro-mechanical systems (MEMS) [126].

In abrasive slurry jet micro-machining (ASJM) systems, a slurry of abrasive particles and water is premixed and pumped through a small orifice to form a jet that erodes a target material. Most previously developed ASJM setups operate at relatively low pressures (<14 MPa). Investigators such as Nguyen et al. [127] have identified such ASJM devices as promising for the micro-machining of high-quality features in brittle materials such as glass. For example, Wang et al. [48] drilled holes in glass using a 3 MPa slurry jet and found that the cross-sections of these holes were W-shaped. Pang et al. [91] used an ASJM system with a pressure range of 8-14 MPa to machine channels in glass, finding that the channel width increased with increasing pressure and standoff distance. Moreover, they reported an increase in channel depth with increasing pressure and dose of particles (decreasing traverse velocity), but standoff distance did not have a significant effect on channel depth. Nouraei et al. [128] used a 4 MPa ASJM system to micro-machine holes and 350-500 μm wide U-shaped micro-channels having a very low waviness. They reported a glass erosion rate of 0.6 mg/g. Later, Kowsari et al. [129] used the same setup with a dilute polymer solution to machine V-shaped micro-channels and micro-holes with a width less than 250 μm in glass. They found that the polymer solution allowed for machining symmetric through-holes in a 3-mm-thick glass plate without chipping around the exit edge.

There have been relatively few attempts at developing high-pressure abrasive slurry jet micro-machining (HASJM) systems. For example, Hashish [130] developed a 345 MPa HASJM set-up with a slurry that had a concentration of garnet particles of up to 48 wt% in order to mill Al6061-T6. Liu [131] fabricated an HASJM apparatus with a similar working concept and similar pressure range, and found that it was a viable technology for producing concave and convex surfaces such as optical lenses, with a relatively low roughness and waviness in both ductile and brittle materials. Miller [4] developed a 70 MPa HASJM system using 20 wt% slurries of either aluminum oxide (Al_2O_3) or garnet, and demonstrated very high resolution cutting of metals, polymer, composites and glass. However, the conventional HASJM systems discussed above forced the high-pressure slurry through critical components, resulting in premature damage to the slurry valve [4], and very high wear in nozzles and valves [130].

The present work was aimed at avoiding these problems by introducing a system in which the slurry was entrained after the high-pressure water passed through an orifice into a mixing chamber. The water pump pressure, P_p (i.e. the water pressure measured at the exit of the water pump) was between 135 and 250 MPa. The system was essentially a modified abrasive water jet micro-machining setup fitted with a prototype micro-nozzle and a pre-mixed slurry tank. The system was used to machine micro-channels over a wide range of aspect ratios (depth/width), and the system process parameters such as pressure, traverse velocity, standoff distance, and slurry flow rate were optimized for micro-machining purposes. A preliminary investigation by Haghbin et al. [132] showed that this HASJM system produced channels with centreline roughness (R_a=1.35 µm) and waviness (W_a=1.93 µm) that were, respectively, 19% and 44% smaller than those produced with conventional abrasive water jet micro-machining (AWJM). This was attributed to a more consistent abrasive flow rate and the elimination of air bubbles in the erosive jet.

4.2. Experiments

4.2.1. Experimental setup

Figure 4-1 shows a schematic of the high-pressure slurry jet setup. A water-based slurry with either 3 wt% or 6 wt% 25 μm aluminum oxide was premixed in two separate 19 L graduated containers a main slurry tank and a reservoir tank mounted H_1=28 cm higher and connected to the main tank with a 6.35 mm tube. Once the slurry level in the main tank decreased by more than 0.5

L, the valve installed on the connecting tube between reservoir tank and the main tank was opened in order to keep the slurry level in the main tank approximately constant (Figure 4-1a). This ensured an approximately constant slurry mass flow rate to the nozzle; i.e. there was at most a measured 1.2% variation in slurry flow rate. Both slurry tanks were continuously stirred using 102 mm diameter propellers at 180 rpm. The ratio of propeller to mixing tank diameter and the mixer rotational speed were chosen to prevent particle settlement, as calculated by Nouraei et al. [128]. The slurry flowed under the pressure head H_2=79 cm from the main tank through a 3.2 mm inner diameter tube into the mixing chamber of an OMAX 2626 Jet Machining Center (OMAX Corp., Kent, WA, USA) capable of water pump pressures, P_p, of up to 345 MPa. As shown in Figure 4-1b, the slurry flow rate was adjusted using a 1/8" abrasive slurry valve. The OMAX system was fitted with a prototype nozzle having orifice and mixing tube diameters of 127 µm and 254 µm, respectively.

The OMAX system utilized a dump valve (Figure 4-1a) to control the water flow rate, $\dot{m}_w$. The water pressure immediately upstream of the nozzle orifice, P_w, was calculated using Bernoulli's equation by collecting and weighing the flow rate of water, $\dot{m}_w$, exiting from the nozzle during the machining process (Section 4.3.1). It was found that P_w was much less than water pump pressure, P_p. The nozzle movement was computer controlled with a positioning accuracy of ±76 µm over 30 cm and a maximum traverse velocity of 4572 mm/min.

In Figure 4-1, The inlet slurry flow rate, $\dot{m}_s$, and thus the particle concentration (wt%) of the slurry exiting the nozzle (i.e. $W_{t,out} = (W_{t,in}\,\dot{m}_s)/(\dot{m}_s + \dot{m}_w)$) was controlled using the abrasive slurry valve (ASV, Figure 4-1b) and was measured in each experiment as the difference in the weight of the main tank before and after 60 s of flow. The 25 µm aluminum oxide particle concentration in the inlet slurry, $W_{t,in}$, was either 3 wt% or 6 wt%. The jet flow rate exiting the nozzle (i.e. $\dot{m}_j = \dot{m}_w + \dot{m}_s$) was measured in a similar fashion, using slurry collected in a small container at the nozzle exit. The nozzle high-pressure water flow rate ($\dot{m}_w$ in Figure 4-1) was found as $\dot{m}_w = \dot{m}_j - \dot{m}_s$.

Mixer

Valve

Connecting tube

Mixer

Reservoir tank

Main tank

Dump valve

$\dot{m}_p - \dot{m}_w$

Slurry valve

High-pressure water

Slurry tube

$\dot{m}_p, P_p$

$\dot{m}_w, P_w$

Nozzle

Water pool

H_1

H_2

$\dot{m}_s$

$W_{t,in}$

Support structure

(a)

Nozzle orifice

Mixing chamber

Mixing tube

Water
$\dot{m}_w, P_w$

Inlet slurry
($\dot{m}_s$, $W_{t,in}$)

Abrasive slurry valve (ASV)

Slurry tube

h: Nozzle standoff distance

Jet containing mixture of abrasive, water without air
$\dot{m}_j = \dot{m}_s + \dot{m}_w$, $W_{t,out}$

Workpiece

(b)

Figure 4-1 (a) Schematic of high-pressure slurry jet setup, and (b) AWJM nozzle. Not to scale.

4.2.2. Micro-channel experiments

As explained in Section 4.1, the micro-fabrication of channels with a width less than 1 mm is useful in many industrial applications [133]. Using the parameters in Table 4.1, the influence of pressure, traverse velocity, standoff distance, slurry flow rate, and number of passes on the shape, erosion rate, depth, and width of micro-channels was investigated. Straight multi-pass micro-channels were milled into 15×5×0.3 cm thick Al6061-T6 and 10×5×0.3 cm thick borosilicate glass (Borofloat®, Schott Inc., NY, USA) samples using the HASJM setup. These materials were chosen to represent typical ductile (Al6061-T6) and brittle (glass) erosive systems used in MEMS and microfluidics applications.

Table 4.1. Operational parameters of the HASJM

Standoff distance (mm), h	1, 2, 5, 10
Abrasive type	Al_2O_3
Average abrasive diameter (µm)	25
Opening of abrasive slurry valve (%), ASV	25-40-50-100
Inlet slurry flow rate (g/min), $\dot{m}_s$	200-317
particle concentration of input slurry (%), $W_{t,in}$	3, 6
Water pump pressure (MPa), P_p	134-263
Traverse speed (mm/min), V_t	20, 40, 100, 500, 1000
Nozzle angle (deg.), Θ	30°, 45°, 90°
Number of passes, n	1, 2, 4, 10, 20, 30, 40, 50, 60
Orifice diameter/mixing tube diameters (µm), d_O/d_M	127/254
Workpiece material	Al6061-T6, glass

The micro-channels of various depths were machined into the two target materials using a stepped arrangement with adjacent sections receiving an increasing number of passes (n=4, 10, 20, 30, 40, 50, 60 passes) without turning off the slurry jet. The samples were clamped to a stationary base that was placed underneath the nozzle (Figure 4-1b) at different standoff distances, h, and the nozzle was moved at different traverse speeds. The resulting micro-channel profile shapes were measured using a non-contact optical profilometer (model ST 400, Nanovea, Irvine, CA, USA) having lateral and vertical resolutions of 0.1 µm.

A scanning electron microscope was used to further characterize the channels. All data points (i.e. depths, widths, erosion rates, roughness, and/or waviness) of channels were reported as the average and standard deviation of 18 total measurements; i.e. 6 measurements within a 1.5 cm long machined channel, repeated on three separately machined channels. It was found that channel-to-channel scatter was similar to scatter within a single channel.

4.2.3. Specific erosion rate

In order to compare the material removal under the different machining conditions (e.g. pressure, standoff distance, traverse velocity, abrasive mass flow rate, etc., the specific erosion rate was calculated as

$$E = \frac{M_m}{M_a} \tag{4.1}$$

where M_a was the total abrasive mass used to remove a mass M_m of target material.

4.2.4. Optimum slurry flow rate

It was found that for machining harder materials such as metals, the slurry flow rate had to be controlled to ensure a maximum transfer of momentum from the high-speed pure water jet exiting the orifice to the low speed slurry entering the mixing tube. To determine the optimum abrasive slurry flow rate, the momentum and energy exchange analysis developed by Zhang et al. [134] for abrasive water jet micro-machining, was modified for use with the HASJM system.

Applying conservation of momentum to the input and output flows of the nozzle (assembly consisting of the mixing chamber, mixing tube and high-pressure orifice. Figure 4-1b), the output velocity of the slurry jet at the nozzle tip (exit of mixing tube), V_j is

$$V_j = \frac{\dot{m}_s V_s + \dot{m}_w V_w}{(\dot{m}_s + \dot{m}_w)} \tag{4.2}$$

where $\dot{m}_s$ and $\dot{m}_w$ are the mass flow rates of the slurry and water entering the mixing chamber from the slurry tank and orifice, respectively, while V_s and V_w are the corresponding velocities entering the mixing chamber.

Neglecting the water velocity upstream of the orifice and pressure within the mixing chamber, the water velocity, V_w, on the mixing tube side of the orifice (i.e. the orifice exit) was found using Bernoulli's law as

$$V_w = \eta \sqrt{\frac{2P_w}{\rho_w}} \qquad (4.3)$$

where P_w and ρ_w are the pressure and density of the high-pressure water upstream of the orifice. The orifice efficiency, η, which was 0.65, characterizes energy losses due to wall friction, water flow disturbances, and the compressibility of the water [29].

The power of the slurry phase of the jet exiting the nozzle, $E_{out,s}$ is

$$E_{out,s} = \frac{1}{2} \dot{m}_s V_j^2 \qquad (4.4)$$

By substituting Eq. (4.2) into Eq. (4.4), and ignoring the contribution of the slow moving slurry entering the mixing chamber ($\dot{m}_s V_s$), the kinetic energy out of the nozzle is

$$E_{out,s} = \frac{1}{2} \dot{m}_s \left(\frac{\dot{m}_w V_w}{\dot{m}_s + \dot{m}_w} \right)^2 \qquad (4.5)$$

Taking the derivative of Eq. (4.5) with respect to $\dot{m}_s$ and setting it to zero leads to the following condition for the maximum $E_{out,s}$

$$\dot{m}_s = \dot{m}_w \qquad (4.6)$$

Eq. (4.6) demonstrates that the slurry output power is optimal when the input slurry mass flow rate equals the high-pressure water mass flow rate through the orifice. The mass flow rate of the high-pressure water, $\dot{m}_w$, either can be measured directly or estimated using the continuity equation:

$$\dot{m}_w = \rho_w A_O V_w \qquad (4.7)$$

where A_O is the cross section area in vena contracta zone downstream of the orifice where the area is minimum and V_w is the water velocity in the vena contracta. Substituting Eq. (4.3) into Eq. (4.7)

$$P_w = \frac{8\dot{m}_w^2}{\rho_w \eta^2 \pi^2 d_o^4} \qquad (4.8)$$

where d_o is the jet diameter in vena contracta. The value of d_o was approximated as the orifice diameter (i.e. d_o=125 µm). It is noted that in reality only a portion of the momentum of the high-pressure water is actually transferred to the slurry; i.e. $V_j < \frac{\dot{m}_s V_s + \dot{m}_w V_w}{(\dot{m}_s + \dot{m}_w)}$ in Eq. (4.2) due to friction and particle fracture, so $\dot{m}_s < \dot{m}_w$. This will be discussed further in Section 4.3.3.

4.3. Results and discussion

4.3.1. Measurement of water and slurry flow rate

Figure 4-2 shows the measured dependence of $\dot{m}_s$ and $W_{t,out}$ on the percentage that the slurry valve stem was opened at P_p=235 MPa. The values of $\dot{m}_s$ and $W_{t,out}$ decreased from 291 g/min and 3.3 wt% to 200 g/min and 2.2 wt%, respectively, when the valve stem was closed to about 25% of its rotations to the fully open state. As expected, the output particle concentration was significantly lower than that entering (6 wt%) due to the mixing of the inlet slurry with the water exiting the orifice.
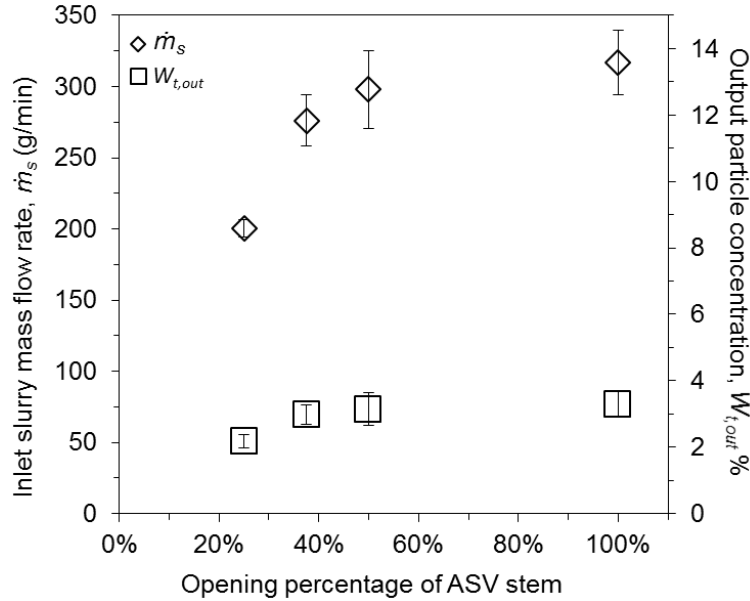
Figure 4-2 Variation of input slurry flow rate, $\dot{m}_s$, and output particle concentration, $W_{t,out}$, of the jet exiting the nozzle with percentage of the abrasive slurry valve (ASV) stem turns to fully open. P_p=235 MPa and inlet particle concentration, $W_{t,in}$, of 6 wt%. Scatter bars represent ±1 standard deviation of three separate measurements.

The globe valve used to regulate $\dot{m}_s$ was found to perform better than a needle valve, which tended to clog due to the accumulation of particles. There was a plateau in $\dot{m}_s$ to the nozzle at approximately 50% opening, which did not occur when the slurry tube was disconnected from the nozzle; i.e. the flow could be regulated beyond 50% when the tube was disconnected. Therefore, the plateaus in Figure 4-2 cannot be explained by the non-linear behavior of the globe valve alone. The most likely reason is flooding of the small annular space between the walls of the mixing tube and jet exiting the orifice. In other words, at ASV=50% ($\dot{m}_s$~300 g/min), the maximum slurry flow rate that could be entrained in the mixing tube was reached. As will be shown in Section 4.3.3, the flooding resulted in a sharp drop in the erosion rate.

Figure 4-3a shows the variation of the inlet slurry flow rate, $\dot{m}_s$, and output particle concentration, $W_{t,out}$, when the stem of the abrasive slurry valve was completely opened and partially opened (25%) at different water pump pressures, P_p (Figure 4-1), for inlet particle concentrations of $W_{t,in}$ of 3 wt% and 6 wt%. It is seen that the inlet slurry flow rate, $\dot{m}_s$, increased (e.g. from 130 to 200 g/min at ASV=25%) as the pump pressure increased from 138 MPa to 235 MPa, because a greater vacuum was formed in the mixing chamber as the water velocity increased [65]. Moreover, the sensitivity to the ASV position also increased with P_p. For example, at P_p=138 MPa, the closing the ASV stem to 25% of fully open caused an 11% reduction in the inlet slurry flow rate (reduced from 146 to 130 g/min), but at P_p=235 MPa it reduced the inlet slurry flow rate by 37% (reduced from 310 to 200 g/min). Moreover, Figure 4-3a shows that the nozzle outlet particle concentration, $W_{t,out}$, also increased (e.g. from 2.4%wt to 2.8%wt at ASV=25%) with increasing water pump pressure, because the increase in inlet slurry flow rate, $\dot{m}_s$, (i.e. 54%) with pressure was greater than that of the water flow rate, $\dot{m}_w$ (i.e. 28% increase, Figure 4-3a).

As expected, Figure 4-3b shows that the nozzle high-pressure water flow rate, $\dot{m}_w$, (199 g/min at P_p=138 MPa) and the water pressure just upstream of the orifice, P_w, (43 MPa at P_p=138 MPa) also increased as the water pump pressure, P_p, increased to 235 MPa. Moreover, further investigation showed that neither the inlet particle concentration, $W_{t,in}$, nor the inlet slurry flow rate, $\dot{m}_s$, had any significant effect on the high-pressure water flow rate, $\dot{m}_w$, passing through the orifice into the mixing chamber.
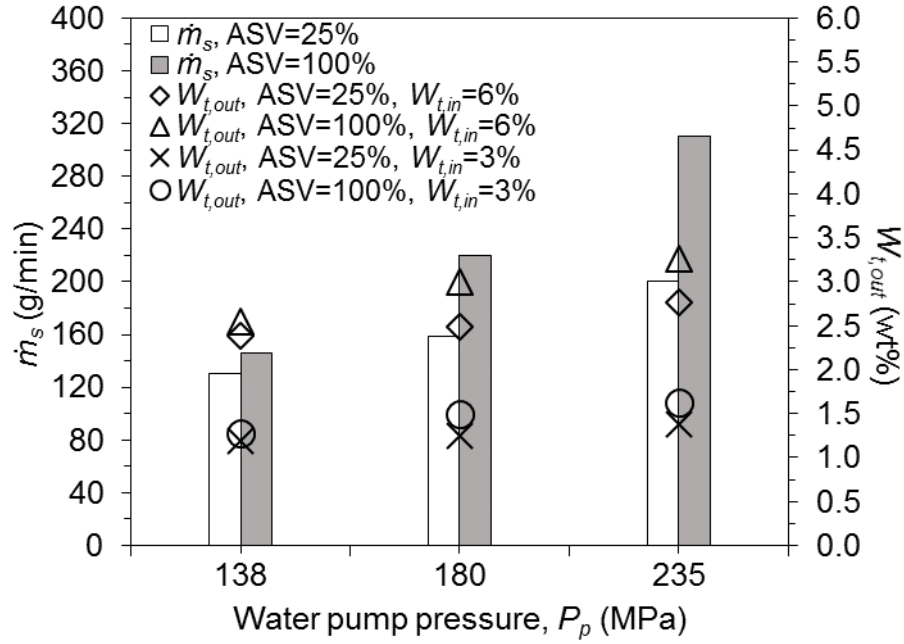
(a)
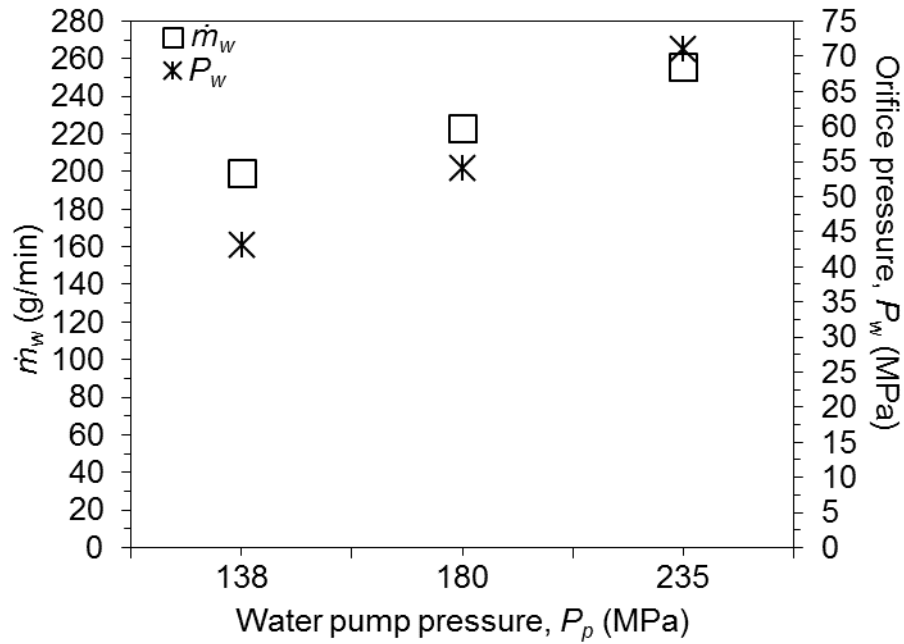
(b)

Figure 4-3 Effect of water pump pressure, P_p, on (a) inlet slurry flow rate, $\dot{m}_s$ and output particle concentration, $W_{t,out}$ and (b) high-pressure water flow rate passing through nozzle orifice, $\dot{m}_w$ and pressure just upstream of the orifice, P_w. Scatter bars representing ±1 standard deviation of 3 separate experiments were small enough to fit within the symbols.

4.3.2. Slurry jet size

Figure 4-4a shows a high-pressure slurry jet in air at a water pump pressure of P_p=235 MPa. The effective diameter of the slurry jet, d_j, was determined (Figure 4-4b) by measuring the
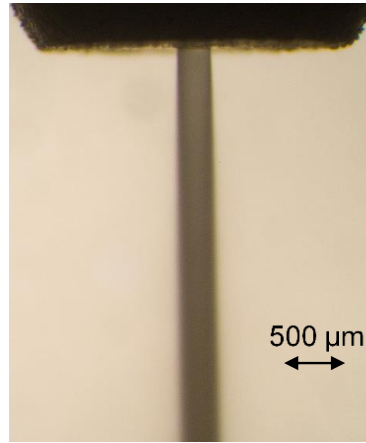
(a)
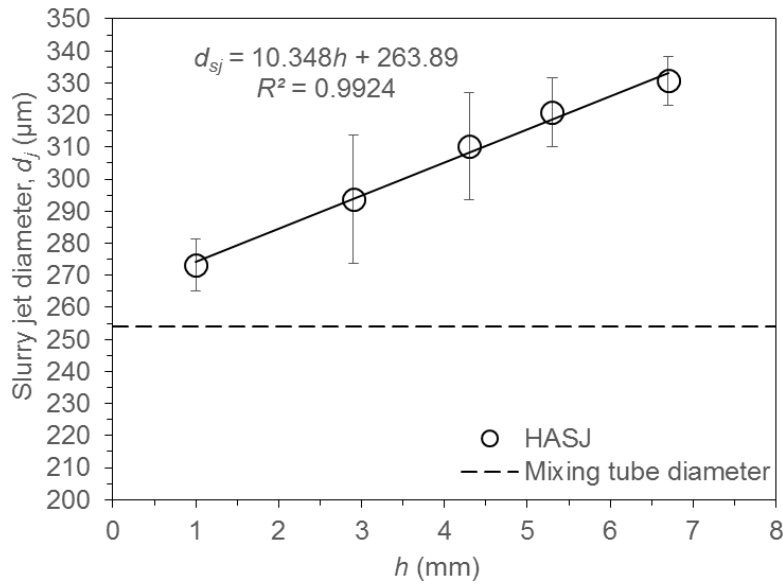
(b)

Figure 4-4 (a) High-pressure abrasive slurry jet emerging from the micro-nozzle in air. (b) Effective slurry jet diameter, d_j, from Renshape™ cutting tests at P_p=235 MPa, V_t=4572 mm/min with 25 μm Al_3O_2 at $W_{t,in}$=3 wt% and $\dot{m}_s$=317 g/min. Scatter bars indicate ±1 standard deviation of a total of 18 measurements on 3 separate slots.

width of slots cut through a high-density 3 mm thick foam board (Renshape, Huntsman Advanced Materials) with a traverse velocity of V_t=1000 mm/min as explained in detail in Haghbin et al. [123]. As Figure 4-4b shows, the jet diameter, d_j, tended towards the mixing tube diameter at low standoff distances (d_j=273 µm at h=1 mm), and increased linearly with increasing standoff (d_j=330 µm at h=6.5 mm). The jet divergence angle in the HASJM was 1.5°. In comparison, the divergence angle in low pressure ASJM was 0.03° using a 254 µm orifice [122], while in conventional AWJM using the present water jet machine and micro-nozzle it was 6.9° [123].

In AWJM, the abrasive-air mixture occupies more than 90 percent of the jet volume [35,36], which leads to greater divergence of the jet [39]. Moreover, the elimination of air entrainment in the mixing chamber of the HASJM greatly decreased the thickness of the water droplet zone typically found at the periphery of AWJM jets, thereby creating a jet with a sharper edge definition.

4.3.3. Optimum slurry flow rate

Figure 4-5 shows that both the specific erosion rate, E, and the centerline depth, d, of channels made in Al6061-T6 displayed a maximum (E=2.7 mg/g and d=159 µm) at $\dot{m}_s$=200 g/min (i.e. ASV=25%). These maxima are roughly consistent with Eq. (4.6) which predicted, under ideal conditions, that the power of the slurry is maximum when $\dot{m}_s = \dot{m}_w$. The measured water flow rate of $\dot{m}_w$=261.5 g/min was approximately 23% higher than predicted because of losses associated with friction and slip in the water, slurry, and mixing tube as discussed by Momber and Kovacevic [29]. There was also a sharp decrease in erosive power at 300 g/min (~ 50% ASV) corresponding to the flooding condition discussed in Section 4.3.1.

Since ASV=25% represented the maximum jet erosive power, it was used for most of the machining experiments on Al6061-T6. However, this ideal condition was found to be too aggressive for the brittle glass, which shattered upon exposure to the jet, even at a relatively low pressure of P_p=138 MPa. Therefore, the much less powerful condition ASV=100% was used for most of the machining experiments on glass.
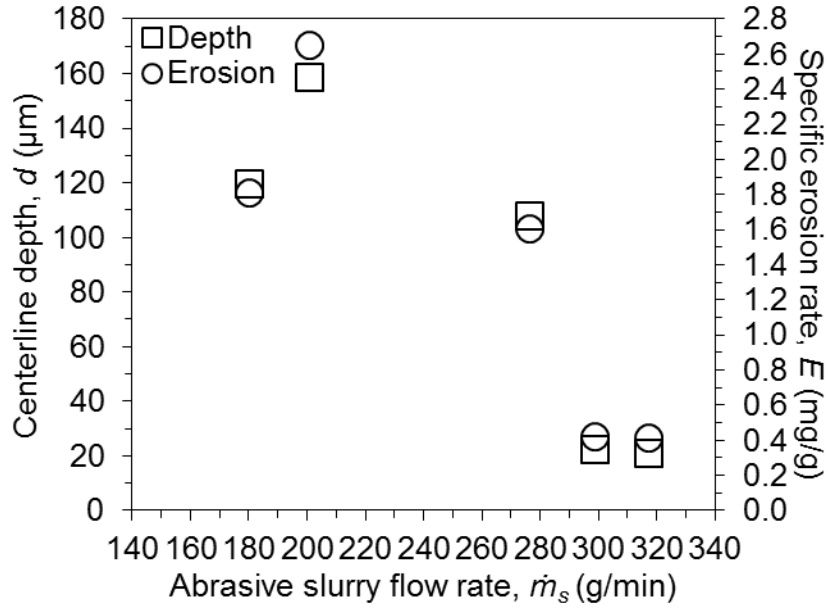
Figure 4-5 Effect of entrained slurry flow rate, $\dot{m}_s$, on specific erosion rate, E, and centerline depth, d, of channels made in Al6061-T6, at P_p=235 MPa, V_t=1000 mm/min, n=4 passes, W_t=6 wt%. Scatter bars representing ±1 standard deviation of a total of 18 measurements on 3 separate channels were small enough to fit within the symbols.

4.3.4. Effect of standoff distance

Figure 4-6 presents the normalized erosion rates (i.e. erosion rate at standoff distance h, E_h, divided by erosion rate at h=1 mm, E_1) of relatively shallow (d~28.7 µm in Al6061-T6 and d~50.5 µm in glass at h=1 mm) and deeper (d~174 µm in Al6061-T6 and d~221 µm in glass at h=1 mm) channels made in glass and Al6061-T6 at standoff distances between 1 and 10 mm under identical slurry jet conditions; i.e. multi-pass channels were machined on glass and Al6061-T6 samples placed side by side, and without turning off the jet. Figure 4-6 shows that as the standoff distance increased, the erosion rate increased in glass, but decreased in Al6061-T6.
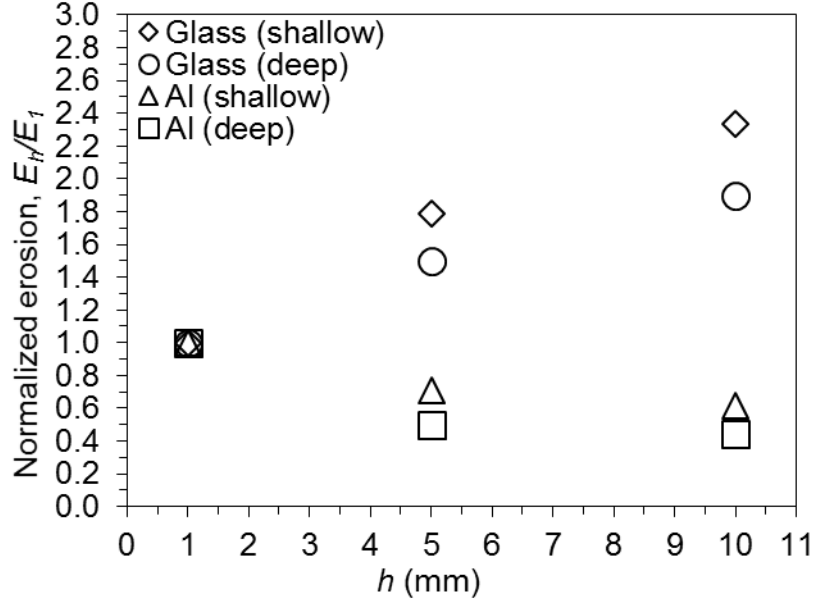
Figure 4-6 Normalized erosion rate ($\frac{E_h}{E_1}$) of relatively shallow ($d\sim28.7$ µm in Al6061-T6 and $d\sim50.5$ µm in glass at h=1 mm) and deeper ($d\sim174$ µm in Al6061-T6 and $d\sim221$ µm in glass at h=1 mm) channels as a function of standoff distance, h, made in (a) glass (E_1=0.10 mm³/g) and (b) Al6061-T6 (E_1=0.06 mm³/g) at identical non-stop HASJM conditions of P_p=134 MPa, V_t=1000 mm/min, $W_{t,in}$=3 wt%, ASV=100%, and nozzle angle of θ=90°. Scatter bars representing ±1 standard deviation of a total of 18 measurements on 3 separate channels were small enough to fit within the symbols.

The peculiar erosion rate behavior in Figure 4-6 can be better understood by comparing the measured channel depths and widths in glass and Al6061-T6 as shown in Figure 4-7. It is seen that, for both the shallow and deep channels, the centerline depths in glass increased slightly with standoff distance (Figure 4-7a), but they decreased sharply in Al6061-T6 (Figure 4-7b). The channel widths, however, drastically increased with increasing standoff distance in glass (Figure 4-7a), but to a much lesser extent in Al6061-T6 (Figure 4-7b). Channel-to-channel scatter in both depth and width were similar to scatter within a channel. The overall standard deviation among the centerline depths and widths were 1.6 µm and 13.1 µm, respectively, for glass, and 1.7 µm and 27.1 µm, respectively, for Al6061-T6. These general trends were found to be independent of slurry valve opening percentage (i.e. slurry flow rate) and jet inclination angle for both target materials.
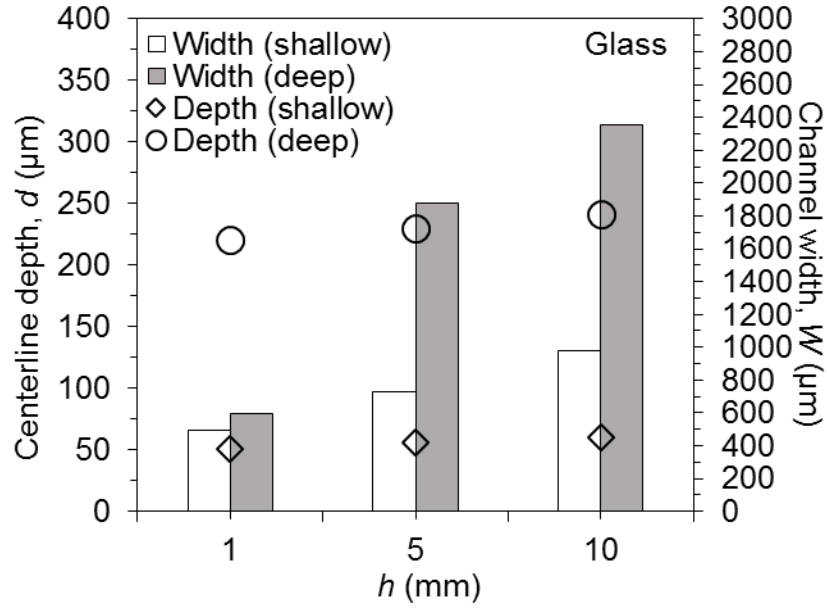
(a)
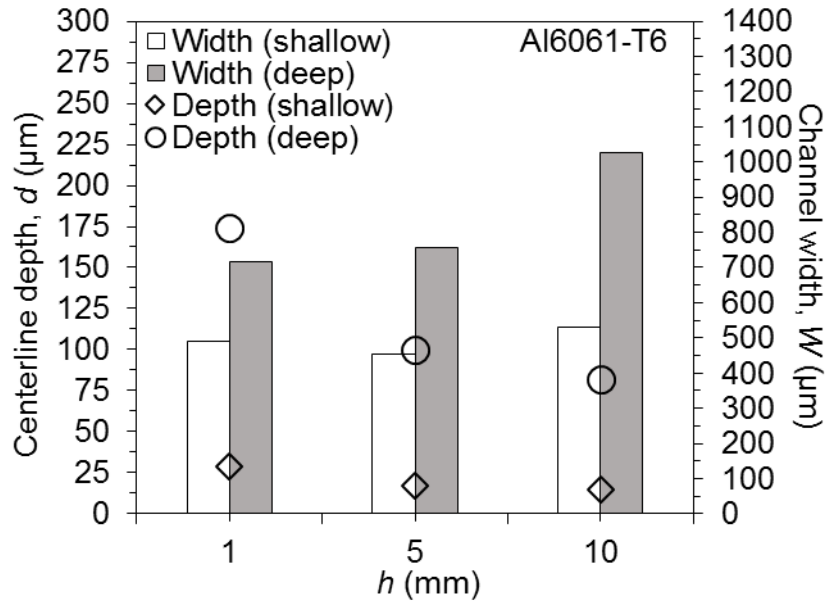
(b)

Figure 4-7 Centerline depth, d, and width, W, of relatively shallow (d~28.7 μm in Al6061-T6 and d~50.5 μm in glass at h=1 mm) and deeper (d~174 μm in Al6061-T6 and d~221 μm in glass at h=1 mm) channels as a function of standoff distance, h, made in (a) glass and (b) Al6061-T6 at identical non-stop HASJM conditions of P_p=134 MPa, V_t=1000 mm/min, $W_{t,in}$=3 wt%, ASV=100%, and nozzle angle of θ=90°. Scatter bars representing ±1 standard deviation of a total of 18 measurements on 3 separate channels were small enough to fit within the symbols.

The dependence of channel width and depth on standoff in this study did not agree with the results of Nouraei et al. [128], who found negligible changes in channel width or depth with standoff for a low-pressure abrasive slurry jet which had negligible divergence. The present results are more consistent with those obtained with abrasive water jet machining (AWJM) and abrasive air jet machining (AJM), where the erosive jets have greater divergence. For example, Hashish [5] and Haghbin et al. [123] showed that the channel width in metals increased with standoff distance, and Momber and Kovacevic [29] reported such increases for both ductile and brittle materials. Such trends are associated with jet spreading as standoff increases, since the target is exposed to an increasingly large jet footprint and a greater area for secondary milling due to the flow along the surface immediately after jet impact [135]. Although the increase and decrease in channel depth and erosion rate with standoff for brittle and ductile materials, respectively, appears never to have been reported under identical conditions, evidence for such behaviour exists in separate studies from the literature for AWJM and AJM. For example, Aich et al. [136] and Dadkhahipour et al. [135] found that the AWJM erosion and depth in glass increased with increasing standoff distance, and Fan et al. [137] showed a similar trend for the AJM erosion rate of glass. Dadkhahipour et al. [135] attributed this trend in AWJM to a decrease in particle interference at the lower particle fluxes associated with larger standoffs, as has also been shown for AJM by a number of studies; e.g. Ciampini et al. [138]. For more ductile materials such as metals, Kovacevic [94], Hashish [5], and Haghbin et al. [123] all found that AWJM depth of cut and erosion rate decreased with standoff. Such trends are usually associated with reduced jet energy at larger standoffs due to jet spreading.

The observations from the above studies can be used to explain the puzzling difference in the trend of centerline erosion rate (i.e. depth) with standoff that occurs for glass and Al6061-T6, as well as the trends of increasing channel width in Figure 4-7. As the jet spread with increasing standoff distance, particles at the periphery of the jet slowed down due to the drag of the surrounding air. However, these peripheral particles still had sufficient kinetic energy to erode the target surface, consistent with the increases in channel width for both materials. For example, the width of shallow and deep channels in glass increased from 496 µm to 976 µm and from 599 µm to 2351 µm in glass (Figure 4-7a) and from 491 µm to 529 µm and from 718 µm to 1026 µm in Al6061-T6, respectively (Figure 4-7b). The lower rate at which the width of channels in ductile materials increased with standoff distance (Figure 4-7b) compared to brittle materials (Figure

4-7a), was also observed by Momber and Kovacevic [29] for AWJM, and was simply due to the lower erosion rate of ductile materials (e.g. it was E_I=0.06 mm^3/g in Al6061-T6 and E_I=0.1 mm^3/g in glass under identical jet conditions as shown Figure 4-6). It is noted that peripheral particles at the leading and trailing edges of the moving footprint also contributed to channel centerline erosion. So this lower peripheral erosion in the ductile Al6061-T6 also explains the decrease in channel depth with standoff (d decreased from 29 µm to 15 µm for shallow channels and from 174 µm to 82 µm for deep channels, as seen in Figure 4-7b). However, in glass, even at the highest standoff, the peripheral particles still had enough energy to erode, resulting in relatively little change in depth. As mentioned previously, the slight increase in depth with standoff in glass (d increased from 50 µm to 60 µm for shallow channels and from 221 µm to 242 µm for deep channels, as seen in Figure 4-7a) was due to a decreased particle interference in glass that, as stated by Dadkhahipour et al. [135] for AWJM, tended to overcompensate for the loss in peripheral particle energy at higher standoffs.

4.3.5. Effect of pressure

Figure 4-8a, b shows that the specific erosion rate, depth and width of glass micro-channels (E=0.2 mg/g, d=8.8 µm, and W=312 µm at P_p=138 MPa) increased markedly with increasing water pump pressure, P_p (E=1.2 mg/g, d=118 µm, and W=573 µm at P_p=263 MPa). Similar trends were seen with Al6061-T6, i.e. increases in the range of E=0.7-2 mg/g, d=3-38 µm, and W=351-592 µm are seen in Figure 4-8a, c.

The increase in specific erosion rate and depth at higher pump pressure was attributed partly to the increase in particle concentration (i.e. $W_{t,out}$ increased by 27% over this range of P_p, Figure 4-3a), but mostly to the increased particle velocity. The width of the channels also increased at higher pressures due to greater secondary milling of the channel sidewalls by the higher kinetic energy of the slurry flow, and due to the small expansion of the slurry jet diameter with increasing pump pressure (i.e. d_j=279-309 µm at P_p=134-264 MPa, h=2 mm) caused by the corresponding increases in the water and slurry flow rates (Figure 4-3).
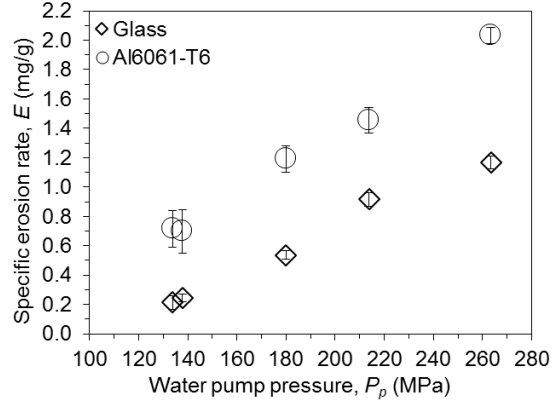
(a)
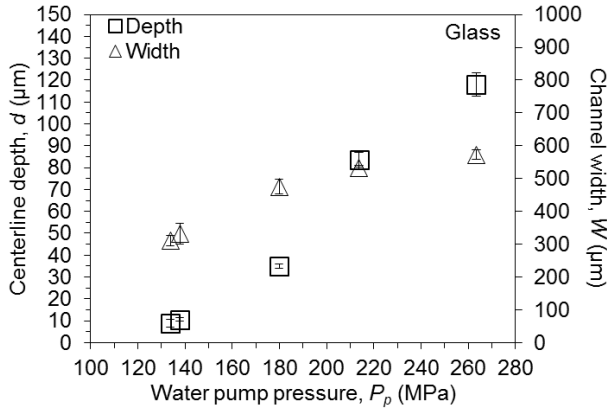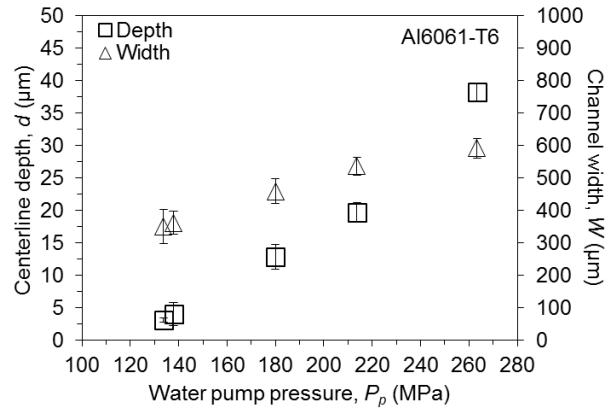
(b)   (c)

Figure 4-8 Effect of water pump pressure P_p on (a) specific erosion rate E in glass and Al6061-T6, and centerline depth, d, and width, W, of channels made in (b) glass at V_t=1000 mm/min, n=4 passes, ASV=100%, $W_{t,in}$=6 wt%, h=2 mm, and (c) Al6061-T6 at V_t=1000 mm/min, n=2 passes, ASV=40%, $W_{t,in}$=6 wt%, h=2 mm. Scatter bars represent ±1 standard deviation of a total of 18 measurements on 3 separate channels.

4.3.6. Effect of traverse velocity

4.3.6.1. Micro-machining of multi-pass channels

In controlled depth micro-milling, the aspect ratio (i.e. depth/width) and quality (i.e. waviness and roughness) of a micro-channel can be controlled using multiple passes at a relatively

high traverse velocity and/or a single pass at a low traverse velocity. It was therefore of interest to investigate the effects of traverse velocity and number of passes on the aspect ratio and quality of micro-channels produced using the present HASJM apparatus. Figure 4-9 shows the cross-sectional shapes of stepped multi-pass channels made in Al6061-T6 and glass using a high traverse velocity of V_t=1000 mm/min. Figure 4-9c and d show scanning electron micrographs of symmetric micro-channels made at V_t=1000 mm/min in Al6061-T6 and glass.

It is seen that the channel shape became asymmetric for aspect ratios greater than about 0.9 (i.e. depth/width). However, when a much lower traverse velocity (e.g. V_t=40 mm/min and less) was used to machine a channel with a single pass, no asymmetry resulted and channel quality was much better. For example, Figure 4-10 shows two typical micro-channels in aluminum (Figure 4-10a) at P_p=235 MPa and V_t=40 mm/min and glass (Figure 4-10b) at P_p=134 MPa and V_t=10 mm/min with aspect ratios (depth/width) greater than 1 using n=1 pass, h=2 mm. Figure 10c shows the average profiles of these two channels, illustrating that the eccentricity problem was solved when a low traverse velocity was used.

Moreover, it was observed that the centerline waviness, W_a, and roughness, R_a, of the channels made at a low traverse velocity (Figure 4-10) were much lower than those in the asymmetric channels made at a high traverse velocity (Figure 4-9). For example, the W_a and R_a (W_a=41 µm and R_a=4.2 µm at V_t=1000 mm/min) in Al6061-T6 (Figure 4-11a) decreased by about 95% and 71%, respectively, when the traverse velocity decreased from V_t=1000 mm/min to V_t=40 mm/min (W_a=2.6 µm and R_a=1.2 µm at V_t=40 mm/min). Thus, in order to both avoid asymmetry and low channel quality in the machining of high aspect-ratio channels, a relatively low traverse velocity using a single pass should be used rather than many passes at a high traverse velocity. Possible mechanisms for the asymmetry at high traverse velocities will be presented in the next section.

Finally, it was noted that the micro-channels made using HASJM were much less wavy and rough than those made using AWJM. For example, in multi-pass channels in Al60761-T6 with a depth of d= 250 µm made by both machining methods at V_t=1000 mm/min, the W_a and R_a in HASJM (W_a=6.9 µm and R_a=1.1 µm) were, respectively, 51% and 15% less than in AWJM (W_a=14.1 µm and R_a=1.3 µm). This is consistent with the previous study by Haghbin et al. [132].
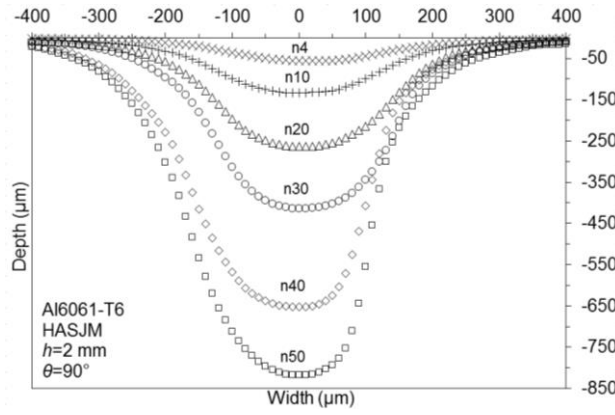
(a)
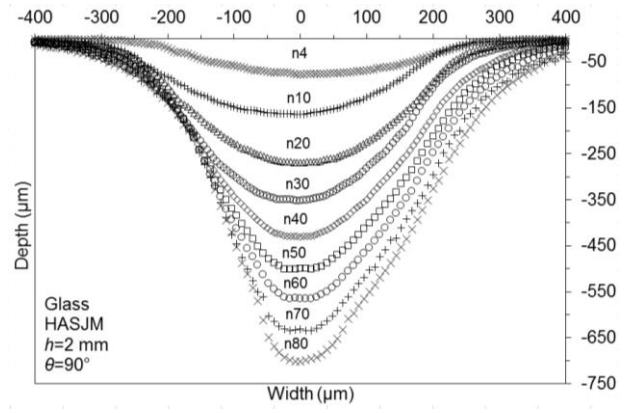
(b)
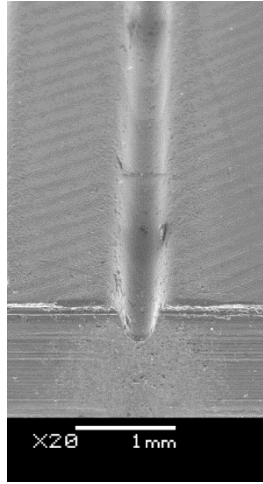
(c)
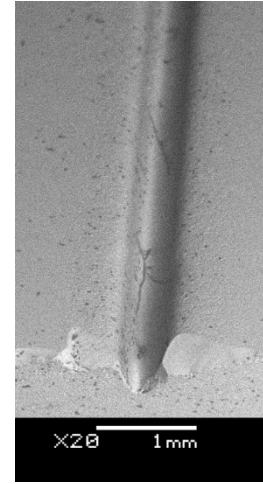
(d)

Figure 4-9 Cross-sectional profiles of multi-pass stepped channels made in (a) Al6061-T6 (n=4, 10, 20, 30, 40, 50 passes, P_p=235 MPa), (b) glass (n=4, 10, 20, 30, 40, 50, 60, 70, 80 passes, P_p=134 MPa) at high traverse velocity (V_t=1000 mm/min), h=2 mm, AVP=40 %, $W_{t,in}$=6 wt%, θ=90°, and scanning electron micrographs of (c) a 350 µm deep channel in Al6061-T6 using n=25 passes at P_p=235 MPa, V_t=1000 mm/min, (d) a 420 µm deep channel in glass using n=40 passes at P_p=134 MPa, V_t=1000 mm/min.

(a)   (b)

(c)
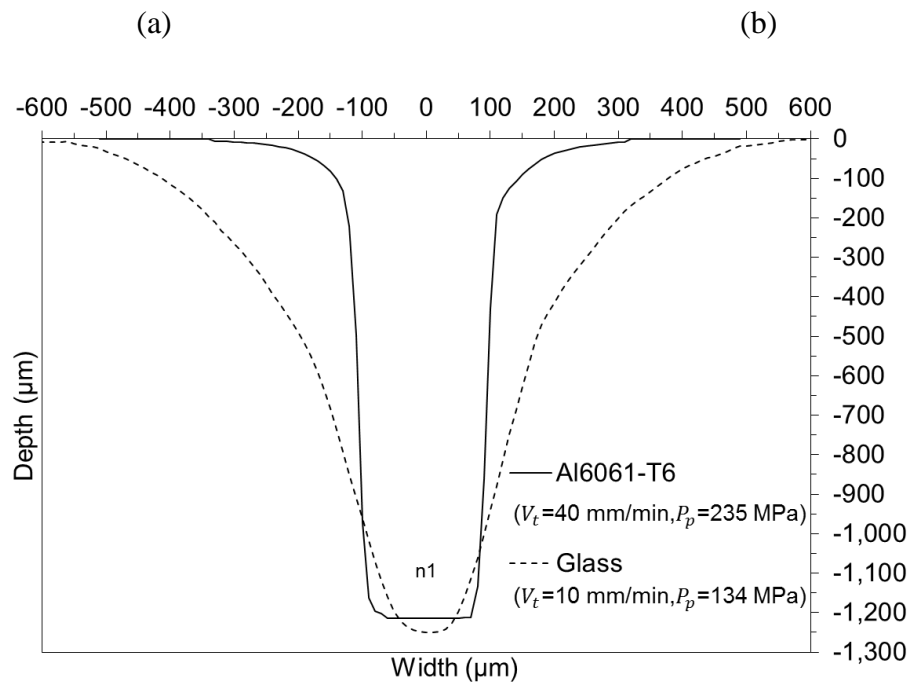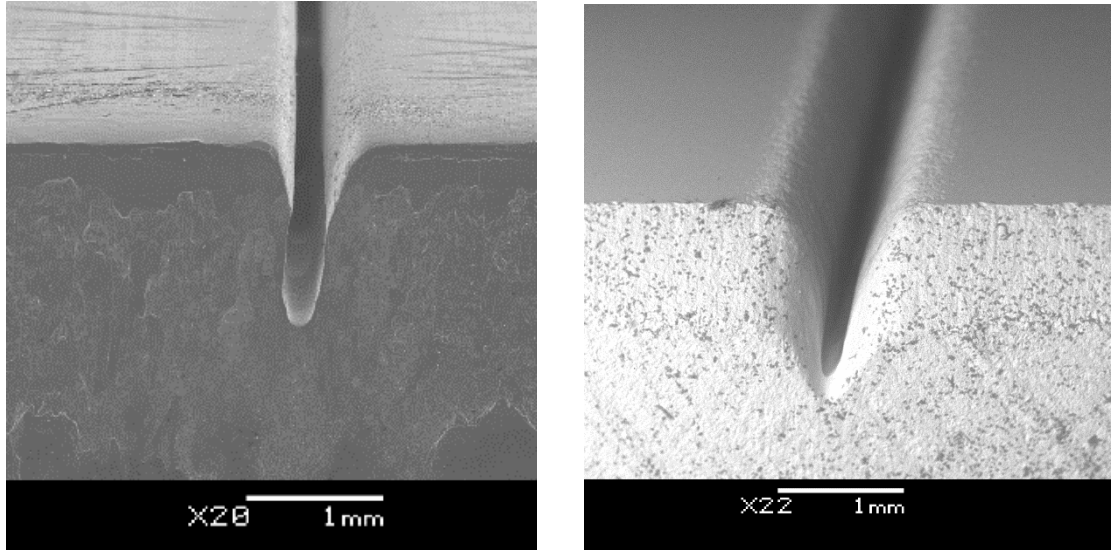
Figure 4-10 Scanning electron micrographs of micro-channels made at low traverse velocities in (a) Al6061-T6 at P_p=235 MPa, V_t=40 mm/min and (b) Glass at P_p=134 MPa, V_t=10 mm/min, n=1 pass, machined in air (unsubmerged) and h=2 mm, (c) average channel profiles of Al6061-T6 (a) and glass (b).
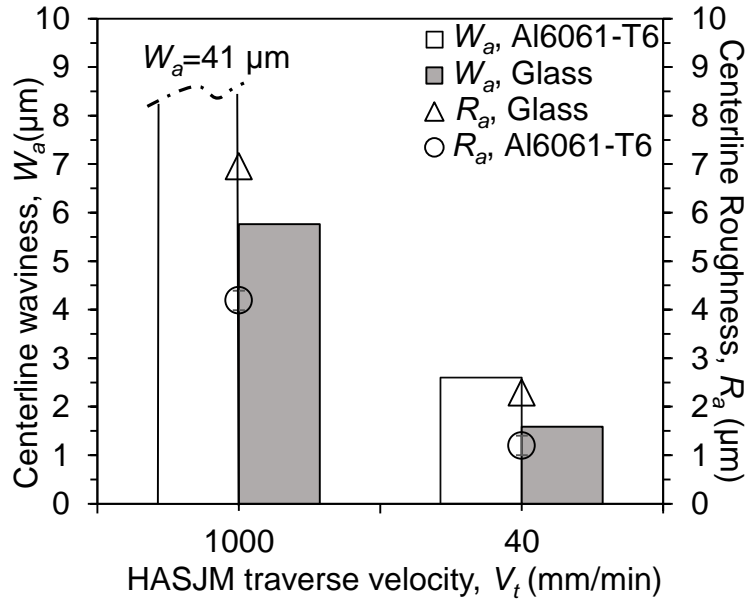
(a)
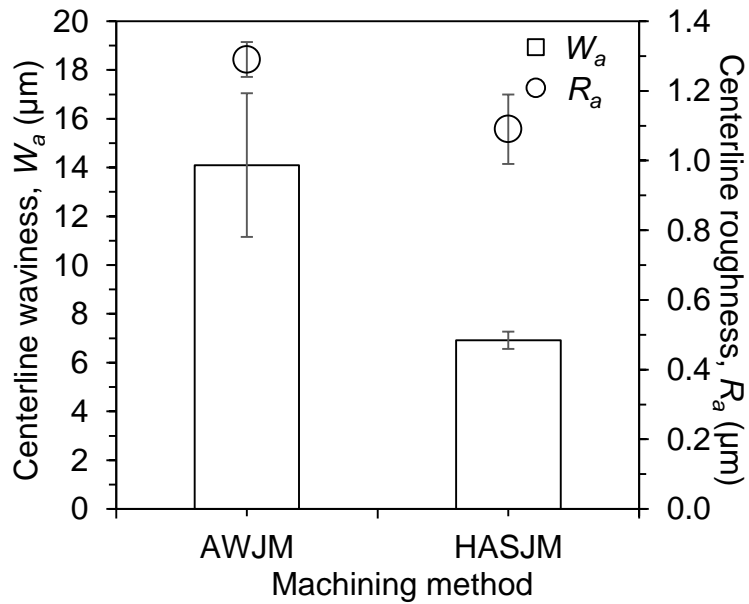
(b)

Figure 4-11 Centerline waviness, W_a, and roughness, R_a, of micro-channels in Al6061-T6 made by (a) using HASJM at high (V_t=1000 mm/min) and low (V_t=40 mm/min) traverse velocities, d=1.2 mm, (b) using both AWJM and HASJM at V_t=1000 mm/min, d=250 μm.

4.3.6.2. Mechanism of asymmetric channel formation

The mechanism responsible for the onset of channel asymmetry at high traverse velocities in relatively deep channels (beyond an aspect ratio of about 0.9) was unclear, and a number of possible explanations were examined experimentally as illustrated in Figure 4-12.
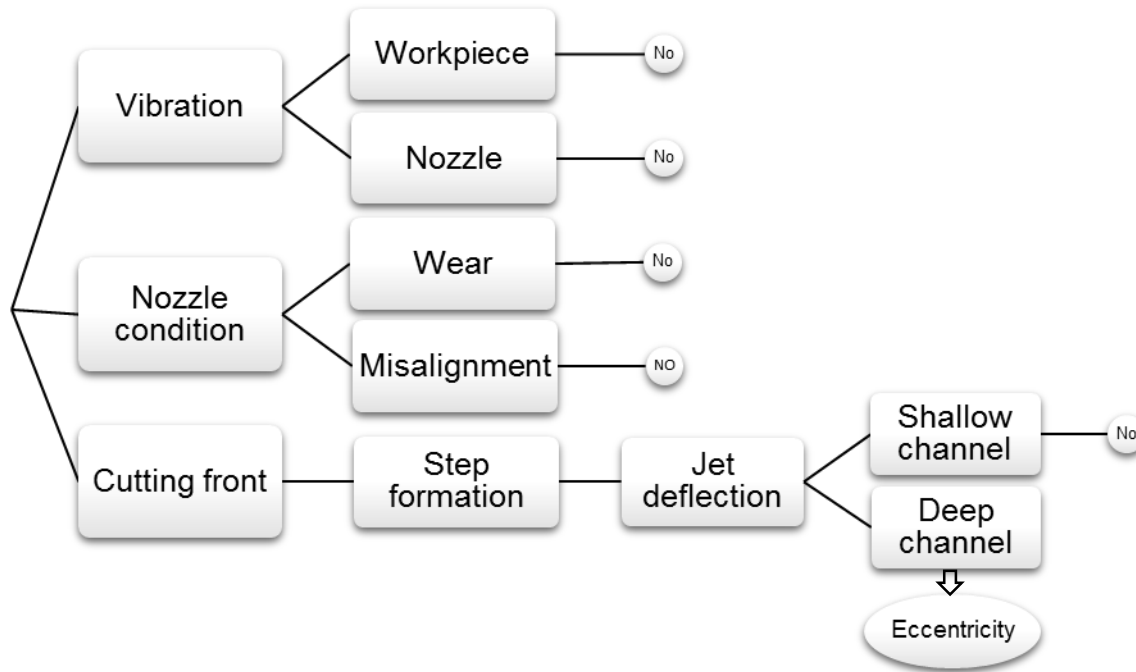
Figure 4-12 List of possible causes of asymmetry observed in deeper channels at high traverse velocities. Outcomes determined from experiments.

Vibration

Pang et al. [91] reported asymmetric channel waviness due to vibration of a slurry-jet nozzle. In the present experiments, workpiece vibration was minimized by clamping the target material as suggested by Monno and Ravasio [46]. The roughness and waviness of the left and right sidewalls was measured on channels that were milled using a range of traverse velocities, V_t, with different numbers of passes, *n,* such that the 1 mm thick Al6061-T6 sheets were completely cut through. Figure 4-13 shows that R_a and W_a, measured on the sidewalls half way through the sheet thickness

were the same on both sides of the channel at slow speed but became increasingly different as the speed increased.
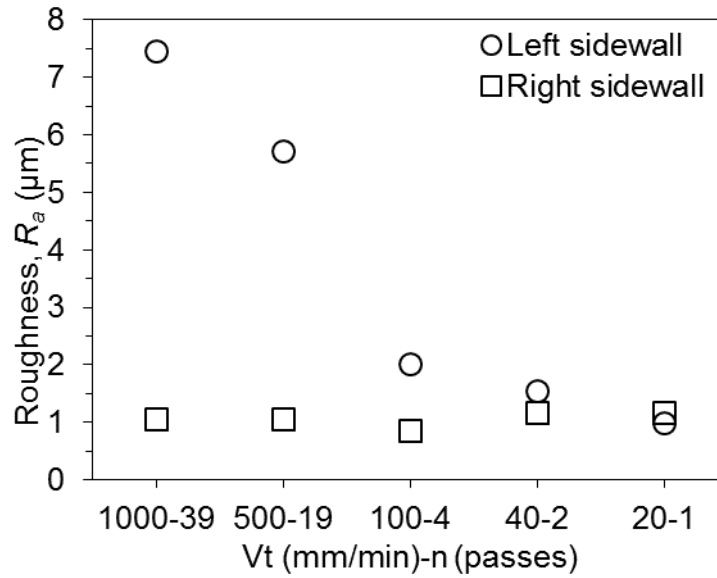
(a)
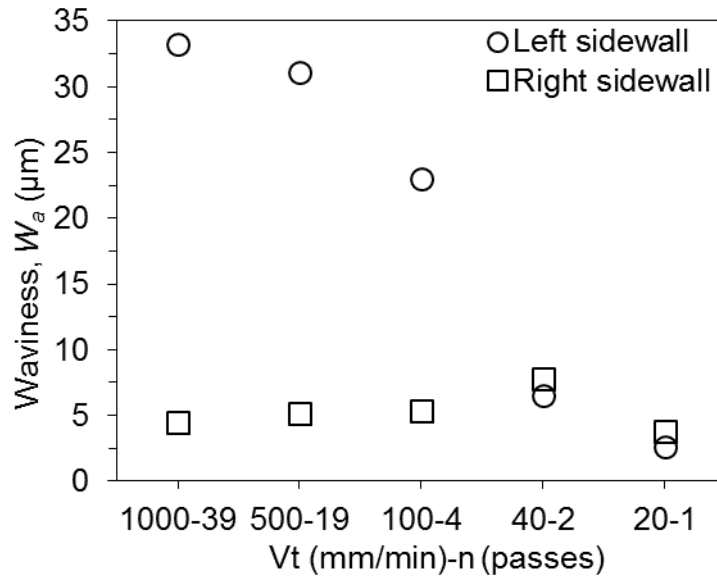
(b)

Figure 4-13 (a) Roughness and (b) waviness of left and right sidewalls of cut surfaces made with different combinations of traverse velocity (V_t) and number of passes (n), in 1 mm thick Al6061-T6 at P_p=235 MPa, h=2 mm. Scatter bars representing ±1 standard deviation were small enough to fit within the symbols.

A fast Fourier transform (FFT) analysis showed that there was no specific dominant frequency in the roughness and waviness data (Figure 4-13) on either sidewall, effectively ruling out workpiece vibration as a possible cause of the asymmetry.

Wear and misalignment of the nozzle

Two sets of channels were machined by scanning the nozzle at various inclinations in two perpendicular directions. It was found that the direction of asymmetry was random; i.e. separate channels made in a given direction were equally likely to tilt left or right. It was thus concluded that the asymmetry was not due to nozzle misalignment with the target. Moreover, channel asymmetry continued to be observed under the same conditions when a new nozzle was used.

Cutting front

A number of investigators have noted that the creation of a step in the cutting front (Figure 4-14) during machining using abrasive water jets at a high traverse velocity can deflect the jet laterally. For example, Hashish [140] used a high-speed camera to record steps in the cutting front of the cutting front formed by an AWJ. He explained that steps formed on the cutting front due to the existence of two different mechanisms of erosion, cutting and deformation wear, which led to the formation of two different front curvatures. Wang [139] and Pang et al. [91] described how the dissipation of slurry jet energy during the machining process caused the slurry flow to deflect from these steps to the channel sidewalls causing a jet instability. For abrasive waterjets, Guo et al. [142] also observed an unsteady oscillation of the jet to either one sidewall or both sidewalls due to such steps in the machining front. They found that this phenomenon led to grooves forming on the channel sidewalls made in different materials such as aluminum alloy, titanium alloy, steel, and ceramics. Orbanic and Junkar [141] explained the lateral waterjet deflection from these machining steps by using a "meandering river" analogy. As explained below, these four papers together provide the keys elements for the most likely explanation for the asymmetric channels observed in the present work at high traverse velocities.

At the high traverse velocity, a step formed on the cutting front as shown in Figure 4-14a,

because there were two erosion mechanisms; i.e. deformation erosion created the upper part of the front and cutting erosion created the lower part of the cutting front . If the jet deflecting from this step shifted laterally, it had the potential to widen the channel. For relatively shallow channels (i.e. aspect ratio ≤0.9), the deflected jet did not erode the sidewalls, but tended to escape from the channel and move along the unmachined flat surface. But for deeper channels at high traverse velocity, the deflected jet did erode the side walls because the flow was confined by the channel. In contrast to the previous AWJM cutting studies described above that noted jet deflection oscillating from side to side, the present milling process involved a secondary flow that could not escape at the bottom, but was instead trapped within the channel.

(a)   (b)
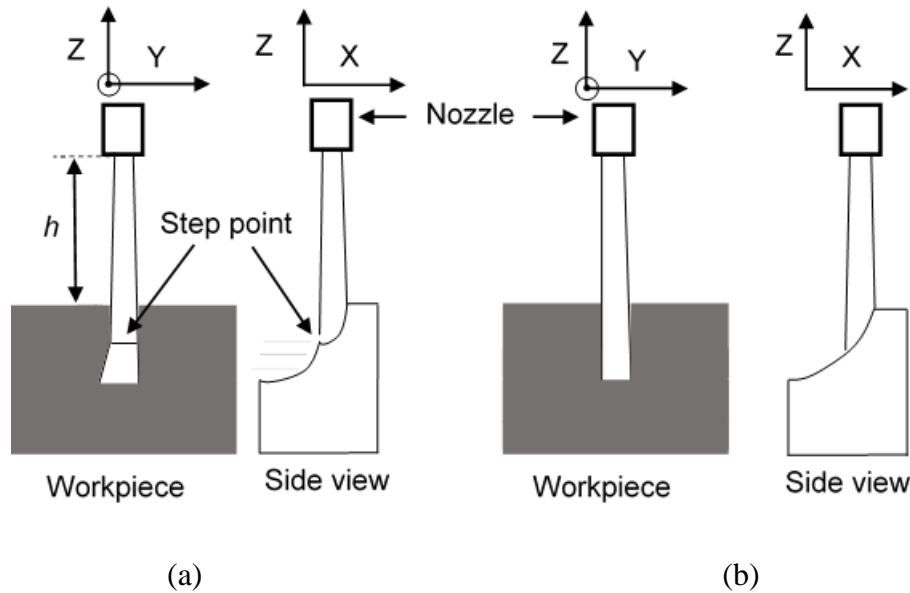
Figure 4-14 Process of formation of (a) asymmetric channels at relatively high traverse velocity of V_t=1000 mm/min with step on cutting front of channel (b) symmetric channel at a low traverse velocity of V_t=40 mm/min without step formation on the cutting front. Nozzle motion is in the direction of X-axis.

It is hypothesized that this accentuated the erosion produced by the jet once it was deflected to one of the sidewalls, thereby causing the eccentricity to grow quickly in that direction. At a low

traverse velocity there was no asymmetry simply because there was only one material removal mechanism, cutting erosion at glancing local particle impact angles, so that no steps were formed on the cutting front (Figure 4-14b).

The role of step formation in the creation of asymmetric channels was confirmed by machining a multi-pass (i.e. n=10 passes) channel at a high traverse velocity of V_t=1000 mm/min on a previously machined single-pass deep channel made at a low traverse velocity of V_t=40 mm/min. Although the pre-made symmetric channel had no steps as explained in Figure 4-14b, it quickly formed steps when the channel was deepened by the machining at the higher traverse velocity, and the jet was immediately deflected to the sidewall, rapidly forming an asymmetry as shown in Figure 4-15.
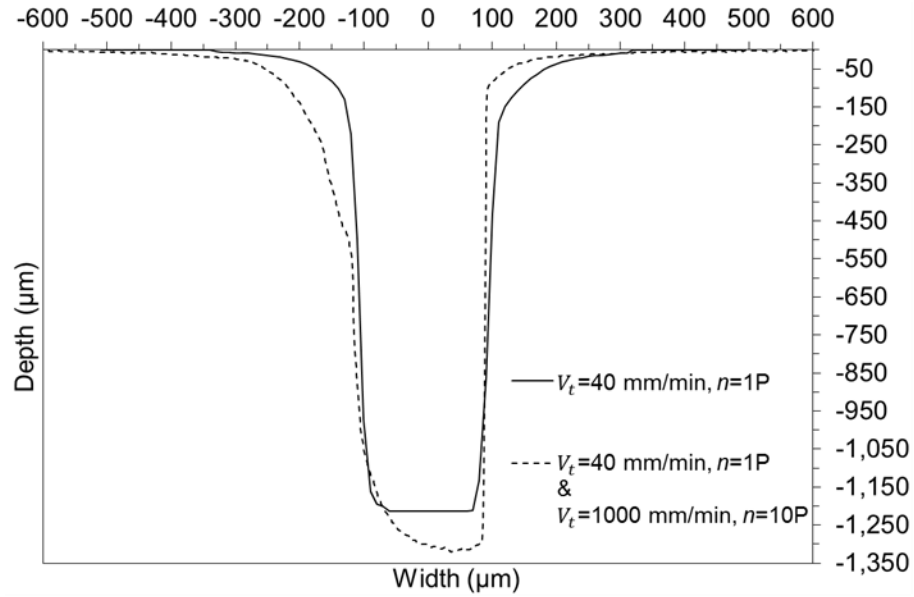
Figure 4-15 Cross-sectional profiles of (a) a single-pass deep channel made in Al6061-T6 at a low traverse velocity of V_t=40 mm/min, P_p=235 MPa, h=2 mm, AVP=25%, $W_{t,in}$=3wt%, θ=90°, and (b) a 10-pass channel made at a high traverse velocity of V_t=1000 mm/min on the previously machined channel of (a).

4.4. Summary

An innovative high-pressure abrasive slurry-jet micro-machining (HASJM) apparatus was developed from a relatively simple modification to a commercial high-pressure water jet. In contrast to previous setups, high-pressure slurry is not forced through an orifice, and therefore the new device can be used to micro-machine both ductile and brittle materials with minimal damage to the components of the nozzle. It was found that the kinetic energy of the particles, and thus the target erosion rate, was maximized at an entrained slurry flow rate of 77% of the water flow rate, roughly consistent with an optimum momentum transfer from the high-pressure water entering the mixing chamber through the orifice to the essentially stationary slurry entering the chamber. Some evidence of nozzle flooding was apparent at sufficiently high slurry flow rates. It was also found that HASJM provided smoother channels with less roughness and waviness when compared to those machined with AWJM. The choice of a suitable operating pressure, slurry flowrate, and concentration of particles depended on the properties of the target material. For example, the best conditions for glass were a lower water pump pressure and a slurry flow rate sufficiently high to flood the nozzle, whereas a higher pressure and the optimized slurry flow rate were best for machining aluminum.

Under identical jet conditions, as the standoff distance increased, the erosion rate of channels increased slightly in glass, but decreased in Al6061-T6. For both materials, the channel width increased with standoff, although the rate of increase was much higher for glass. These effects were attributed to differences in the local erosion rate at the periphery of the jet for the two materials.

Finally, it was found that the channels became highly asymmetric when multiple passes at relatively high traverse velocities ($V_t \sim 1000$ mm/min) were used to machine relatively deep (aspect ratio of 0.9 and larger) micro-channels in aluminum. The asymmetry did not occur when much lower traverse velocities ($V_t \leq 40$ mm/min) were used. These phenomena were explained in terms of jet deflection from steps on the cutting front that formed at higher traverse velocities. Overall, the study demonstrated that high-quality micro-channels can be machined in both ductile and brittle materials using the new HASJM apparatus with the appropriate operating conditions.

However, it was difficult to conclude whether the improvements in roughness and waviness using HASJM were simply due to using different particle type, size, and velocity or were caused by more fundamental reasons such as the effect of air in AWJM. Moreover, the effects of machining parameters (e.g. pressure, traverse velocity, dose of particles, and nozzle angle) on waviness, roughness, erosion rate, and the width of channels were not investigated. In next chapter, The effect of the entrained air in abrasive water jet micro-machining (AWJM) was isolated by comparing AWJM milled surfaces with those produced by high-pressure slurry jet micro-machining (HASJM) while maintaining a constant particle velocity and dose.

Chapter 5   Effect of Entrained Air in Abrasive Water Jet Micro-Machining: Reduction of Channel Width and Waviness using Slurry Entrainment

This chapter is based on the following published paper:

N. Haghbin, F. Ahmadzadeh, J. K. Spelt, and M. Papini, "Effect of entrained air in abrasive water jet micro-machining: Reduction of channels width and waviness using slurry entrainment," *Wear*, vol. 344-345, pp. 99-109, 2015.

5.1. Introduction

Abrasive water jet micro-machining (AWJM) and abrasive slurry jet micro-machining (ASJM) are water-jet based technologies for micro-machining a variety of materials such as metals, glass, ceramics, polymers, and composite materials. It is often important to minimize surface roughness and waviness in controlled-depth milling using these processes in order to prevent the need for further finishing operations [28].

The air that is entrained by an abrasive water jet can have three effects: a) it creates a nonhomogeneous three-phase jet in which the abrasive particles are carried and strike the target in a bubbly flow, b) it can lead to variations in the abrasive flow rate, and c) it causes an increase in the jet diameter [123,143].

The first effect causes a nonhomogeneous three-phase flow due to existence of air bubbles in the jet. For example, Chahine et al. [144] found that in a multi-phase flow, air bubbles can apply repulsive forces to small particles so that particles concentrate in the liquid phase. Firouzi et al. [145] demonstrated that, in a mixture of particles, air bubbles, and water, there is a high probability of particle-bubble collisions that affect particle motion. It is therefore expected that a non-uniform distribution of particles will occur in the abrasive water jets used for AWJM, which could lead to an increase in the surface waviness and roughness. The bubbly flow at the target could also lead to water drop erosion. For example, water droplets striking a solid surface can also generate a high 'water hammer' pressure, leading to plastic deformation as explained by Huang et al. [32]. Oka et al. [40] found erosion damage on an aluminum alloy by water droplet impingement depends on

water pressure and the nozzle standoff distance. Chillman et al. [39] observed that the injection of air into a plain water jet accelerates drop impingement erosion on an aluminum alloy surface due to the creation of water droplets at relatively lower standoff distances. However, Haghbin et al. [123] reported that the core region of submerged and unsubmerged water air jets did not break up into water droplets for standoff distances between 2 and 5 mm. The effect of the bubbly flow was found to be negligible in the present work, as discussed in Section 5.3.3.

The second effect of entrained air in AWJM can contribute to an increase in surface waviness due to the limitations of the particle/air feed systems used in AWJM. For example, abrasive flow can be affected by particle agglomeration resulting from high humidity or the generation of electrostatic forces, and by particle segregation as reported by Tang and Puri [146], and its effect on flowability [147]. Pak and Bechringer [148] reported that providing a uniform air flow rate in the particle/air feeder was key to having a consistent particle flow rate in nozzles used in AWJM. Bertho et al. [144] found that the instantaneous abrasive flow rate in a two-phase mixture of air and particles fluctuated at the output of the abrasive tube (Figure 5-1) due to the compressibility of the entrained air. Some solutions have been proposed for delivering a uniform particle flow in a particle/air system. For instance, Tardos and Lu [149] suggested using vibratory feeders, but these systems could not provide a constant flow rate for relatively small particles (e.g. cement with a diameter of 143 µm) due to powder bridging, compaction, and agglomeration. Some air abrasive blasting systems utilize a particle feeding system that creates an upward air flow, which is passed through the powder bed, generating a cloud of suspended particles (e.g. aluminum oxide of 25 µm), which then settles into a collection funnel connected to the nozzle, as described by Ghobeity et al. [150]. Such systems provide a more uniform air flow through the particles resulting in a more consistent particle flow than traditional vibrating hoppers. Yang et al. [150] suggested that Van der Waals attractive forces between micro-particles that lead to poor flowability can be reduced by applying a hydrophobic coating. Nevertheless, Haghbin et al. [123] found that significant mass flow rate fluctuations persisted with coated abrasive particles in AWJM using small (254 µm mixing tube diameter) nozzles due to inconsistent particle flow though the abrasive tube leading to the nozzle mixing tube. In the present work, such fluctuations were found to significantly affect the waviness of the channels made using AWJM (Section 5.3).

The third effect of entrained air, the increase in the jet diameter, is due to the formation of a diffuse, unsteady transition zone between the jet core and the surrounding air as described by Momber and Kovacevic [29]. Yanaida and Ohashi [43] and Huang et al. [32] found that a plain water jet breaks up after a certain standoff distance due to entrainment of surrounding air. Chillman et al. [39] concluded that the presence of entrained air in a water jet accelerates the break up into a droplet flow, compared to a plain water jet. Osman et al. [65] found that the water and air flows in the nozzle separate as a core jet of water surrounded by an annular air flow. Haghbin et al., [123] found that the AWJ emerging from a micro-nozzle had a core zone surrounded by a droplet zone. Later, Haghbin et al. [143] showed that the jet divergence angle in HASJM (1.5°) was smaller than that in AWJM (6.9°). In the present work, the effect of this difference in divergence on the channel width was quantified for the same channel depth and abrasive particle velocity (Section 5.3.3.1).

Particle kinetic energy has a large effect on the depth, waviness and roughness of micro-channels milled using abrasive jet processes [7]. Predicting or even measuring the particle velocity in such multi-phase flows can, however, be challenging. Narayanan et al. [81] developed an analytical model for abrasive particle velocities in AWJM systems considering the entrained air as a compressible fluid. Li et al. [80] used the momentum and continuity principles to predict particle velocity in a two-phase (i.e. air and abrasive) jet. Nouraei et al. [128] adapted this model to predict the particle velocity in a low-pressure abrasive slurry-jet micro-machining system that used a two-phase flow consisting of water and particles. The present HASJM system differs from that of Nouraei et al. [128] in that the abrasive slurry is injected into the high-pressure mixing tube of a water-jet machine, resulting in much greater particle velocities.

Measuring particle velocities in abrasive water jets using laser Doppler velocimetry [63] or particle image velocimetry [71] has proven to be unreliable due to difficulties in distinguishing abrasive particles in a mixture of abrasive, water and air. Later, Balz and Heiniger [152] found that particle velocity and size distributions could be measured within an abrasive water jet using PIV and the laser induced fluorescence of dyed abrasive particles. Balz et al. [153] also showed that ultra-fast X-ray particle velocimetry is a feasible method to measure particle velocities and spatial positions of individual abrasive particles in a three-phase jet consisting of abrasive, water, and air. Using magnetic particles in inductive methods [64] raises questions about whether the results are applicable to other abrasive particles. The impact force method [66] can only provide the net

impact velocity of the three-phase mixture. Ruff and Ives [153] introduced a double-disc apparatus (DDA) for measuring the average particle velocity in the free jet in abrasive air-jet micro-machining (AJM). This technique was applied to an abrasive water jet system by Liu et al. [72]; however, the measurements were not independently verified and were made using much larger nozzles than used in a micro-machining process.

In contrast to AWJM, no air enters HASJM systems, because the abrasive and water are first premixed in a separate container before being accelerated. The premixed slurry is then either pumped through the orifice [4], or entrained into the mixing tube of an AWJ nozzle and mixed with the high-speed water jet passing through the orifice [132]. The advantage of entraining the slurry is that less orifice damage occurs, since only water, rather than the slurry, passes through the orifice. Haghbin et al. [132] found that the abrasive flow rate stayed approximately constant during machining using an HASJM system. Preliminary observations under typical operating conditions indicated that the centerline waviness and roughness of micro-channels in such an HASJM system were less than in AWJM [143]. However, the particle type and size used in those two micro-machining methods were not identical, and the particle velocities were not measured. Hence, it was difficult to conclude whether the improvements in roughness and waviness using HASJM were simply due to these differences, or were caused by more fundamental reasons such as the effect of air in AWJM. Moreover, the effects of machining parameters (e.g. pressure, traverse velocity, dose of particles, and nozzle angle) on waviness, roughness, erosion rate, and the width of channels were not investigated.

In this chapter, the centerline waviness and roughness of micro-channels made in Al6061-T6 and SS316L using AWJM and HASJM were compared using the same 38 µm garnet abrasive particles at various water pump pressures, traverse velocities, and nozzle angles. The average particle velocities in the free jets of HASJM and AWJM were predicted and were verified using a double disc apparatus (DDA). This permitted the identification of the pressure and abrasive flow rate that generated the same particle velocity in both HASJM and AWJM, thereby yielding a direct comparison of surface quality, channel dimensions, and erosion rate in the two systems, one having entrained air and one that did not.

5.2. Experiments

5.2.1. Experimental setup and machining parameters

The AWJM and HASJM apparatuses were described in detail in Haghbin et al. [123] and Haghbin et al. [143], respectively. Briefly, Figure 5-1 shows a schematic of a prototype micro nozzle having an orifice diameter, d_O, of 127 µm and a mixing tube diameter of 254 µm installed on an OMAX 2626 Jet Machining Centre (OMAX Corp., Kent, Washington, USA), capable of water pump pressures, P_p, of up to 345 MPa. The OMAX machine could be easily switched between the AWJM and HASJM setups using a 3.2 mm inner diameter tube that connected the nozzle mixing tube to either the dry abrasive hopper or the abrasive slurry tank. The slurry flow rate was adjusted using a 3 mm abrasive slurry valve. The abrasive flow rate in AWJM was controlled by a 1.5 mm orifice at the bottom of the abrasive hopper.

Figure 5-2 shows the measured size distribution (38 µm average equivalent spherical diameter) of the treated 320-mesh garnet (Barton International, Glens Falls, NY, USA) that was used in all AWJM experiments [132]. A proprietary process was used to reduce particle agglomeration and improve the flowability of the micro-particles feeding from the hopper and in the abrasive feed tube [150]. The treated garnet, however, could not be used for HASJM because it repelled water and could not be mixed uniformly in the slurry tank. Therefore, an untreated version of the same 320-mesh garnet was used for all the HASJM experiments. The density and hardness of both treated and untreated garnet particles were virtually identical based on information provided by the supplier.

Table 5.1 shows the machining parameters used to mill straight, multi-pass micro-channels into 3×5×0.3 cm thick SS316L and Al6061-T6 samples using AWJM and HASJM. Up to n=8 multiple nozzle passes were used at different traverse velocities, V_t, and under different water pump pressures, P_p, with nozzle inclinations of θ= 90° and 45°. The effect of each experimental parameter was isolated by varying it individually while holding all other parameters constant at typical AWJM values. As explained below, experiments were also performed at a crossover condition, in which the average particle velocity, particle dose, and particle size and type were identical for both AWJM and HASJM.
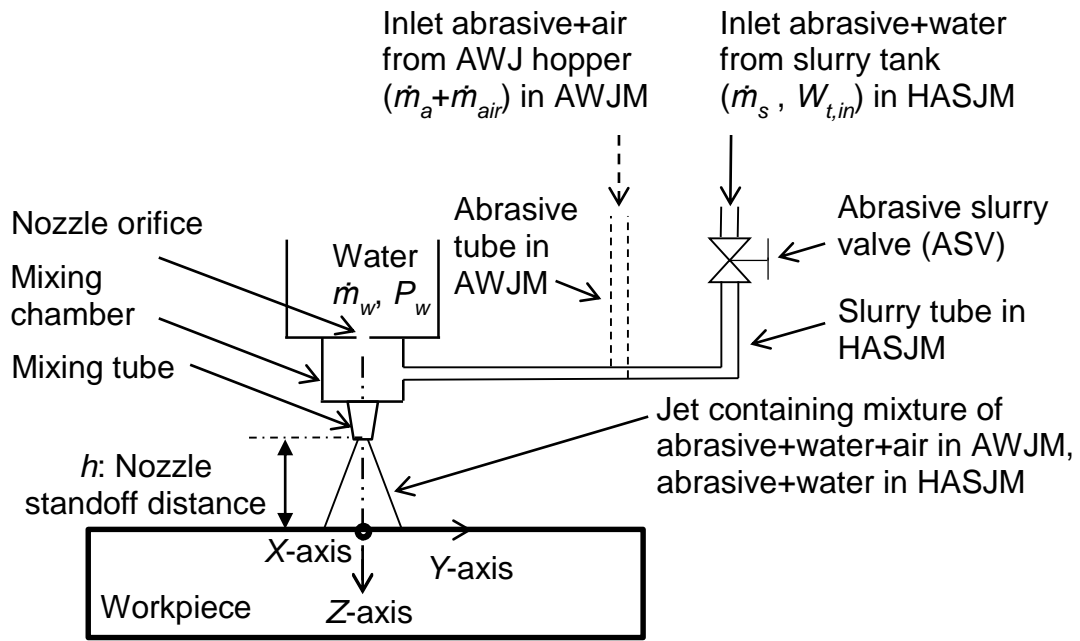
(a)
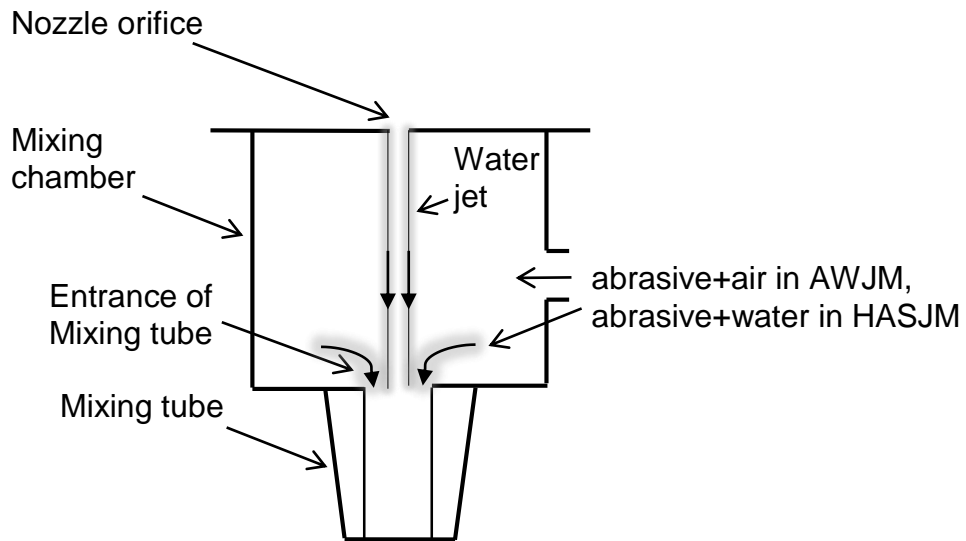
(b)

Figure 5-1 a) Schematic of the nozzle in the AWJM and HASJM systems. *X*-axis is along the channel length. b) Schematic of high-pressure water jet from the orifice entering the mixing tube and entraining abrasive in either air (AWJM) or water (HASJM). Not to scale.
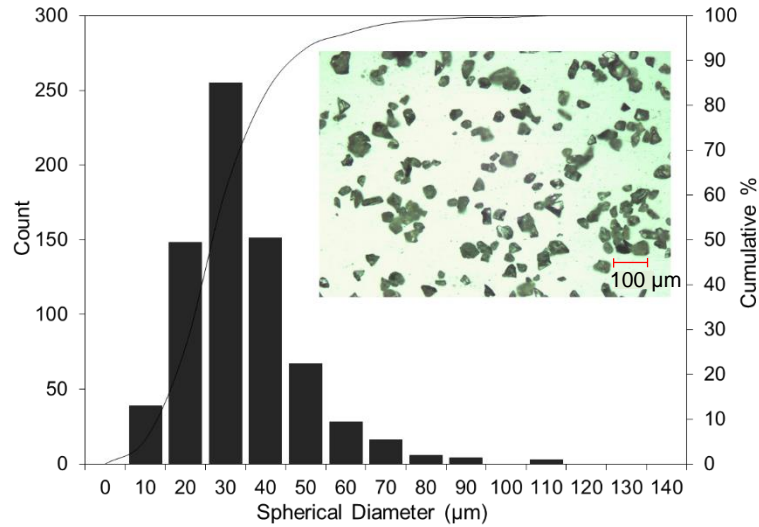
Figure 5-2 The size distribution and shapes of the surface-treated and untreated 320-mesh garnet. Curve gives cumulative percent [132].

Table 5.1. Process parameters used for HASJM, AWJM, and a crossover condition where the same abrasive dose and average particle velocity were achieved in both micro-machining processes.

	AWJM	HASJM	Crossover conditions
Standoff distance (mm), h	2	2, 5, 10	2
Abrasive type	treated garnet	untreated garnet	
Average abrasive diameter, d_p (µm)	38	38	
Inlet abrasive flow rate (g/min), $\dot{m}_a$	20-60	6, 6.94, 7.48	
Inlet slurry flow rate (g/min), $\dot{m}_s$	---	200, 231.3, 249.3	
Particle concentration of input slurry (%), $W_{t, in}$	---	3	3
Water pump pressure (MPa), P_p	137	194, 221, 277	137, 221
High-pressure water flow rate, $\dot{m}_w$ (g/min)	199	231.3, 255.5, 280.3	
Traverse speed (mm/min), V_t	1000, 2500, 4572	1000, 2500, 4572	4572
Nozzle angle (deg.), Θ	90°, 45°	90°, 45°	90°
Number of passes, n	2	4, 8	2, 8
Mixing tube length, mm	33	33	33
Workpiece material	Al6061-T6, SS316L	Al6061-T6, SS316L	Al6061-T6, SS316L
Average free-jet particle velocity, V_p (m/s)	255	226, 255, 275	255
Abrasive particle dose, M_a (g) for a 2-cm channel length			0.24
Effective jet diameter, d_j (µm)	455	285	455, 285

94

The effective jet diameter, d_j, in AWJM and HASJM was found by cutting through a foamed plastic (Renshape® material) as explained by Haghbin et al. [123,143]. The micro-channels were machined into the two target materials under identical conditions; i.e. multi-pass channels were machined on SS316L and Al6061-T6 samples placed side-by-side, and without turning off the jet. The samples were clamped to a stationary base that was placed at different standoff distances, h, below the nozzle (Figure 5-1) which moved at different traverse velocities, with a positioning accuracy of ±76 µm over 30 cm.

The resulting micro-channel profile shapes and centerline waviness and roughness were measured using a non-contact optical profilometer (model ST 400, Nanovea, Irvine, CA, USA) having lateral and vertical resolutions of 0.1 µm. Centerline waviness and centerline roughness were recorded as the average and standard deviation of three 2 cm long channels, measured using a Gaussian filter with a cut-off length of 0.8 mm (suggested by [154,155]) for roughness and waviness.

The erosion rate for both processes was expected to depend strongly on the abrasive particle velocity. It was therefore also of interest to machine channels using both AWJM and HASJM with the same free-jet particle velocity in order to isolate the effects of air in AWJM. The model of Narayanan et al. [81] was used to predict the particle velocity in AWJM. The model was adapted in Section 2.3.2 to allow prediction of particle velocity for the HASJM setup. All predicted results were verified experimentally using a double-disc apparatus. Table 5.1 shows the crossover machining conditions (i.e. P_p=134 MPa, n=2 in AWJM and P_p=279, n=8 in HASJM), for which the average free-jet particle velocity, V_p, and the abrasive particle dose, M_a, in AWJM and HASJM were the same.

5.2.2. Volumetric erosion rate

The volumetric erosion rates for AWJM and HASJM were calculated as

$$E = \frac{V_m}{M_a} \tag{5.1}$$

where M_a was the total abrasive mass consumed (i.e. abrasive particle dose) to remove a total volume of V_m from the target surface. The removed target volume was determined by calculating the average area of nine cross-sectional channel profiles (3 profiles for each of 3 separate

channels), and multiplying by the channel length. The mass of abrasive incident to the channel was an average of two measurements, one before and one after machining, in which the abrasive exiting the hopper or the slurry tank was collected and weighed. Significant variations in the abrasive mass flow rate are typical in abrasive water jet operations [75,76,77]. For example, in previous work, it was found that the abrasive mass flow rate reduced by 70% over a 20 min period [123]. Therefore, for AWJM, the machining time was kept as short as possible to minimize the variation in the abrasive flow rate for AWJM (i.e. 0.7 g for a machining time of 6 s at a traverse velocity of V_t=4572 mm/min).

5.2.3. Abrasive particle velocity

5.2.3.1. Double disc apparatus (DDA)

The average particle velocity in AWJM and HASJM was directly measured using a double disc apparatus (DDA). The principle of the DDA was explained in detail by Liu et al. [72]. Briefly, the present design consisted of two discs, fixed to a central shaft at a specified separation, and made to rotate rapidly using a 2 HP electric router (DeWalt, Model 621, Baltimore, MD) with a maximum angular velocity of 23,400 rpm (Figure 5-3). The particles in the jet passed through the four 1.5 mm wide slots on the upper rotating disc and generated four erosion scars on the recording disc placed on the lower rotating disc. The recording (lower) disc was made of Al6061-T6, because it remained undamaged by water droplets, and the resulting scars could thus be attributed to the particles alone [72].

The average velocity of the abrasive particles (V_p) was calculated from the angle, φ, (Figure 5-3) measured on the recording disc between a reference line directly below the centerline of the upper slot and a line through the center of the corresponding erosion scar, as described by Liu et al. [72]. Then the average particle velocity in the jet was given by

$$V_p = \frac{6\omega S}{\varphi} \tag{5.2}$$

where V_p is in m/s, S (m) is the distance between the upper disc and the recording disc as shown in Figure 5-3, ω (rpm) is the disc angular velocity and the scar angle φ is in degrees. The traverse velocity of nozzle was V_t=1000 mm/min in the radial direction of the rotary discs (Figure 5-3),

thereby creating a straight radial scar on the recording disc, reflecting the effect of the increasing tangential disk velocity as the jet moved radially outward. The total average free-jet particle velocity and its standard deviation were found by averaging φ for the four scars in three repeats separately measured in each of micro-machining processes.
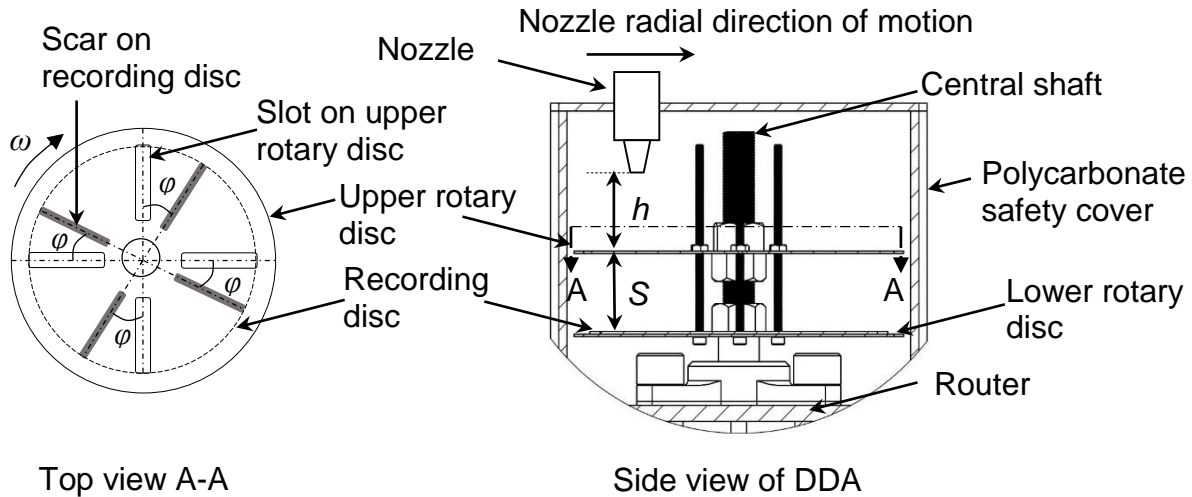
Figure 5-3 Experimental setup for double disc apparatus (DDA) used for measuring particle velocity in the HASJM and AWJM. Nozzle moved along the radial direction of the discs. Not to scale.

The high centrifugal forces prevented the formation of a water film of the recording disc so that the jet impacted an essentially dry recording disc each time. It is important to note that the DDA measured the average speed of particles in the free jet, and not the actual impact velocity of the particles. The latter will be less than the free-jet velocity because of particle deceleration caused by the displacement of the "squeeze film" of water between the particle and target at very small separations [96]. This deceleration occurs so quickly that it does not introduce a significant error in the measured free-jet particle velocity. The particle free-jet velocity was measured at different

97

standoff distances, h (mm), as shown in Figure 5-3c and Table 5.1. The DDA yielded an average particle velocity and could not measure the distribution of velocities within the jets.

5.2.3.2. Particle velocity prediction in AWJM and HASJM

As mentioned previously, the free-jet particle velocity in AWJM was determined using the approach of Narayanan et al. [81], which applied Bernoulli's equation and momentum and continuity principles in a three-phase flow consisting of water (i.e. a non-compressible fluid), air (i.e. a compressible fluid), and abrasive. This approach was modified in the present work to also predict the particle velocities of HASJM by assuming momentum exchanges between three nominal "phases" (high pressure water exiting the orifice, low pressure water in the slurry, abrasive in the slurry) in the mixing tube (Figure 5-1b). It was assumed that interactions in the mixing chamber were negligible since the high-pressure jet from the orifice entered the mixing tube directly, causing the abrasive to be entrained into the mixing tube along with either air (AWJM) or water (HASJM) (Figure 5-1b) [29]. The 28 mm long mixing tube (Figure 5-1) was divided into 1000 segments, based on a balance of computational time and accuracy. For example, trials with 10000 segments resulted in a 0.02 % difference in predicted velocity when compared with 1000 segments. Then the continuity equation was separately written for each phase within each segment as

$$\rho_w \frac{d\alpha_w u_w}{dz} = 0 \tag{5.3}$$

$$\rho_{w'} \frac{d\alpha_{w'} u_{w'}}{dz} = 0 \tag{5.4}$$

$$\rho_p \frac{d\alpha_p u_p}{dz} = 0 \tag{5.5}$$

where indices w, w', and p stand for the high-pressure water from the orifice, the low-pressure water in the slurry, and the abrasive particles, respectively, and the z-axis is along the centerline of the mixing tube as shown in Figure 5-1 The terms ρ_w, $\rho_{w'}$, ρ_p and α_w, $\alpha_{w'}$, α_p and u_w, $u_{w'}$, u_p are the densities, volume fractions and velocities of the high-pressure water, low-pressure water, and particles, respectively. Equation (5.4) differs from that in the Narayanan AWJM model, where the volume fractions of water, air, and particles changed while the jet moved through the mixing tube due to the compressibility of air. In the case of HASJM, which involves incompressible flows,

there was no need to update the density of any of the phases. The volume fraction, α of the incompressible flows of water and particles in the HASJM setup are:

$$\alpha_w = \frac{(\dot{m}_w/\rho_w)}{(\dot{m}_w/\rho_w)+(\dot{m}_{w'}/\rho_{w'})+(\dot{m}_p/\rho_p)} \tag{5.6}$$

$$\alpha_p = \frac{(\dot{m}_p/\rho_p)}{(\dot{m}_w/\rho_w)+(\dot{m}_{w'}/\rho_{w'})+(\dot{m}_p/\rho_p)} \tag{5.7}$$

$$\alpha_{w'} = \frac{(\dot{m}_{w'}/\rho_{w'})}{(\dot{m}_w/\rho_w)+(\dot{m}_{w'}/\rho_{w'})+(\dot{m}_p/\rho_p)} \tag{5.8}$$

where $\dot{m}_w$, $\dot{m}_{w'}$, and $\dot{m}_p$ are the flow rates of the high-pressure water, low-pressure water, and particles, respectively, and $\alpha_{w'} + \alpha_w + \alpha_p = 1$.

Following Narayanan et al. [81], the approach of Burns et al. [157] was used to model the drag interactions between the phases assuming that liquid phases could be modelled as a uniform dispersion of spherical elements. Therefore, the momentum equations for each of the two-phase pairs (i.e. high-pressure and low-pressure water phases, high-pressure water and particle phases, low-pressure water and particle phases) were

$$\rho_w \frac{d}{dz}(\alpha_w u_w^2) = F_D^{wp} + F_D^{ww'} \tag{5.9}$$

$$\rho_{w'} \frac{d}{dz}(\alpha_{w'} u_{w'}^2) = -F_D^{pw'} - F_D^{ww'} \tag{5.10}$$

$$\rho_p \frac{d}{dz}(\alpha_p u_p^2) = -F_D^{wp} + F_D^{pw'} \tag{5.11}$$

where F_D^{wp}, $F_D^{ww'}$, and $F_D^{pw'}$ are the drag forces between each pair of phases, found as

$$F_D^{wp} = \frac{1}{8}C_D A_{pw}\rho_w|u_p - u_w|(u_p - u_w) \tag{5.12}$$

$$F_D^{ww'} = \frac{1}{8}C_D A_{ww'}\rho_{w'}|u_{w'} - u_w|(u_{w'} - u_w) \tag{5.13}$$

$$F_D^{pw'} = \frac{1}{8}C_D A_{pw'}\rho_{w'}|u_{w'} - u_p|(u_{w'} - u_p) \tag{5.14}$$

where A_{pw}, $A_{ww'}$, and $A_{pw'}$ are the effective interaction areas between the particles and high pressure water, high and low pressure water, and particles and low pressure water, respectively, as defined below. Particle collisions were ignored by assuming that the phases were uniformly distributed. The drag coefficients, C_D, suggested by Crowe et al. [158] and applied to dispersed phases by Narayanan et al. [81], are also valid for the present HASJM case, as

$$C_D = \frac{24}{Re_d} f \tag{5.15}$$

$$f = 1 + 0.15 Re_d^{2/3} + \frac{0.0175 Re_d}{1 + 42500/Re_d^{1.16}} \tag{5.16}$$

$$Re_d = \frac{\rho_c (\Delta u) d_d}{\mu_c} \tag{5.17}$$

where subscripts c and d refer to continuous phase (i.e. a fluid phase within which abrasive particles or another fluid phase are distributed) and dispersed phase (i.e. abrasive particles or a fluid phase spread in a fluid phase), respectively. The terms f, Re_d, Δu, μ_c, ρ_c, and d_d are friction factor (i.e. a dimensionless factor related to shear stress between two phases), Reynolds number of the dispersed phase, the relative velocity of the two phases, the viscosity of the continuous phase, the density of the continuous phase, and the diameter of dispersed phase, respectively. In Eqs. (5.9) to (5.17), the continuous and dispersed phases in each pair of phases (i.e. w, w', and p) were assumed as w (i.e. continuous phase)- p (i.e. dispersed phase) and w' (i.e. continuous phase)- p (i.e. dispersed phase) and w (i.e. continuous phase)- w' (i.e. dispersed phase). Equations (5.15) and (5.16) are applicable for flows with Reynolds number up to 30,000, and therefore valid for both AWJM and HASJM.

Narayanan et al. [81] defined the interaction areas A_{pw}, $A_{ww'}$, and $A_{pw'}$, in terms of the volume fractions of the fluid phases as

$$A_{pw} = A_p \left(\frac{\alpha_w}{\alpha_{w'} + \alpha_w} \right) \tag{5.18}$$

$$A_{ww'} = A_w \left(1 - \alpha_p \right) \tag{5.19}$$

$$A_{pw'} = A_p - A_{pw} \tag{5.20}$$

where A_p, and A_w, were defined as [157]

$$A_p = \frac{6\alpha_p}{d_p} \tag{5.21}$$

$$A_w = \frac{6\alpha_w}{d_w} \tag{5.22}$$

where d_p is the average abrasive particle diameter. As mentioned above, the high-pressure water was modelled as a uniform dispersion of spherical elements of diameter of d_w, given by Narayanan et al. [81] as

$$d_w \approx d_j \left(\frac{\dot{m}_w}{\dot{m}_s + \dot{m}_w}\right) \tag{5.23}$$

The jet diameter, d_j, was measured for both AWJM and HASJM by cutting through a polymeric foam board as explained by Haghbin et al. [123].

The continuity and momentum equations (Eqs. (5.3) - (5.14)) were solved for each small segment of the mixing tube using a MATLAB (R2014a) code, so that the output results for each segment were taken as the initial conditions for the next segment. The initial velocity of the particles, high-pressure water, and low-pressure water at the entrance of mixing tube (Figure 5-1) were assumed u_{op}=0, $u_{ow} = \dot{m}_w/\rho_w$, and $u_{ow'}$=0, respectively. It was assumed that the particle velocity in the radial direction of each cross section of the mixing tube was constant.

5.3. Results and discussion

5.3.1. Particle velocity in the AWJM and HASJM

The particle velocity model of Section 5.2.3 was verified by comparison with the DDA experiments performed at three water pump pressures of P_p=194, 235 and 279 MPa using both AWJM and HASJM (Figure 5-4).
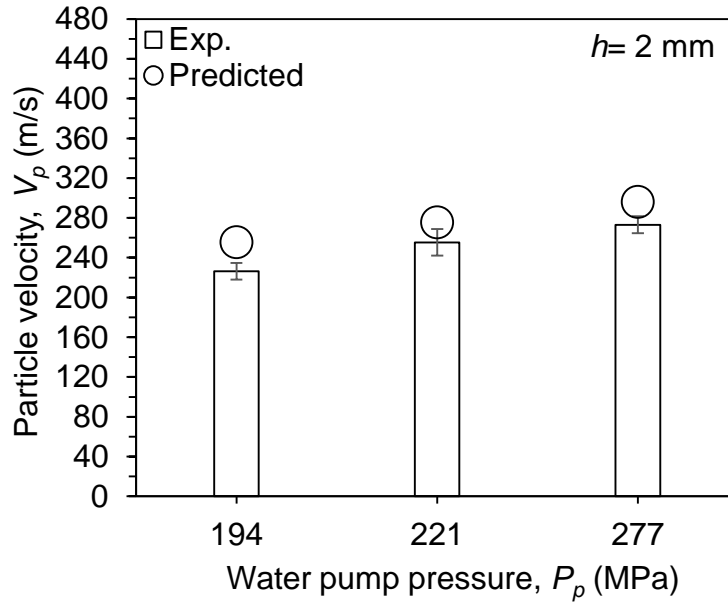
(a)
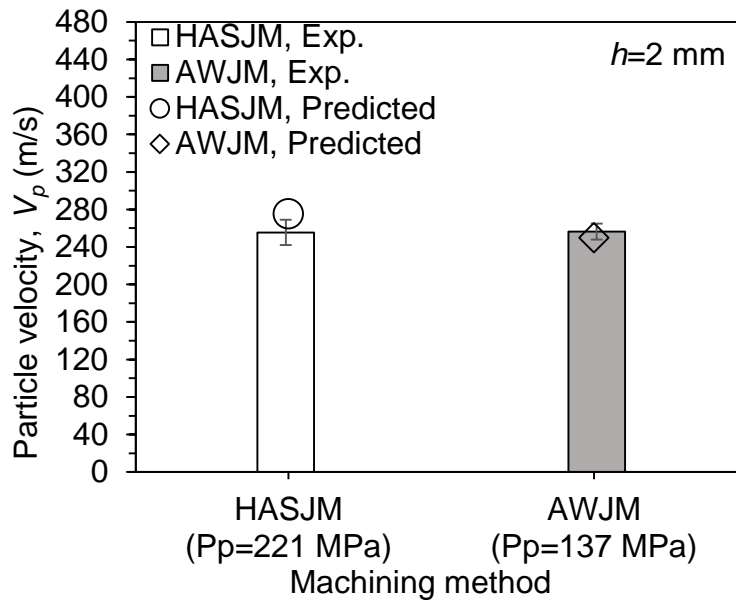
(b)

Figure 5-4 Average predicted free-jet particle velocity, V_p, compared with the DDA measurements for (a) HASJM at different water pump pressures, (b) particle velocity for HASJM and AWJM at the crossover condition: HASJM P_p=221 MPa and AWJM at P_p=137 MPa at a standoff distance of h=2 mm. Scatter bars represent ±1 standard deviation for three separate measurements with 4 scars each.

Table 5.1 gives the corresponding measured high-pressure water mass flow rates through the orifice and the flow rates of the water and abrasive particles entrained from the slurry tube [143]. The densities of the garnet particles and water were taken as 4,000 kg/m^3 and 1,000 kg/m^3, respectively. The average free-jet particle velocity at the HASJM nozzle exit predicted by the model was V_p=226 m/s at P_p=194 MPa, and rose with increasing pressure (Figure 5-4a) to V_p=273 m/s at P_p=277 MPa. The DDA measurements had an average standard deviation of 8.6 m/s. It was found that the model over-predicted the DDA measured values by an average of 9%. Figure 4b shows that the particle velocity at the lower water-pump pressure of P_p=137 MPa in the AWJM was approximately equal to that at the high water-pump pressure of P_p=221 MPa in HASJM (i.e. V_p≈255 m/s). This crossover condition in particle velocity while using the same abrasive dose by varying the number of passes, as shown in Table 5.1, allowed the roughness and waviness of channels micro-machined using both systems to be compared directly (Section 5.3.3).

5.3.2. W_a and R_a for AWJM and HASJM-Trends with pressure and dose

5.3.2.1. Effect of pressure

Che et al. [159] showed theoretically that surface roughness in ductile materials depends on particle velocity, which increases with pressure for AWJM. This has been confirmed by the observations of a number of authors. For example, Cenac et al. [160] observed that the surface roughness of composite materials increased slightly with increasing a pressure during AWJ milling. The same trends in roughness and waviness with pressure were reported by Shipway et al. [28] for the AWJ milling of a titanium alloy. Ojmertz [161] found that in the AWJ milling of steel and aluminum alloys, waviness increased sharply with rising pressure.

Figure 5-5 confirmed that the centerline waviness, W_a, and roughness, R_a, of micro-channels machined in Al6061-T6 and SS316L in both AWJM and HASJM increased with increasing water pump pressure, P_p. As particle velocity increased with a pressure (Figure 5-4a), the indentations became deeper and thus the centerline waviness and roughness became larger. The average centerline waviness and roughness of channels made in Al6061-T6 (Figure 5-5a) in both machining processes were overall 2.6 and 1.5 times higher than in SS316L, respectively (Figure 5-5b). This was due to the relatively lower erosion rate of SS316L than Al6061-T6 (i.e. 2.1 times
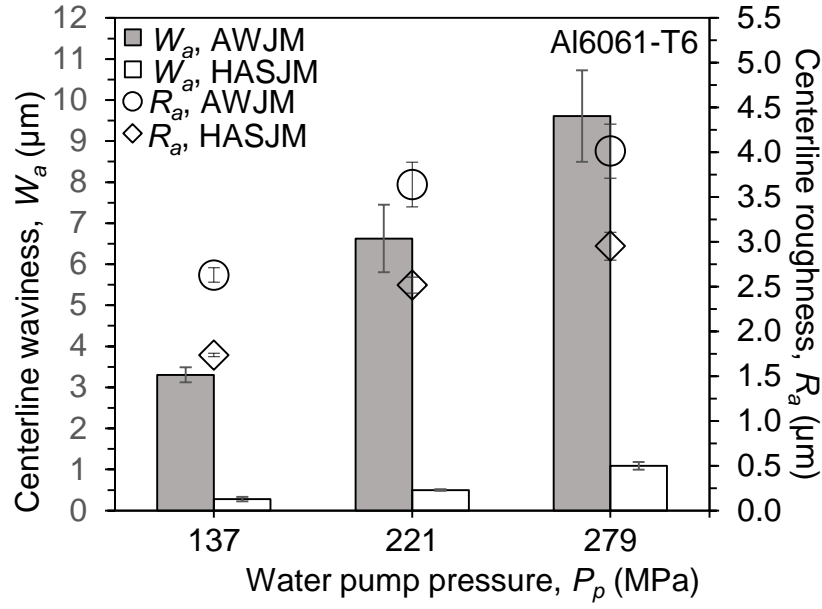
(a)
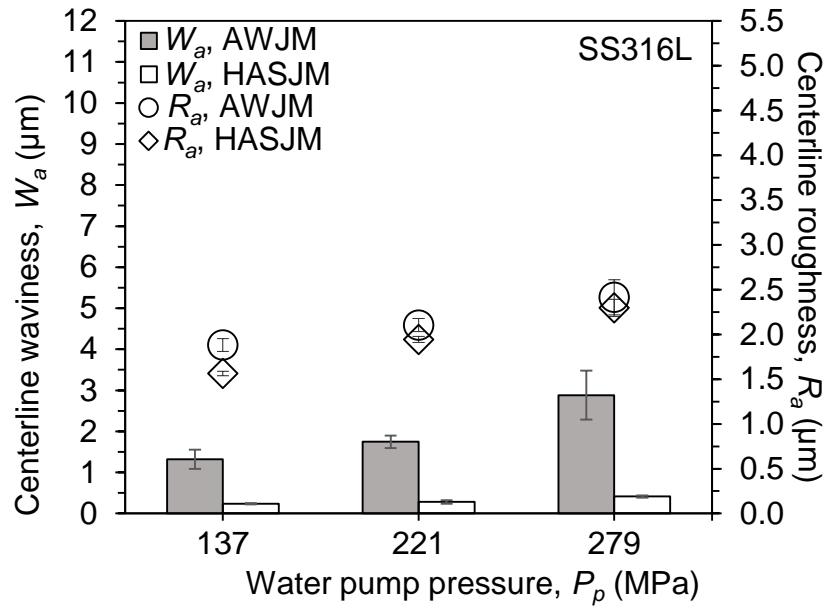
(b)

Figure 5-5 Variation of centerline waviness, W_a, and centerline roughness, R_a, versus pressure for micro-channels made in (a) Al6061-T6 and (b) SS316L using AWJM (n=2 passes) and HASJM (n=8 passes) at V_t=4572 mm/min, h=2 mm. Scatter bars represent ±1 standard deviation for three separate measurements.

smaller). The much higher variation in waviness for AWJM seen in Figure 5-5 is better discussed under conditions of identical particle dose and velocity, in Section 5.3.3.1.

5.3.2.2. Effect of particle dose at the same particle velocity

Figure 5-6 shows the centerline waviness, W_a, and centerline roughness, R_a, of micro-channels machined using either AWJM or HASJM as a function of abrasive particle dose, M_a, controlled by varying the traverse velocity, V_t. As the traverse velocity increased from 1000 to 4572 mm/min, W_a decreased by 76% and R_a decreased by 45%, while for HASJM, W_a decreased by 81% and R_a decreased by 10%. It was hypothesized that W_a decreased with the increasing traverse velocity because of a decrease in particle dose. Because the number of passes in the two processes was different, the effect of the leading edge angle on erosion rate and surface morphology in AWJM and HASJM was different. For example, over this range of traverse speeds, the centerline depth in AWJM ranged from 19 to 161 µm, and from 18 to 121 µm in HASJM. The leading edge angle of micro-channels made in Al661-T6 and SS316L (Figure 5-6a,b) increased with a decrease of traverse velocity from 3° to 18° and 2° to 8° in AWJM and from 1° to 4° and 0.5° to 1.5° in HASJM, respectively. The W_a increased with dose (lower scan speed) for both machining processes due to the tendency to form more irregularities (that was enhanced by further passes) at a lower traverse velocity [6]. The waviness was much worse in AWJM due to the greater variation in the abrasive mass flow rate associated with the presence of air [149].

The R_a at a relatively low traverse velocity in AWJM was 1.5 times higher than that in HASJM. Furthermore, it is seen that the difference in R_a between the two processes for SS316L (Figure 5-6b) was smaller than in Al6061-T6 (Figure 5-6a). The R_a was different at a low traverse velocity because the leading edge of the kerf formed in the traverse direction is sloped differently for AWJM (2 passes, high slope of 18°) and HASJM (8 passes, low slope of 4°). At a high traverse velocity, the slope of the leading edge was about the same for both processes. In order to minimize the effect of leading edge slope on roughness so that the effect of air could most accurately be assessed, the channels resulting from the highest traverse velocity of V_t=4572 mm/min and the same particle velocity of 255 m/s (Table 5.1) will be discussed in more detail in Section 5.3.3.
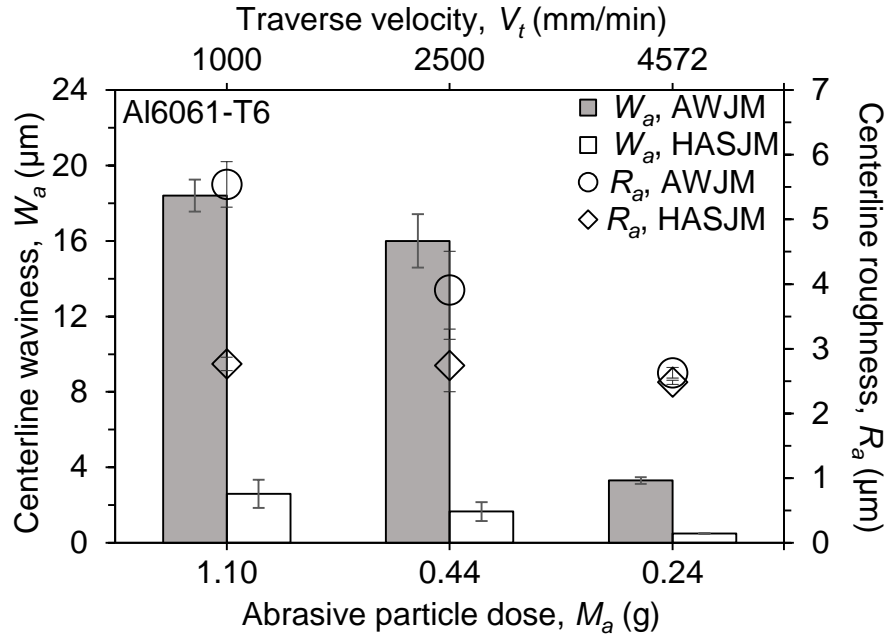
(a)
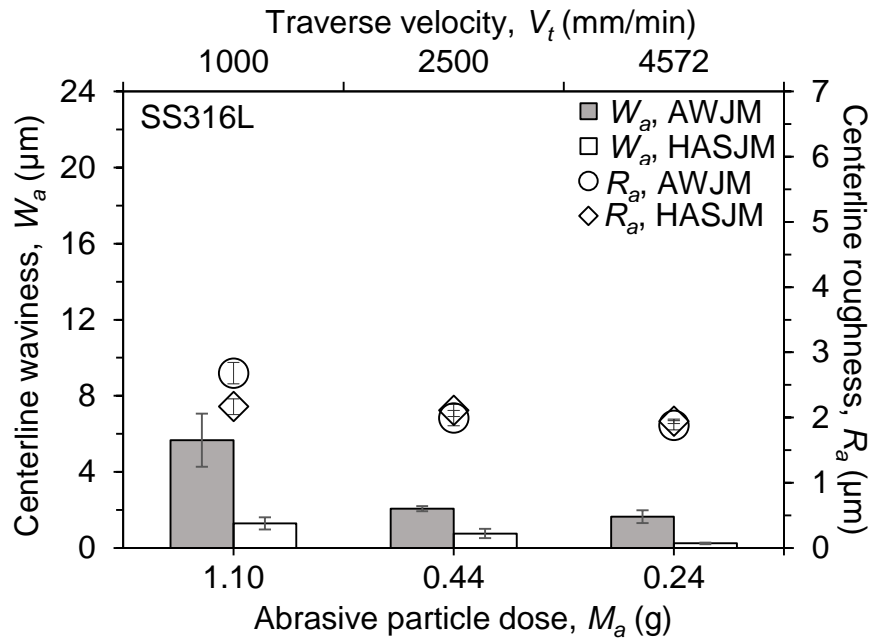
(b)

Figure 5-6 Variation of centerline waviness, W_a, and centerline roughness, R_a, as a function of abrasive particle dose, M_a, for micro-channels made in (a) Al6061-T6 and (b) SS316L, using AWJM (P_p=137 MPa, n=2 passes) and HASJM (P_p=221 MPa, n=8 passes) at h=2 mm. Scatter bars represent ±1 standard deviation for three separate measurements.

5.3.3. Comparison of AWJM and HASJM at the same particle velocity and dose-effect of air

In Section 5.1, three possible effects that the air that is entrained by an abrasive water jet can have on the resulting erosion at the surface were identified. Since the crossover condition in Table 5.1 allowed AWJM (air entrained) and HASJM (no air entrained) to be conducted at the same particle velocity and dose, it allowed for a direct assessment of the effect of air.

The first effect, i.e., bubbly flow at the surface, causing drop impingement erosion, was investigated by milling Al6061-T6 and SS316L using a water/air jet (i.e, an AWJM setup without abrasive, but still entraining air) at P_p=137 and 221 MPa, V_t=4572 mm/min, n=2 passes, h= 2 mm. In all cases, there was negligible erosion of the two target metals, consistent with previous work by Haghbin et al. [123] who showed that a water/air jet could not erode a metal surface when the standoff distance, $h \leq 5$ mm because the jet core did not break up into water droplets. While it is possible that an impinging air/water/abrasive jet in AWJM could result in erosion due to a synergy between particles and liquid drops or bubbles, the fact that the air/water jet caused no damage indicates that the overall effect of the bubbly flow on erosion was very likely small.

5.3.3.1. Erosion rate and channel dimension at the same particle velocity and dose

Figure 5-7a compares the volumetric specific erosion rates (Eq. (5.1)) of micro-channels made using the same particle velocity and dose (i.e. 0.24 g for a channel length of 2 cm, Table 5.1 crossover condition) in AWJM and HASJM. As discussed above, under these conditions the only difference between the processes was the presence of the entrained air in the AWJM. It is seen that the entrained air increased the erosion rate in AWJM so that it was approximately 26% greater than that for HASJM in Al6061-T6, and 29% greater in SS316L.

The differences in erosion rate were caused by the entrained air in AWJM which produced a wider jet (i.e. d_e~455 µm in AWJM and d_e~285 µm in HASJM, Table 5.1), leading to a wider channel. For example, Figure 5-7b shows that the micro-channels made with HASJM were about 26% narrower than those made with AWJM. As discussed in Section 5.1, while there was a core jet area in both machining processes, the entrained air in AWJM was distributed more in the peripheral jet area [43] where it produced a droplet zone around the core zone [123] and increased the jet diameter. Therefore, the wider jet in AWJM created wider channels than in HASJM. It was found that the
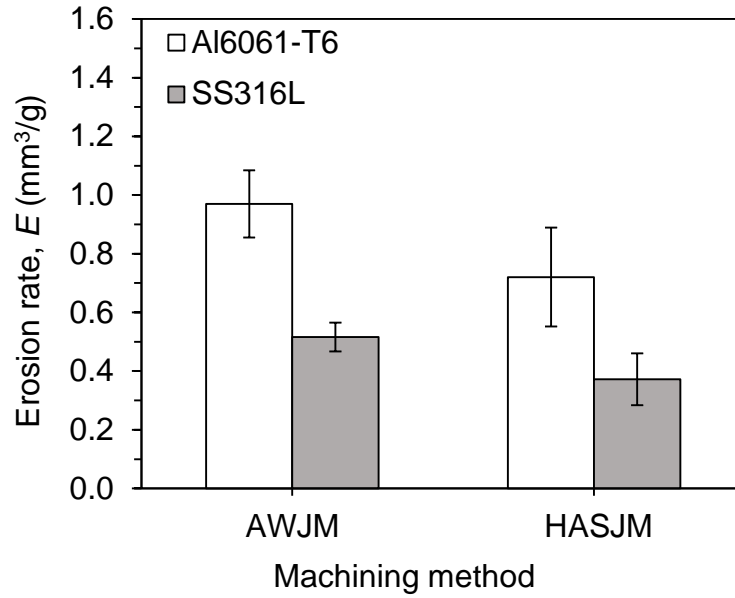
(a)
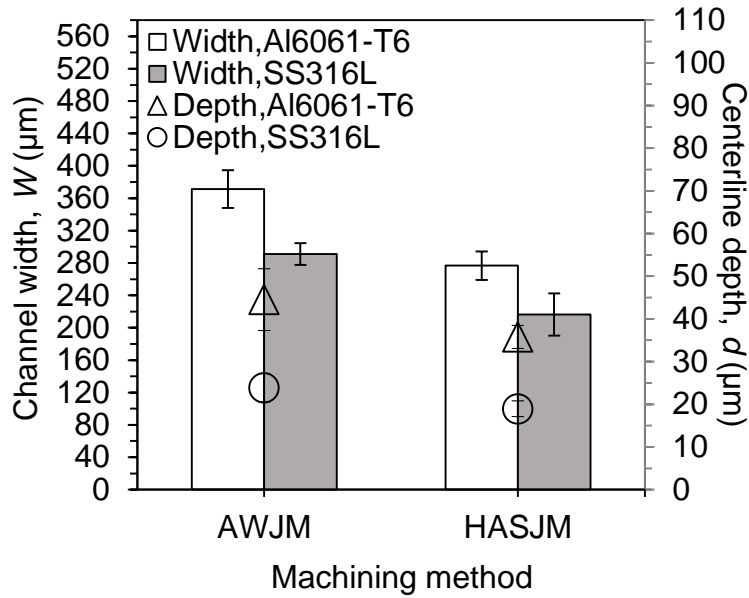
(b)

Figure 5-7 Micro-channels made at $\theta=90°$ in Al6061-T6 and SS316L using the same particle velocity and dose in AWJM (P_p=138 MPa, n=2 passes) and HASJM (P_p=221 MPa, n=8 passes) at V_t=4572 mm/min, h=2 mm: (a) Volumetric specific erosion rate, E, (b) Centerline depth, d, and width, W. Scatter bars represent ±1 standard deviation for three separate measurements.

normalized channel widths for Al6061-T6 and SS316L (i.e. width divided by effective jet diameter) were, respectively, 82% and 64% in AWJM, and 97% and 76% in HASJM. Since the channels machined with HASJM were narrower than those machined with AWJM, they were filled with water to a greater depth, thereby causing greater particle deceleration through the water-filled channel as described by Haghbin et al. [123]. This smaller particle impact velocity in HASJM compared with AWJM led to the slightly shallower (20% smaller) channel centerline depths in HASJM seen in Figure 5-7b for the crossover condition.

Figure 5-8 shows that the cross-sectional profiles of micro-channels of about the same depth made by AWJM and HASJM at the same velocity and dose were very similar in shape, although they differed in width as discussed above.
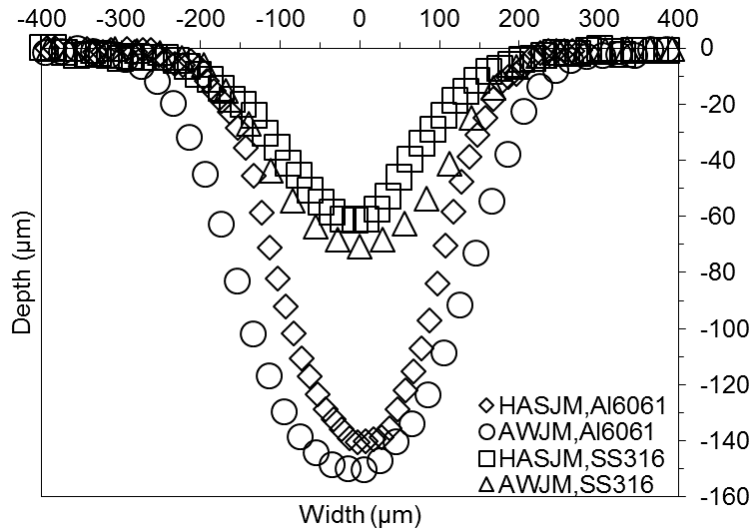
Figure 5-8 Typical cross-sectional shapes of micro-channels of approximately the same centerline depth made at the same particle velocity in Al6061-T6 using AWJM at P_p=138 MPa, n=2 passes, and HASJM at P_p=221 MPa, n=8 passes, V_t=1000 mm/min, θ=90°. Note difference in depth and width scales.

5.3.3.2. Effect of nozzle angle on W_a and R_a at the same particle velocity and dose

Considering first the data for a nozzle angle of $\theta=90°$, Figure 5-10 shows that the waviness of channels made with AWJM was significantly larger than with HASJM at the same particle velocity and dose made at $V_t=4572$ mm/min. However, the roughness was approximately the same for the two processes. It was hypothesized that the larger waviness of the micro-channels created by AWJM were due to greater fluctuations in the abrasive flow rate in the particle-air feed system, as discussed in Section 5.1. The nozzle inclination angle affects the flow field in the jet footprint, with smaller angles causing a greater fraction of the flow to be directed axially along the channel rather than toward the sidewalls adjacent to the footprint [161]. It was of interest to compare the magnitude of this effect in AWJM and HASJM at the same average particle velocity and dose. With a nozzle inclination of $\theta=45°$, machining in the "backward" direction (Figure 5-9a) was indistinguishable from machining in the "forward" direction (Figure 5-9b), with no statistically significant differences (t-test, 95% confidence) in W_a and R_a of channels in Al6061-T6 and SS316L (Figure 5-10) for either process.

(a) (b)
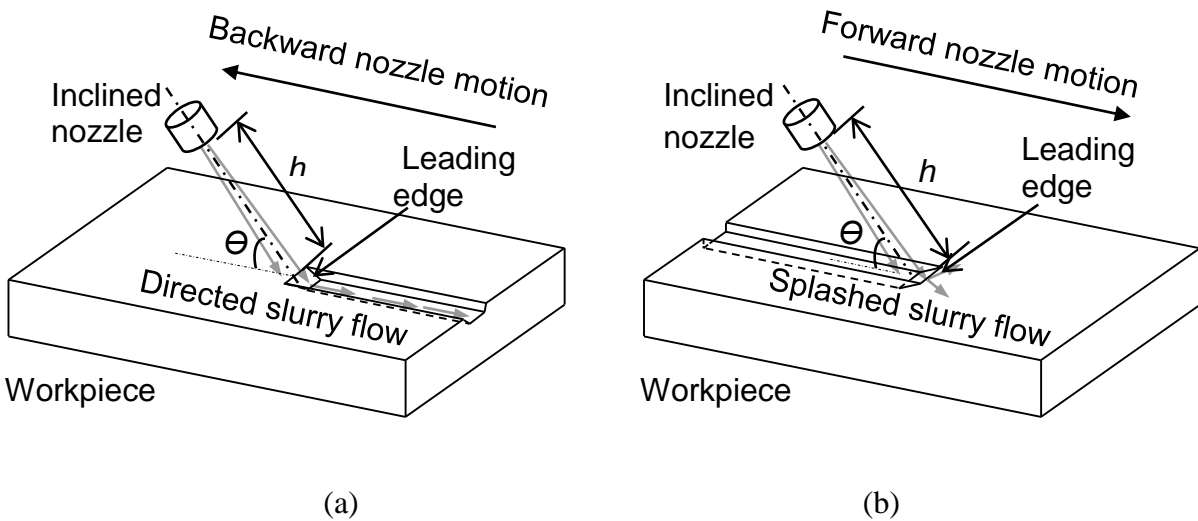
Figure 5-9 Micro-milling in AWJM and HASJM with a nozzle at global angle of $\varTheta=45°$ at standoff distance, h in form of (a) backward machining with the slurry flow along the length of the machined channel, (b) forward machining with the slurry deflecting from the leading edge. Not to scale.
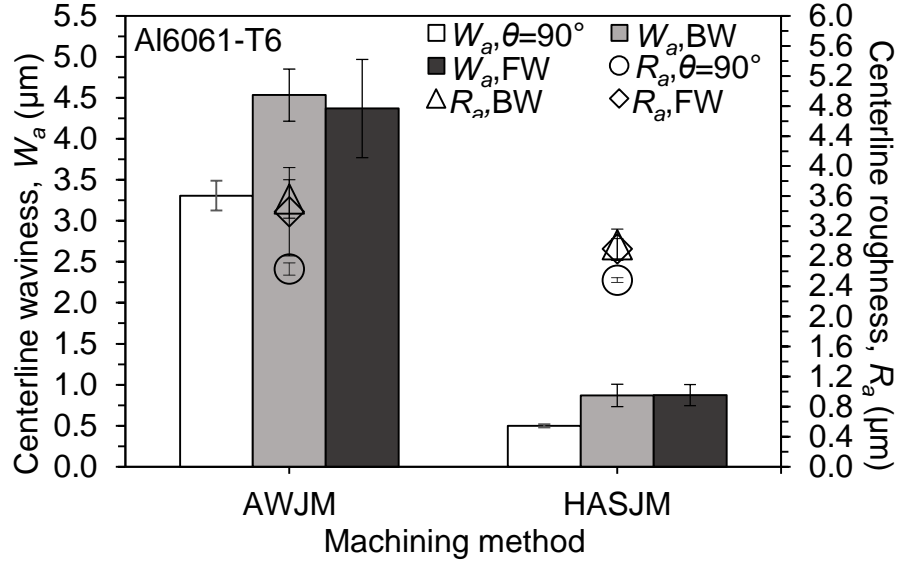
(a)
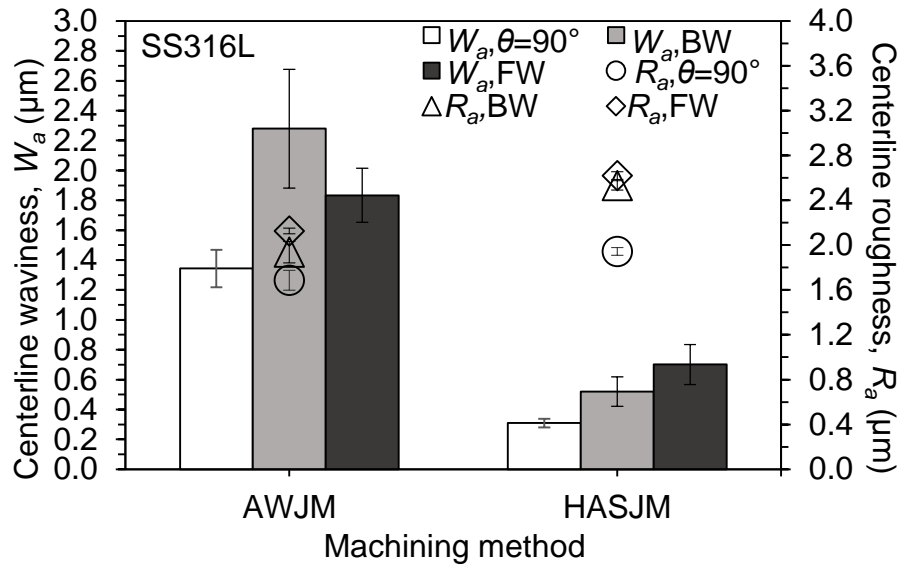
(b)

Figure 5-10 Comparison of AWJM and HASJM using the same particle velocity and dose. Centerline waviness, W_a, and centerline roughness, R_a, of micro-channels made at $\theta=90°$ and $\theta=45°$ (Backward-BW, Forward-FW) in: (a) Al6061-T6, and (b) SS316L using AWJM ($P_p=138$ MPa, $n=2$ passes, $V_t=4572$ mm/min) and HASJM ($P_p=221$ MPa, $n=8$ passes, $V_t=4572$ mm/min) at $h=2$mm. Scatter bars represent ±1 standard deviation for three separate measurements.

The similarity of the forward and backward results is explained by the relatively small slope of the leading edge of the machining front as discussed in Nouraei et al. [128].

The width of channels at $\theta=45°$ in AWJM was $W=440$ µm in Al6061-T6 and $W=371$ µm in SS316L, while the comparable widths with HASJM were $W=350$ µm in Al6061-T6 and $W=227$ µm in SS316L. The centerline depth of channels in backward and forward machining in both processes were almost the same (i.e. $d=85$ µm in Al6061-T6 and $d=42$ µm in SS316L). These width and depth trends were similar to those seen at $\theta=90°$, but the values a $\theta=45°$ were larger because the erosion rate in these metals increased with decreasing particle impact angle [132].

In both forward and backward machining, inclining the nozzle at $\theta=45°$ increased both the waviness and roughness compared with machining at $\theta=90°$. This was attributed to the smaller water stagnation zone leading to a higher impact velocity at a nozzle angle of 45° compared to 90° [98]. Regardless of the nozzle angle, however, W_a was always greater in AWJM, and R_a was always the same or slightly greater in HASJM. The increase in waviness and roughness with decreasing nozzle angle (Figure 5-10) is opposite to the trend reported for the slurry jet polishing of optical surfaces made of glass where small nozzle angles are recommended to minimize roughness [163]. For the polishing of glass, the decrease in nozzle angle resulted in lower impact energy transfers normal to the surface, leading to a smaller chip being removed, a lower erosion rate, and ultimately a lower roughness [164]. In contrast, the erosion rate in metals increases with decreasing impact angle [155]. Moreover, the much higher kinetic energy of particles in AWJM compared to slurry jet polishing produces a very high erosion rate at low impact angles, but in jet polishing the very low particle kinetic energy limits low-angle erosion to just the peaks of asperities, thereby smoothing the surface [165].

The results of Sections 5.3.2 and 5.3.3 are summarized in Table 5.2, which gives the properties of the micro-channels made with AWJM relative to those made with HASJM at the crossover condition, and as pressure, dose and jet angle were changed.

Table 5.2. Summary of properties of micro-channels made with AWJM and HASJM. At the crossover condition, the differences were due solely to the effects of entrained air in the abrasive feed system of AWJM.

	AWJM relative to HASJM	
Crossover condition: equal particle velocity in free jet and equal particle dose		
Channel width	26% wider	
Channel depth	20% deeper	
W_a	4.7x greater	
R_a	Approx. the same	
Specific erosion rate	27% greater	
Effect of increasing pressure, dose, jet inclination on AWJM and HASJM		
W_a	Increases	
R_a	Increases	

5.4. Summary

In this chapter, the particle velocities in the jets produced in abrasive water-jet micro-machining (AWJM) and high-pressure slurry-jet micro-machining (HASJM) were predicted using a model and verified using a double disc apparatus (DDA). This facilitated the prediction of the pressures and abrasive flow rates required to generate equal free-jet particle velocities (V_p~255 m/s) in both processes. These conditions permitted a direct assessment of the effects of the air in the jet in AWJM on the quality (i.e. centerline waviness and centerline roughness) and dimensions of micro-channels made in Al6061-T6 and SS316L using the same abrasive particle size (i.e. d_p=38 µm) and type (i.e. garnet). At this crossover condition (i.e. identical free jet particle velocity and equal abrasive dose at a high traverse velocity), the erosion rate in AWJM was about 27% higher in both metals than that in HASJM. This was due an increase in the channel width caused by the wider jet in AWJM resulting from the entrained air. The centerline waviness, W_a, of micro-channels made in SS316L and Al60661-T6 using HASJM at this crossover condition were typically 4.7 times smaller than those made with AWJM due to the various possible effects of air in the AWJM (e.g. providing a nonhomogeneous jet and non-uniform abrasive flow rate). The centerline roughness, R_a, was approximately the same in both processes at a traverse velocity of V_t=4572 mm/min and a nozzle angle of 90°.

It was observed that the W_a and R_a were significantly reduced in both micro-machining techniques with a decrease in pressure, traverse velocity, and particle dose. The waviness and roughness in both processes at a nozzle angle of $\theta=90°$ were lower than at $\theta=45°$ due to the erosion characteristics of ductile metals at an inclined nozzle angle. The W_a of micro-channels with the same depth in HASJM were much smaller than those in AWJM, by factors of 6.6 (Al6061-T6) and 4.3 (SS316L), while the R_a in both processes were similar. In general, the higher erosion rate in Al6061-T6 compared with SS316L produced larger changes in W_a and R_a as the process parameters (e.g. pressure, traverse velocity, dose of particles, nozzle angle) were changed.

It was concluded that the entrained air in AWJM resulted in a relatively high waviness compared to HASJM due to variation in the abrasive flow rate in the air/particle feeding system, but the effect of the bubbly flow on erosion and waviness was most likely ignorable. The entrained air surrounded the peripheral area of the core jet, increased the AWJ size, and led to a growth of channel width in AWJM.

Chapter 6 Summary and Conclusions

6.1 Summary

Abrasive water jet technology can be used for micro-milling using recently developed miniaturized nozzles. Chapter 2 compared the performance of submerged and unsubmerged abrasive water jet micro-milling of channels in 316L stainless steel and 6061-T6 aluminum at various nozzle angles and standoff distances. The effect of submergence on the diameter and effective footprint of AWJ erosion footprints was measured and compared. Chapter 3 used the results of previous chapter to develop a new surface evolution model that predicted the size and shape of relatively deep micro-channels resulting from unsubmerged and submerged abrasive water jet micro-machining (AWJM). A novel high-pressure (water pump pressure up to 250 MPa) abrasive slurry micro-machining (HASJM) system was introduced in Chapter 4. By feeding a premixed slurry into the mixing chamber of a water jet machine with a micro-nozzle (mixing tube diameter of 254 µm), premature erosion of system components was avoided. Channels produced by micro-milling Al6061-T6 and glass using a 25 µm aluminum oxide had smaller waviness and roughness than those made with the conventional abrasive water jet using a 38 µm treated garnet in which air and abrasive entered the mixing chamber. In Chapter 5, the effect of the entrained air in abrasive water jet micro-machining (AWJM) was investigated by comparing AWJM milled surfaces with those produced by high-pressure slurry jet micro-machining (HASJM) while maintaining a constant particle velocity. The effects of air on the quality (i.e. centerline waviness and centerline roughness) and dimensions of micro-channels made in Al6061-T6 and SS316L by AWJM and HASJM using the same abrasive particle size (i.e. d_p=38 µm) and type (i.e. garnet) with an identical free jet particle velocity (V_p~255 m/s) were determined.

6.2 Conclusions

The main conclusions of this dissertation are:

i. Unsubmerged micro-milling created micro-channels that were significantly wider than those milled with the submerged jet because of increased drag on the jet periphery.

ii. The instantaneous centerline erosion rate and volumetric erosion rates in AWJM decreased with channel depth due to jet spreading and stagnation zone.

iii. The decrease in erosion rate due to the stagnation zone is only a function of channel geometry, and was independent of the standoff distance, jet angle, jet direction (forward or backward machining) and whether the jet was submerged or in air.

iv. A major advantage of submerged abrasive waterjet micro-machining compared to its use in air, is that it is possible to machine narrower channels, thereby increasing the resolution of the process without reducing the centerline etch rate. Moreover, it reduced noise and released less abrasive debris into the air.

v. Surface evolution in AWJM was found to occur in a two-stage process. A surface evolution model was developed to predict the cross-sectional profiles of relatively deep channels, based on modifications of an existing air jet model to account for these two stages which brought about nonlinear changes in depth and other effects not previously considered.

vi. The model was found to work equally well when the water jet was submerged and when it was used in air, and when machining was in the forward or backward directions.

vii. Channel depths predicted to within approximately 4%, while the average error in the predicted channel width at half the depth was less than 16%, and the maximum error of the predicted sidewall slopes was less than 3%.

viii. A HASJM apparatus was developed from a relatively simple modification to a commercial high-pressure water jet. It produced a much lower micro-channel waviness than AWJM, and was shown to be effective for micro-milling both ductile and brittle materials with minimal damage to the components of the nozzle. The choice of a suitable operating pressure, slurry flowrate, and concentration of particles depended on the properties of the target material. For example, the best conditions for glass were a lower water pump pressure and a slurry flow rate sufficiently high to flood the nozzle, whereas a higher pressure and the optimized slurry flow rate were best for machining aluminum.

ix. The kinetic energy of the particles, and thus the target erosion rate, was maximized at an entrained slurry flow rate of 77% of the water flow rate, roughly consistent with an optimum momentum transfer from the high-pressure water entering the mixing chamber through the orifice to the essentially stationary slurry entering the chamber.

x. The channels made using ASJM became highly asymmetric when multiple passes at relatively high traverse velocities ($V_t \sim 1000$ mm/min) were used to machine relatively

deep (aspect ratio of 0.9 and larger) micro-channels in aluminum. However, the asymmetry did not occur when much lower traverse velocities ($V_t \leq 40$ mm/min) were used. These phenomena were explained in terms of jet deflection from steps on the cutting front that formed at higher traverse velocities.

xi. For both HASJM and AWJM, the W_a and R_a significantly decreased with a decrease in pressure, traverse velocity, and particle dose. The waviness and roughness in both processes at a nozzle angle of $\theta=90°$ were lower than that at $\theta=45°$.

xii. It was found that the W_a of micro-channels with the same depth using HASJM were 6.6 times in Al6061-T6 and 4.3 times in SS316L lower than that in AWJM, while the R_a in both processes were similar.

xiii. Using a crossover condition (i.e. identical free jet particle velocity and equal abrasive dose at a high traverse velocity), the erosion rate in AWJM was also found to be higher by 26% in Al6061-T6 and 29% in SS316L than in HASJM due to the higher width and depth of micro-channels resulting from HASJM that in AWJM, because elimination of air bubbles resulted in a smaller jet size in HASJM.

xiv. Entrained air in AWJM resulted in an increase of waviness due to variation in the abrasive flow rate in the air/particle feeding system and formation of a non-homogenous three-phase jet. However, the roughness depended more on particle velocity and particle local impact angle. The entrained air surrounded the peripheral area of the core jet, increased the AWJ size, and led to a growth of channel width in AWJM.

6.3 Contributions

The novel contributions of this dissertation can be summarized as:

i. For the first time, a novel prototype miniature nozzle with a 254 µm mixing tube was used in AWJM and HASJM systems for the milling of micro-channels.

ii. A submerged AWJM was shown for the first time to produce narrower micro-channels than in-air machining, thereby increasing the resolution of the process without reducing the centerline etch rate, and the additional benefits of reducing noise and releasing less abrasive debris to the air.

iii. A new surface evolution model was developed for prediction of shapes of micro-channels in unsubmerged and submerged AWJM. The novel approach considered the decrease in

erosion rate with increasing channel depth, two different erosive efficacy expressions, and the effect of particle local impact angle.

iv. A novel high-pressure (water pump pressure up to 250 MPa) abrasive slurry micro-machining (HASJM) system was introduced, which did not have problems (i.e. a quick wear of slurry valve and nozzle orifice) of conventional slurry micro-machining and provided much smoother channels than AWJM.

v. A double-disc apparatus (DDA) was used for measuring the particle velocity in the free jet in AWJM and HASJM.

vi. An existing model developed for AWJM abrasive particle velocities was modified and used to predict the particle velocity in HASJM, and then verified using a double disc apparatus (DDA).

vii. The effect of the entrained air in abrasive water jet micro-machining (AWJM) was isolated by comparing AWJM milled surfaces with those produced by high-pressure slurry jet micro-machining (HASJM) while maintaining a constant particle velocity.

viii. The effects of air on the quality (i.e. centerline waviness and centerline roughness) and dimensions of micro-channels were investigated using the same particle velocity, abrasive size and type.

ix. The effects of process parameters (e.g. pressure, traverse velocity, dose of particles, nozzle angle) on the W_a and R_a of micro-channels in AWJM and HASJM were investigated.

x. The quality (i.e. centerline waviness and centerline roughness) and dimensions of micro-channels in AWJM and HASJM were compared using the same particle velocity, abrasive size and type.

6.4 Recommendations for future work

A number of interesting extensions to the present work could be made in the future. These are listed below:

i. The surface evolution model in the presented work was tested in submerged and unsubmerged AWJM on metals. However, its reliability for HASJM needs to be investigated.

ii. Further refinements of the surface evolution model will likely require CFD modelling of the complex flows within deeper channels in order to account for the relatively small amount of secondary milling of the sidewalls tending to widen the channels. This would improve the prediction of the channel width in AWJM.

iii. In the present research, a water-based slurry was used in HASJM. Kowsari et al. [129] found that using a dilute polymer-based slurry in a low pressure ASJM system decreased roughness and width of micro-channels in glass. It would be of interest to explore the effect of other solutions (e.g. a dilute high-weight polymer solution) on shape, roughness, and waviness of channels made in ductile and brittle materials by the HASJM system.

iv. The eccentric channel formation in HASJM at a high traverse velocity is an interesting phenomenon that requires further research to fully explain. A CFD model that considers the flow fields within the developing channel may shed light on the secondary milling effect due to slurry flow along the channel that may cause the asymmetry.

v. The presented HASJM can fill the existing gap in utilizing waterjet technologies for milling of micro-channels in metals. The HASJM system provides interesting future opportunity for further downsizing the nozzle whilst avoiding problems with micro-abrasive particle flowability in feeding system.

vi. This thesis experimentally investigated the effect of process parameters in AWJM and HASJM on centerline roughness and centerline waviness of channels. Developing models that allow the prediction of W_a and R_a at the channel centerline as a function of particle velocity and entrained air flow rate would be extremely useful. These models do not currently exist for ductile materials.

vii. In this research, average particle velocity in AWJM and HASJM were predicted using a prediction model and then the results were verified by a double disc apparatus (DDA). However, the DDA work could be expanded to try to determine more than just the average velocity by for example a microscopic investigation of particle impact angle and size on the recording disc. The model can be improved to predict the particle velocity distribution and particle velocity at higher standoff distances.

References

[1]   A. L. Miller and J. H. Archibald, "Measurement of particle velocities in an abrasive jet cutting system," *in Proceedings of the 6th American Water Jet Conference*, Houston, Texas, pp. 291-304, 1991.

[2]   J. Y. Sheikh-Ahmad, "Machining of polymer composites," *Springer*, New York, pp. 164-165, 2009.

[3]   I. Kharagpur, "Non conventional machining, lesson 37, water jet and abrasive water jet machining," *Available at works. bepress. Com*, 2012.

[4]   D. S. Miller, "Micromachining with abrasive waterjets," *Journal of Materials Processing Technology*, vol. 149, pp. 37–42, 2004.

[5]   M. Hashish, "Milling with abrasive-waterjets: A preliminary investigation," *in Proceeding of the 4th U.S. Water Jet Conference*, California, Berkeley, U.S.A, pp. 1-20, 1987.

[6]   M. Hashish, "Investigation of milling with abrasive-waterjets," *Journal of engineering for industry*, vol. 111, no. 2, pp. 158-166, 1989.

[7]   G. Fowler, P. H. Shipway, and I. R. Pashby, "Abrasive water-jet controlled depth milling of Ti6Al4V alloy-an investigation of the role of jet-workpiece traverse speed and abrasive grit size on the characteristics of the milled material," *Journal of Materials Processing Technology*, vol. 161, pp. 407-414, 2005.

[8]   Y. M. Ali and J. Wang, "Impact abrasive machining," *Machining with Abrasive, Springer*, London, pp. 385-420, 2011.

[9]   A. Alberdi, A. Rivero, L. N. López de Lacalle, I. Etxeberria, and A. Suárez, "Effect of process parameter on the kerf geometry in abrasive water jet milling," *International Journal of Advanced Manufacturing Technology*, vol. 51, pp. 467–480, 2010.

[10]   B. Freist, H. Haferkamp, A. Laurinat, and H. Louis, "Abrasive jet machining of ceramic products," *in Proceedings of the 5th American Water Jet Conference*, Toronto, Canada, 1989.

[11]   A. Laurinat, H. Louis, and G. A. Meier-Wiechert, "Model for milling with abrasive water jets," *in Proceedings of 7th American Water Jet Conference*, Seattle, USA, 1993.

[12]   O. Flynn, D. J. Bingley, M. S. Bradley, and M. S. A. Burnett, "A model to predict the solid particle erosion rate of metals and its assessment using heat-treated steels," *Wear*, vol. 248, pp. 162-177, 2000.

[13]   S. G. Sapate and R. Rama, "Effect of material hardness on erosive wear behavior of some weld-deposited alloys," *Materials and Manufacturing Processes*, vol. 17, no. 2, pp. 187-198, 2002.

[14]   P.H. Shipway, "The effect of plume divergence on the spatial distribution and magnitude of wear in gas-blast erosion," *Wear*, vol. 205, pp. 169-177, 1996.

[15]   M. Hashish, "The effect of beam angle in abrasive waterjet machining," *Journal of Manufacturing Science and Engineering*, vol. 115, no. 1, pp. 51–56, 1993.

[16]   G. Fowler, P. Shipway, and I. Pashby, "A technical note on grit embedment following abrasive water-jet milling of a titanium alloy," *Journal of Materials Process Technology*, vol. 159, pp. 356–368, 2005.

[17]   S. Anwar, D. A. Axinte, and A. A Becker, "Finite element modeling of a single-particle impact during abrasive waterjet milling," *in Proceeding of Institution of Mechanical Engineers, Part J: Journal of Engineering Tribology*, vol. 225, no. 8, pp. 821-832, 2011.

[18]   Y. M. Ali, P. Mathew, and J. Wang, "Progress in the Modeling of Abrasive Jet Machining," *Advanced Materials Research*, vol. 126, pp. 3-8, 2010.

[19]   H. Getu, A. Ghobeity, J. K. Spelt, and M. Papini, "Abrasive jet micromachining of acrylic and polycarbonate polymers at oblique angles of attack," *Wear*, vol. 265, pp. 888-901, 2008.

[20]   S. Ally, "Abrasive jet micro-machining of metals," MASc thesis, Department of mechanical and industrial engineering, Ryerson University, Toronto Ontario, 2011.

[21]   S. Ally, J. K. Spelt, and M. Papini, "Prediction of Machined Surface Evolution in the Abrasive Jet Micro-machining of Metals," *Wear*, vol. 292, pp. 89–99, 2012.

[22]   L. K. Ives and A. W. Ruff, "Electron microscopy study of erosion damage in copper," *Erosion: Prevention and Useful Applications*, vol. 664, pp. 5–35, 1977.

[23]   J. H. Neilson and A. Gilchrist, "Erosion by stream of solid particles," *Wear*, vol. 11, pp. 111–122, 1968.

[24]   G. B. Stachowiak and G. W. Stachowiak, "The effects of particle characteristics on three body abrasive wear," *Wear*, vol. 249, pp. 201–207, 2001.

[25]   S. Armada, T. Hirose, and T. Senda, "Quantitative evaluation of residual grits under angled blasting, Surf. Coat," *Surface and Coatings Technology*, vol. 111, no. 1, pp. 1–9, 1999.

[26]   J.B. Zu, G. T. Burstein, and I. M. Hutchings, "A comparative study of the slurry erosion and free fall particle erosion of aluminium," *Wear*, vol. 149, pp. 73–84, 1991.

[27]   M. Ramulu and S. P. Raju, "Hydro-abrasive erosion characteristics of 30vol.SiCp/6061T6 Al composite at shallow impact angles," *Wear*, vol. 166, pp. 55–63, 1993.

[28]   P. H. Shipway, G. Fowler, and I. R. Pashby, "Characteristics of the surface of a titanium alloy following milling with abrasive waterjets," *Wear*, vol. 258, pp. 123-132, 2005.

[29]   A.W. Momber and R. Kovacevic, "Principle of abrasive water jet machining," *Springer Science*, 1998.

[30]   D. A. Summers, J. Yao, and W. Z. Wu, "A further investigation of diajet cutting," *in Proceeding of the 10th International Symposium on Jet Cutting*, Technology, Amsterdam, Holland. 1990.

[31] M. Ramulu, "Dynamic photoelectric investigation on the mechanics of waterjet and abrasive waterjet machining," *Optics and Laser*, vol. 19, pp. 43-65, 1993.

[32] L. Huang, J. Folkes, P. Kinnell, and P. H. Shipway, "Mechanisms of damage initiation in a titanium alloy subjected to water droplet impact during ultra-high pressure plain waterjet erosion," *Journal of Materials Processing Technology*, vol. 212, no.9, pp. 1906-1915, 2012.

[33] M. C. Kong, D. Axinte, and W. Voice, "Aspects of material removal mechanism in plain waterjet milling on gamma titanium aluminide," *Journal of Materials Processing Technology*, vol. 210, pp. 573–584, 2010.

[34] U. Himmelreich, "Fluiddynamische Modelluntersuchungen an Wasserabrasivstrahlen," *VDI-Verlag*, Dusseldorf, 1993.

[35] A. Tazibt, N. Abriak, and F. Parsy, "Prediction of abrasive particle velocity in a high pressure water jet and effect of air on acceleration process," *European Journal of Mechanics, B/Fluids*, vol. 15, no. 4, pp. 527-543, 1996.

[36] A. Tazibt, F. Parsy, and N. Abriak, "Theoretical analysis of the particle acceleration process in abrasive water jet cutting," *Computational Materials Science*, vol. 5, no. 1, pp. 243-254, 1996.

[37] A. Laurinat, H. Louis, and G. A. Meier-Wiechert, "Model for milling with abrasive water jets," *in Proceeding of the 7th Am. Water Jet Conf.*, Seattle, USA, 1993.

[38] J. Madadnia, D. K. Shanmugam, T. Nguyen, and J. Wang, "A study of cavitation induced surface erosion in abrasive waterjet cutting systems," *Advanced Materials Research*, vol. 53, pp. 357-362, 2008.

[39] A. Chillman, M. Ramulu, and M. Hashish, "Waterjet and water-air jet surface processing of titanium alloy: a parametric evaluation," *Journal of Manufacturing Science and Engineering*, vol. 132, no. 1, pp. 011012, 2010.

[40] Y. I. Oka, S. Mihara, and H. Miyata, "Effective parameters for erosion caused by water droplet impingement and applications to surface treatment technology," *Wear*, vol. 263, pp. 386-394, 2007.

[41] K. M. C. Ojmertz and N. Amini, "A discrete approach to the abrasive water jet milling process," *in Proceedings of the 12th International Conference on Jet Cutting Technology*, Rouen, France, pp. 425–434, 1994.

[42] C. Leu, P. Meng, E. S. Geskin, and L. Tismeskiy, "Mathematical modeling and experimental verification of stationary waterjet cleaning process," *Journal of Manufacturing Science and Engineering*, vol. 120, pp. 571-579, 1998.

[43] K. Yanaida and A. Ohashi, "Flow characteristics of water jets in air," *in Proceedings of the 4th International conference on Jet Cutting Technology*, Canterbury, UK, pp. 39–53, 1978.

[44]   K. Yanaida and A. Ohashi, "Flow characteristics of water jets in air," *in Proceedings of the 5th International Symposium on Jet Cutting Technology*, Bedfield, UK, pp. 33–44, 1980.

[45]   F. L. Chen and E. Siores, "The effect of cutting jet variation on striation formation in abrasive water jet cutting," *International Journal of Machine Tools and Manufacture*, vol. 41, no. 10, pp. 113-121, 2001.

[46]   M. Monno and C. Ravasio, "The effect of cutting head vibrations on the surfaces generated by waterjet cutting," *International Journal of Machine Tools and Manufacture*, vol. 45, pp. 355-363, 2005.

[47]   M. Ramulu and D. Arola, "Influence of abrasive waterjet cutting conditions on the surface quality of graphite/epoxy laminates," *International Journal of Machine Tools and Manufacture*, vol. 34, no. 3, pp. 295-313, 1994.

[48]   J. Wang, T. Nguyen, and K. L. Pang, "Mechanism of microholes formation on glasses by an abrasive slurry jet," *Journal of Applied Physics*, vol. 105, no. 4, pp. 044906, 2009.

[49]   M. C. Kong, S. Anwar, J. Billingham, and D. A. Axinte, "Mathematical modeling of abrasive waterjet footprints for arbitrarily moving jets: Part I-single straight paths," *International Journal of Machine Tools and Manufacture*, vol. 53, no. 1, pp. 58-68, 2012.

[50]   R. Kovacevic and M. Fang, "Modeling of the influence of the abrasive waterjet cutting parameters on the depth of cut based on fuzzy rules," *International Journal of Machine Tools and Manufacture*, vol. 34, no. 1, pp. 55–72, 1994.

[51]   M.E. Tobgy, E. G. Ng, and M. A. Elbestawi, "Modeling of abrasive waterjet machining: a new approach," *CIRP Annals—Manufacturing Technology*, vol. 54, no.1, pp. 285–288, 2005.

[52]   A. Carrascal and A. Alberdi, "Evolutionary industrial physical model generation," in: M. Grana Romay, E. Corchado, M. Teresa Garcia Sebastian (Eds.), *Hybrid Artificial Intelligence Systems*, *Springer*, Berlin Heidelberg, pp. 327–334, 2010.

[53]   D. A Axinte, D. S. Srinivasu, J. Billingham, and M. Cooper, "Geometrical modeling of abrasive waterjet footprints: A study for 90° jet impact angle," *CIRP Annals—Manufacturing Technology*, vol. 59, no. 1, pp. 341-346, 2010.

[54]   J. Billingham, C. B. Miron, D. A. Axinte, and M. C. Kong, "Mathematical modelling of abrasive water jet foot prints for arbitrarily moving jets: PartII-Overlapped single and multiple straight paths," *International Journal of Machine Tools and Manufacture*, vol. 68, pp. 30-39, 2013.

[55]   J. H. M. ten Thije Boonkkamp and J. K. M. Jansen, "An analytical solution for mechanical etching of glass by powder blasting," *Journal of Engineering Mathematics*, vol. 43, pp. 385-399, 2002.

[56]   P. J. Slikkerveer and F. H. in't Veld, "Model for patterned erosion," *Wear*, vol. 233, pp. 377–386, 1999.

[57]   H. Getu, A. Ghobeity, J. K. Spelt, and M. Papini, "Abrasive jet micromachining of polymethylmethacrylate," *Wear*, vol. 263, pp. 1008-1015, 2007.

[58]   A. Ghobeity, T. Krajac, T. Burzynski, M. Papini, and J. K. Spelt, "Surface evolution models in abrasive jet micromachining," *Wear*, vol. 264, pp. 185-198, 2008.

[59]   Y. I. Oka, H. Ohnogi, T. Hosokawa, and M. Matsumura, "The impact angle dependence of erosion damage caused by solid particle impact," *Wear*, vol. 203, pp. 573-579, 1997.

[60]   Y. I. Oka, S. Mihara, and T. Yoshida, "Impact-angle dependence and estimation of erosion damage to ceramic material caused by solid particle impact," *Wear*, vol. 267, pp. 129-135, 2009.

[61]   C. T. Morrison, R. O. Scattergood, and J. L. Routbort, "Erosion of 304 stainless steel," *Wear*, vol. 111, pp. 1-13, 1986.

[62]   S. Yerramareddy and S. Bahadur, "Effect of operational variables, microstructure and mechanical properties on the erosion of Ti-6Al-4V," *Wear*, vol. 142, pp. 253-263, 1991.

[63]   M. Annoni, L. Cristaldi, M. Norgia, and C. Svelto, "Measurement of water jet velocity distribution using laser velocimetry," *IEEE Transactions on Instrumentation and Measurement*, vol. 57, no. 8, pp. 1524-1528, 2008.

[64]   Y. Dong, L. J. Tyler, D. A. Summers, and M. Johnson, "Experimental study of particle velocity measurement in abrasive water jet cutting in the nozzle and jet stream using multiple sensing elements," *in Proceedings of the 17th International Conference on Water Jetting: Advances and Future Needs*, pp. 137-147, 2004.

[65]   A. H. Osman, T. Mabrouki, B. Théry, and D. Buisine, "Experimental analysis of high-speed air-water jet flow in an abrasive water jet mixing tube," *Flow Measurement and Instrumentation*, vol. 15, no. 1, pp. 37-48, 2004.

[66]   A. W. Momber, "Energy transfer during the mixing of air and solid particles into a high-speed waterjet: An impact-force study," *Experimental Thermal and Fluid Science*, vol. 25, no. 1, pp. 31-41, 2001.

[67]   R. K. Swanson, M. Kilman, S. Cerwin, W. Tarver, and R. Wellman, "Study of particle velocities in water driven abrasive jet cutting," *in Proceedings of the 4th U.S. water jet conference*, pp. 163-167, 1987.

[68]   T. Sawamura, Y. Fukunishi, and R. Kobayashi, "Velocity measurement of abrasive waterjet by a combination of PIV and PTV," *Nihon Kikai Gakkai Ronbunshu, B Hen/Transactions of the Japan Society of Mechanical Engineers Part B*, vol. 66, no. 641, pp. 50-56, 2000.

[69]   P. S. Coray, B. Jurisevic, M. Junkar, and K. C. Heiniger, "Measurements on 5:1 scale abrasive water jet cutting head models," *in Proceedings of the 6th International Conference on Management of Innovative Technologies,* MIT'2003--post-conference edition. Ljubljana: University of Ljubljana, pp. 87-102, 2003.

[70]   R. Wäger, W. A. Messelink, H. Looser, K. C. Heiniger, and O. W. Fähnle, "Particle tracking in a Fluid jet polishing slurry flow," *in Proceedings of SPIE Optifab*, 2005.

[71]   P. Roth, H. Looser, K. C. Heiniger, and S. Buhler, "Determination of abrasive particle velocity using laser-induced fluorescence and particle tracking methods in abrasive waterjets," *in Proceeding of the WJTA American Waterjet Conference*, 2005.

[72]   H.-T. Liu, P. J. Miles, N. Cooksey, and C. Hibbard, "Measurement of water-droplet and abrasive speeds in a ultra-high-pressure abrasive waterjets," *in Proceedings of the 10th American Waterjet Conference*, Houston, Texas, 1999.

[73]   S. Zhang, X. Li, and Y. Gu, "Air flow exploration of abrasive feed tube," *Acta Mechanica Sinica/Lixue Xuebao*, vol. 25, no. 6, pp. 761-768, 2009.

[74]   M. Hashish, "Controlled depth milling of isogrid structures with AWJ," *Journal of Manufacturing and Science Engineering*, vol. 120, pp. 21-27, 1998.

[75]   M. Hashish, "Characteristics of surfaces machined with abrasive-waterjets," *Journal of Engineering Materials and Technology*, vol. 113, no. 3, pp. 354-362, 1991.

[76]   S. Paul, A. M. Hoogstrate, C. A. van Luttervelt, and H. J. J. Klas, "An experimental investigation of rectangular pocket milling with abrasive water jet," *Journal of Materials Processing Technology*, vol. 73, pp. 179-188, 1998.

[77]   D. S. Srinivasu, D. A. Axinte, P. H. Shipway, and J. Folkes, "Influence of Kinematic operation parameters on kerf geometry in abrasive waterjet machining of silicon carbide ceramics," *International Journal of Machine Tools and Manufacture*, vol. 49, pp. 1077-1088, 2009.

[78]   A. Ghobeity, H. Getu, M. Papini, and J. K. Spelt, "Surface evolution models for abrasive jet micromachining of holes in glass and polymethylmethacrylate (PMMA)," *Journal of Micromechanics and Micro engineering*, vol. 17, pp. 2175-2185, 2007.

[79]   Z. W. Liu, C. Z. Huang, H. T. Zhu, H. L. Liu, and B. Zou, "Study on jet formation and modeling for high pressure abrasive water-jet," *Key Engineering Materials*, vol. 487, pp. 468-472, 2011.

[80]   H. Z. Li, J. Wang, and J. M. Fan, "Analysis and modeling of particle velocities in micro-abrasive air jet," *International Journal of Machine Tools and Manufacture*, vol. 49, no. 11, pp. 850-858, 2009.

[81]   C. Narayanan, R. Balz, D. A. Weiss, and K. C. Heiniger, "Modeling of abrasive particle energy in water jet machining," *Journal of Materials Processing Technology*, vol. 213, pp. 2201-2210.

[82]   H. T. Liu, E. Schubert, D. McNiel, and K. Soo, "Application of abrasive-fluid jets for precision machining of composites," *SAMPLE Conference*, Seattle, Washington, 2010.

[83]   H. T. Liu, "Water jet technology for machining fine features pertaining to micromachining," *Journal of Manufacturing Processes*, vol. 12, pp. 8-18, 2010.

[84] H. T. Liu and E. Schubert, "Chapter 10, Micro abrasive-waterjet technology," Mojtaba Kahrizi (Ed.), Micromachining Techniques for Fabrication of Micro and Nano Structures, *InTech Open Access Publisher*, Manhattan, New York, USA, 2012.

[85] H. T. Liu, Y. Hovanski, D. D. Caldwell, and R. E. Williford, "Low-cost manufacturing of flow channels with multi-nozzle abrasive-waterjets: A feasibility investigation," *in Proceeding of the 19th International Conference on Water Jetting*, Nottingham, UK, pp. 15-17, 2008.

[86] C. Iliescu, B. Chen, F. E. H. Tay, G. Xu, and J. M. Miao, "Characterization of deep wet etching of glass," *Microelectronics, MEMS, and Nanotechnology*, International Society for Optics and Photonics, pp. 60370A-2, 2005.

[87] X. Cheng, A. Wang, K. Nakamoto, and K. Yamazaki, "A study on the micro tooling for micro/nano milling," *International Journal of Advanced Manufacturing Technology*, vol. 53, pp. 523-533, 2011.

[88] O. Iordan and C. Burlacu, "The main factors of influence in the micromilling field," *Academic Journal of Manufacturing Engineering*, vol. 48, pp. 43-49, 2010.

[89] C. T. Yang, S. S. Ho, and B. H. Yan, "Micro hole machining of borosilicate glass through electrochemical discharge machining (ECDM)," *Key Engineering Materials*, vol. 196, pp. 149-166, 2001.

[90] H. Ogura and Y. Yoshida, "Hole drilling of glass substrates with a CO2 laser," *Japanese Journal of Applied Physics*, vol. 42, pp. 2881–2886, 2003.

[91] K. Pang, T. Nguyen, J. Fan, and J. Wang, "Machining of micro-channels on brittle glass using an abrasive slurry jet," *Key Engineering Materials*, vol. 443, pp. 639-644, 2010.

[92] F. Haerle, M. Champy, and B. Terry (Ed.), "Atlas of craniomaxillofacial osterosynthesis: Microplates, miniplates, and screws," 2nd Ed., *Thieme*, New York, pp. 225, 2009.

[93] N. D. M. Begg, "Blind transmembrane puncture access: design and development of a novel laparoscopic trocar and blade retraction mechanism," PhD dissertation, Massachusetts Institute of Technology, 2011.

[94] R. Kovacevic, "Monitoring the depth of abrasive waterjet penetration," *International Journal of Machine Tools and Manufacture*, vol. 32, no. 5, pp. 725-727, 1992.

[95] L. Chen, E. Siores, and W. C. K. Wong, "Control of the abrasive waterjet cutting process," *Transactions of the Institution of Engineers,* Australia. Mechanical engineering, vol. 21, no. 1, pp. 66-66, 1996.

[96] H. M. Clark and L. C. Burmeister, "The influence of squeeze film on particle impact velocities in erosion," *International Journal of Impact Engineering*, vol. 12, no. 3, pp. 415-426, 1992.

[97] T. Matsumura, T. Muramatsu, and S. Fueki, "Abrasive water jet machining of glass with stagnation effect," *CIRP Annals—Manufacturing Technology*, vol. 60, pp. 355-358, 2011.

[98]   Z. Lv, Z., C. Huang, C., J. Wang, H. Zhu, and C. Che, "A 3D simulation on fluid field at the impact zone of abrasive water jet under different impact angles," *Advanced Materials Research*, vol. 565, pp. 345-350, 2012.

[99]   A. Radavanska, T. Ergic, Z. Ivandic, S. Hloch, J. Valicek, and J. Mullerova, "Technical possibilities of noise reduction in material cutting by abrasive water jet," *Strojarstvo*, vol. 5, no. 4, pp. 347-354, 2009.

[100]   S. Shimizu, "Erosion due to premixed abrasive water jet under submerged condition," *Nippon Kikai Gakkai Ronbunshu, B Hen/Transactions of the Japan Society of Mechanical Engineers, Part B*, vol. 59, no. 566, pp. 2964-2968, 1993.

[101]   C. Wulf, "Geometrie und zeitliche entwicklung des schnittsplates bein wasser strahschneiden," PhD dissertation, RWTH Aachen University, Aachen, Germany, 1986.

[102]   M. Hashish, "Characteristics of surfaces machined with abrasive-waterjets," *Transactions of ASME, Journal of Engineering Materials and Technology*, vol. 113, pp. 354-362, 1991.

[103]   N. S. Guo, "Abrasive water jet cutting-methods to calculate cutting performance and cutting efficiency," *in Proceedings of the International Conference Geomechanics*, vol. 93, pp. 291-299, 1994.

[104]   K. F. Neusen, T. J. Gores, and R. S. Amano, "Axial variation of particle and drop velocities downstream from an abrasive water jet mixing tube in jet cutting technology," *in Proceedings of the 12th Conference on Jet Cutting Technology*, pp 93-103, 1994.

[105]   A. A. S. Bhagat, S. S. Kuntaegowdanahalli, and I. Papautsky, "Enhanced particle filtration in straight micro-channels using shear-modulated inertial migration," *Physics of Fluids*, vol. 20, no. 10, pp. 101702-4, 2008.

[106]   S. D. Thakre, V. B. Swami, and P. D. Malwe, "Cooling systems of electronics devices using micro-channel heat sink," *International Journal of Thermal Technologies*, vol. 4, no. 2, pp. 58-60, 2014.

[107]   W. Chang, D. Trebotich, L. P. Lee, and D. Liepmann, "Blood flow in simple micro-channels," *in Proceedings of the 1st International IEEE-EMBS Special Topic Conference on Micro-technologies in Medicine and Biology*, Lyon, France, pp. 1-5, 2000.

[108]   K. Ohno, K. Tachikawa, and A. Manz, "Microfluidics: applications for analytical purposes in chemistry and biochemistry," *Electrophoresis*, vol. 29, no. 22, pp. 4443-53, 2008.

[109]   T. Kawai, K. Sueyoshi, F. Kitagawa, and K. Otsuka, "Microchips electrophoresis of oligosaccharides in single' straight channels," *in Proceedings of the 14th International Conference on Miniaturized Systems for Chemistry and Life Sciences*, Groningen, Netherlands, pp. 354-356, 2010.

[110]   M. Agus, A. Bortolussi, N. Careddu, R. Ciccu, B. Grosso, and G. Marras, "Multi-pass abrasive waterjet cutting strategy," *in Proceedings of the 16th International Conference on Water Jetting*, Aix en Provence, France, pp. 16-18, 2002.

[111] J. Wang and D. M. Guo, "The cutting performance in multipass abrasive waterjet machining of industrial ceramics," *Journal of Materials Processing Technology*, vol. 133, pp. 371-377, 2002.

[112] S. C. Crow, "A theory of Hydraulic Rock Cutting," *International Journal of Rock Mechanics and Mining Sciences*, vol. 10, pp. 567-584, 1973.

[113] G. A. Rehbinder, "Theory about cutting rock with water jet," *Rock Mechanics*, vol. 12, pp. 247-257, 1980.

[114] L. Hlaváč and J. Vašek, "Physical model of high energy liquid jet for cutting rock," *International Journal of Water Jet Technology*, vol. 2, no. 1, pp. 39-50, 1994.

[115] M. Hashish, "On the Modeling of Abrasive Waterjet Cutting," *in Proceedings of the 7th International Jet Cutting Symposium*, pp. 249-265, 1984.

[116] J. Wang, "Predictive depth of jet penetration models for abrasive waterjet cutting of alumina ceramics," *International Journal of Mechanical Science*, vol. 49, pp. 306-316, 2006.

[117] K. M. C. Ojmertz and N. Amini, "A discrete approach to the abrasive water jet milling process," *in Proceedings of the twelfth International Conference on Jet Cutting Technology*, pp. 425–434, 1994.

[118] A. Carrascal and A. Alberdi, "Evolutionary industrial physical model generation," *Hybrid Artificial Intelligence Systems*, *Springer*, Berlin Heidelberg, pp. 327–334, 2010.

[119] S. Anwar, D. A. Axinte, and A. A. Becker, "Finite element modeling of abrasive waterjet milled foot prints," *Journal of Materials Processing Technology*, vol. 213, no. 2, pp. 180-193, 2012.

[120] A. Lebar and M. Junkar, "Simulation of abrasive water jet cutting process: Part 1. Unit event approach," *Modelling and Simulation in Materials Science and Engineering*, vol. 12, no. 1, pp. 1159–1170, 2004.

[121] H. Getu, A. Ghobeity, J. K. Spelt, and M. Papini, "Abrasive jet micromachining of acrylic and polycarbonate polymers at oblique angles of attack," *Wear*, vol. 265, no. 5, pp. 888-901, 2008.

[122] H. Nouraei, K. Kowsari, J. K. Spelt, and M. Papini, "Surface evolution models for abrasive slurry jet micro-machining of channels and holes in glass," *Wear*, vol. 309, no. 1, pp. 65–73, 2014.

[123] N. Haghbin, J. K. Spelt, and M. Papini, "Abrasive waterjet micro-machining of channels in metals: comparison between machining in air and submerged in water," *International Journal of Machine Tools and Manufacture*, vol. 88, pp. 108-117, 2015.

[124] H. T. Liu and W. Sagawa, "Roles of abrasive in AWJ meso-micro machining," *in Proceedings of 22nd International of Conference of Water Jet*, Haarlem, Netherlands, pp. 151-165, 2014.

[125] N. Nguyen and S. Wereley, "Fundamentals and applications of microfluidics," Artech House, Norwood, MA, USA, 2002.

[126] G. K. Guruparan, M. Sathish, N. S. Subramaniam, and T. S. kumar, "Design and fabrication of micro-channels for MEMS applications," *Journal of Synthesis and Reactivity in Inorganic, Metal-Organic and Nano-Metal Chemistry*, vol. 6, no. 2, pp. 185-191, 2006.

[127] T. Nguyen, K. Pang, and J. Wang, "A preliminary study of the erosion process in micro-machining of glasses with a low pressure slurry jet," *Key Engineering Materials*, vol. 389, pp. 375–380, 2009.

[128] H. Nouraei, A. Wodoslawsky, M. Papini, and J. K. Spelt, "Characteristics of abrasive slurry jet micro-machining: A comparison with abrasive air jet micro-machining," *Journal of Materials Processing Technology*, vol. 213, no. 10, pp. 1711-1724, 2013.

[129] K. Kowsari, H. Nourei, D. F. James, J. K. Spelt, and M. Papini, "Abrasive slurry jet micro-machining of holes in brittle and ductile materials," *Journal of Materials Processing Technology*, vol. 214, pp. 1909-1920, 2014.

[130] M. Hashish, "Performance of high-pressure abrasive suspension jet system," *ASME-PUBLICATIONS-PED*, vol. 67, pp. 199-207, 1993.

[131] H. T. Liu, "Near-net shaping of optical surfaces with UHP abrasive suspension Jets," *in Proceedings of the 14th International Conference on Jetting Technology*, pp. 285-294, 1998.

[132] N. Haghbin, F. Ahmadzadeh, J. K. Spelt, and M. Papini, "Micro-machining of channels using a high pressure abrasive slurry jet machine (HASJM)," *in Proceedings of the 4M/ICOMM2015 Conference on Micro manufacturing,* Milan, Italy, pp. 459-462, 2015.

[133] L. M. Pua and S. O. Rumbold, "Industrial micro-channel devices where are we today," *in Proceedings of the 1st International ASME Conference on Micro-channels and Mini-channels*, pp. 773-780, 2003.

[134] S. Zhang, X. Li, and Y. Gu, "Optimum abrasive flow rate modelling for titanium alloy cutting using abrasive water jet," *International Journal of Abrasive Technology*, vol. 2, no. 4, pp. 400-419, 2009.

[135] K. Dadkhahipour, T. Nguyen, and J. Wang, "Mechanisms of channel formation on glasses by abrasive waterjet milling," *Wear*, vol. 292, pp. 1–10, 2012.

[136] U. Aich, S. Banerjee, and A. Bandyopadhyay, "Multi-objective optimization of abrasive water jet machining responses by simulated annealing and particle swarm," *International Journal of Mechatronics and Manufacturing Systems*, vol. 7, no. 1, pp. 38-59, 2014.

[137] J. M. Fan, C. Y. Wang, and J. Wang, "Modelling the erosion rate in micro abrasive air jet machining of glass," *Wear*, vol. 266, pp. 968-974, 2009.

[138]   D. Ciampini, J. K. Spelt, and M., Papini, "Simulation of interference effects in particle stream following impact with a flat surface Part I. Theory and analysis," *Wear*, vol. 254, pp. 237-249, 2003.

[139]   J. Wang, "Abrasive waterjet machining of polymer matrix composites cutting performance, erosive process and predictive model," *International Journal of Advanced Manufacturing Technology*, vol. 15, pp. 757-768, 1999.

[140]   M. Hashish, "Visualization of the abrasive-waterjet cutting process," *Experimental mechanics*, vol. 28, no. 2, pp. 159-169, 1988.

[141]   H. Orbanic and M. Junkar, "Analysis of striation formation mechanism in abrasive water jet cutting," *Wear*, vol. 265, no. 5, pp. 821-830, 2008.

[142]   N. S. Guo, H. Louis, and G. Meier, "Surface structure and kerf Geometry in abrasive water jet cutting: formation and optimization," *in Proceedings of the 7th American Water Jet Conference*, Washington, pp. 1-25, 2003.

[143]   N. Haghbin, F. Ahmadzadeh, J. K. Spelt, and M. Papini, "High pressure abrasive slurry jet micro-machining using slurry entrainment," *International Journal of Advanced Manufacturing Technology*, pp. 1-13, 2015.

[144]   G. L. Chahine, A. Kapahi, J. K. Choi, and C. T. Hsiao, "Modeling of surface cleaning by cavitation bubble dynamics and collapse," *Ultrasonics Sonochemistry*, In press, 2015.

[145]   M. Firouzi, A. V. Nguyen, and S. H. Hashemabadi, "The effect of microhydrodynamics on bubble-particle collision interaction," *Mineral Engineering*, vol. 24, pp. 973-986, 2011.

[146]   P. Tang and V. M. Puri, "Methods for minimizing segregation: a review," *Particulate Science and Technology*, vol. 22, no. 4, pp. 321-337, 2004.

[147]   Q. Li, V. Rudolph, B. Weigl, and A. Earl, "Interparticle van der Waals force in powder flowability and compatibility," *International journal of pharmaceutics*, vol. 280, no. 1, pp. 77-93, 2004.

[148]   H. K. Pak and P. R. Behringer, "Bubbling in vertically vibrated granular materials," *Nature*, vol. 371, no. 6494, pp. 231-233, 1994.

[149]   G. I. Tardos and Q. Lu, "Precision dosing of powders by vibratory and screw feeders: an experimental study," *Advanced Powder Technology*, vol. 7, no. 1, pp. 51-58, 1996.

[150]   A. Ghobeity, H. Getu, T. Krajac, J. K. Spelt, and M. Papini, "Process repeatability in abrasive jet micro-machining," *Journal of Materials Processing Technology*, vol. 190, no. 1, pp. 51-60, 2007.

[151]   J. Yang, A. Sliva, A. Banerjee, R. N. Dave, and R. Pfeffer, "Dry particle coating for improving the flowability of cohesive powders," *Powder Technology*, vol. 158, no. 1, pp. 21-33, 2005.

[152]   R. Balz and K. C. Heiniger, "Determination of spatial velocity distributions of abrasive particles in abrasive water jets using laser-induced fluorescence under real conditions," *in Proceedings of 16th WJTA-IMCA Conference and Expo*, Houston, Texas, 2011.

[153]   R. Balz, R. Mokso, C. Narayanan, D. A. Weiss, and K. C. Heiniger, "Ultra-fast X-ray particle velocimetry measurements within an abrasive water jet," *Experiments in fluids*, vol. 54, no. 3, pp. 1-13, 2013.

[154]   A. W. Ruff and L. K. Ives, "Measurement of solid particle velocity in erosive wear," *Wear*, vol. 35, pp. 195-199, 1975.

[155]   N. Haghbin, J. K. Spelt, and M. Papini, "Abrasive waterjet micro-machining of channels in metals: Model to predict high aspect-ratio channel profiles for submerged and unsubmerged machining," *Journal of Materials Processing Technology*, vol. 222, pp. 399-409, 2015.

[156]   ASME B46.1, "Surface texture (surface roughness, waviness, and lay)," *The American Society of Mechanical Engineers*, New York, 1995.

[157]   ISO 4288, "Geometrical product specifications (GPS)-surface texture: profile method-rules and procedures for the assessment of surface texture," *International Organization for Standardization*, 1996.

[158]   A. D. Burns, T. Frank, I. Hamill, and J. M. Shi, "The favre averaged drag model for turbulent dispersion in eulerian multi-phase flow," *in Proceedings of 5th International Conference on Multiphase Flow*, ICMF 04, Yokohama, Japan, 2004.

[159]   C. Crowe, M. Sommerfeld, and Y. Tsuji, "Multiphase flows with droplets and particles," *CRC Press*, Boca Raton, FL., USA.

[160]   C. Che, C. Huang, J. Wang, H. Zhu, and Q. Li, "Theoretical model of surface roughness for polishing super hard materials with abrasive waterjet," *Key Engineering Materials*, vol. 375-378, pp. 465-469, 2008.

[161]   F. Cenac, M. Deleris, F. Collombet, and R. Zitoune, "Abrasive water jet milling of composite materials: Material integrity," *in Proceedings of American WJTA Conference and Expo*, Houston, Texas, 2009.

[162]   K. M. C. Ojmertz, "Abrasive waterjet milling: An experimental investigation," *in Proceedings of the 7th American Water Jet Conference*, Seattle, Washington, vol. 2, pp. 777-791, 1993.

[163]   H. Fang, P. Guo, and J. Yu, "Surface roughness and material removal in fluid jet polishing," *Applied optics*, vol. 45 (17), pp. 4012-4019, 20, 2006.

[164]   R. H. Mohammad Jafar, J. K. Spelt, and M. Papini, "Numerical simulation of surface roughness and erosion rate of abrasive jet micro-machined channels," *Wear*, vol. 303, pp. 302-312, 2013.

[165] Y. P. Liao, C. Y. Wang, Y. N. Hu, and Y. X. Song, "The slurry for glass polishing by micro abrasive suspension jets," *Advanced Materials Research*, vol. 69, pp. 322-327, 2009.